2013

Automatic Block-Matching Registration to Improve Lung Tumor Localization During Image-Guided Radiotherapy

Scott Robertson
Virginia Commonwealth University

AUTOMATIC BLOCK-MATCHING REGISTRATION TO IMPROVE LUNG TUMOR LOCALIZATION DURING IMAGE-GUIDED RADIOTHERAPY

A dissertation submitted to the Virginia Commonwealth University School of Medicine in partial fulfillment of the requirements for the degree of

DOCTOR OF PHILOSOPHY
MEDICAL PHYSICS

by

Scott Patrick Robertson

Director: Dr. Geoffrey D. Hugo
Assistant Professor
Division of Medical Physics
Department of Radiation Oncology

Virginia Commonwealth University
Richmond, Virginia
May 2013

DEDICATION

To my wife and best friend, thank you for all of your love, support, and patience. No matter how busy we seemed to be, your dedication and positive outlook have always inspired me to be my best.

And to my parents, thank you for always believing in me, and for giving me every opportunity to excel.

ACKNOWLEDGMENTS

I first wish to express my deep appreciation and gratitude to my advisor, Dr. Geoffrey Hugo, for his patience, guidance, and mentorship over the years. He has always afforded me the freedom to grow as a researcher and to feel confident in conducting independent research; yet he has always made time to answer my questions and focus my efforts on the task at hand. I have benefited greatly from his encouragement to present at major conferences and publish in major journals. I simply would not be where I am today without his support.

I would also like to thank my committee members for their help with this dissertation. Dr. Gary Christensen and Dr. James Gordon have provided numerous technical insights to both challenge and enhance my fundamental understanding of image registration and its role in radiotherapy. In addition, the clinical advice of Dr. Elisabeth Weiss has been essential in connecting the technical aspects in this work to the daily practice of radiation oncology. Her contributions have truly given me a strong clinical outlook.

Finally, I would like to recognize the contributions of Dr. Salim Balik and Christian Dial. Their constructive feedback was instrumental in completing this dissertation.

TABLE OF CONTENTS

LIST OF TABLES

LIST OF FIGURES

LIST OF ABBREVIATIONS

3D: Three-dimensional
4D: Four-dimensional
BMR: Block-matching registration
CBCT: Cone-beam computed tomography
CR: Correlation ratio
CT: Computed tomography
CTV: Clinical target volume
DIR: Deformable image registration
DMR: Deformable mesh registration
EDM: Euclidean distance similarity metric
GD: Gradient descent
GN: Gauss-Newton
GTV: Gross tumor volume
IGRT: Image-guided radiotherapy
ITK: Insight Registration and Segmentation Toolkit
kV: Kilovoltage
LM: Levenberg-Marquardt
MCR: Multiple candidate registrations
MLN: Mediastinal lymph nodes
MRI: Magnetic resonance imaging
MV: Megavoltage
NSCLC: Non-small-cell lung cancer
PBNRR: Physics-based non-rigid registration
PPV: Positive predictive value
PTV: Planning target volume
ROI: Region of interest
SBF: Stereotactic body frame
SBRT: Stereotactic body radiotherapy
SEDM: Symmetric Euclidean distance similarity metric
TLV: Total local variance

PREFACE

This dissertation is based on the following papers, referred to in the text by their roman numerals:

I. S. P. Robertson, E. Weiss, and G. D. Hugo, “Localization accuracy from automatic and semi-automatic rigid registration of locally-advanced lung cancer targets during image-guided radiation therapy,” Med. Phys. **39**, 330–341 (2011).

II. S. P. Robertson, E. Weiss, and G. D. Hugo, “Deformable mesh registration for the validation of automatic target localization algorithms.” Submitted to Med. Phys. (2012).

III. S. P. Robertson, E. Weiss, and G. D. Hugo, “A block-matching registration algorithm for localization of locally-advanced lung tumors.” Manuscript in preparation (2013).

IV. S. P. Robertson, S. Balik, E. Weiss, and G. D. Hugo, “Comparison of automatic registration algorithms for locally-advanced lung tumor localization during image-guided radiotherapy.” Manuscript in preparation (2013).

ABSTRACT

AUTOMATIC BLOCK-MATCHING REGISTRATION TO IMPROVE LUNG TUMOR LOCALIZATION DURING IMAGE-GUIDED RADIOTHERAPY

Scott Patrick Robertson

A dissertation submitted in partial fulfillment of the requirements
for the degree of Ph.D., Medical Physics
at Virginia Commonwealth University.

Virginia Commonwealth University, 2013

Director: Dr. Geoffrey D. Hugo
Assistant Professor,
Division of Medical Physics
Department of Radiation Oncology

To improve relatively poor outcomes for locally-advanced lung cancer patients, many current efforts are dedicated to minimizing uncertainties in radiotherapy. This enables the isotoxic delivery of escalated tumor doses, leading to better local tumor control. The current dissertation specifically addresses inter-fractional uncertainties resulting from patient setup variability. An automatic block-matching registration (BMR) algorithm is implemented and evaluated for the purpose of directly localizing advanced-stage lung tumors during image-guided radiation therapy. In this algorithm, small image sub-volumes, termed “blocks”, are automatically identified on the tumor surface in an initial planning computed tomography (CT) image. Each block is independently and automatically registered to daily images acquired immediately prior to each treatment fraction. To improve the accuracy and robustness of BMR, this algorithm incorporates multi-resolution pyramid registration, regularization with a median filter, and a new multiple-candidate-registrations technique. The result of block-matching is a sparse displacement vector field that models local tissue deformations near the tumor surface. The distribution of displacement vectors is aggregated to obtain the final tumor registration, corresponding to the treatment couch shift for patient setup correction. Compared to existing rigid and deformable registration algorithms, the final BMR algorithm significantly improves the overlap between target volumes from the planning CT and registered daily images. Furthermore, BMR results in the smallest treatment margins for the given study population. However, despite these improvements, large residual target localization errors were noted, indicating that purely rigid couch shifts cannot correct for all sources of inter-fractional variability. Further reductions in treatment uncertainties may require the combination of high-quality target localization and adaptive radiotherapy.

CHAPTER 1. INTRODUCTION

The availability of reliable imaging techniques and the ability to visualize the internal anatomy of oncology patients has given rise to an almost limitless number of opportunities to reduce treatment-related uncertainties. These advancements are all comprised within the broad scope of image-guided radiotherapy (IGRT), which is defined as the use of advanced patient imaging to better diagnose, stage, and treat cancerous lesions and to assess the outcomes of these treatments. This work focuses on the branch of IGRT dedicated to reducing uncertainties in treatment delivery specifically through more accurate, precise, and robust patient setup prior to the delivery of each treatment fraction.

State of the art three-dimensional and even four-dimensional imaging modalities have become essential to modern radiotherapy treatments, which rely on highly conformal dose distributions with little room for error. These imaging modalities have contributed to significant improvements in tumor localization and the ability to position nearby risk structures safely away from high dose regions. By reducing positional uncertainties, it becomes possible to treat more conformal target volumes, thereby decreasing the dose to healthy tissues. As a result, escalated doses can be delivered without a corresponding increase in the risk of treatment-related toxicities. The importance of dose escalation stems from an established link with improved local tumor control.[1,2] For lung cancer patients in particular, relatively poor outcomes[3] have motivated more aggressive treatments that have only become possible by reducings treatment-related uncertainties.

Patient setup and tumor localization errors directly impact the efficacy of radiation delivery. To ensure that the prescribed dose is accurately delivered, a number of patient setup correction strategies are currently employed. In some cases, manual alignment of on-treatment images to an initial planning computed tomography (CT) image has been shown to provide reliable target localization. Other studies rely on automatic registration algorithms to improve the reproducibility (and oftentimes efficiency) of patient setup corrections. This dissertation addresses the limitations of current target localization strategies specifically for locally-advanced lung cancer patients. For these patients, large changes in primary tumor shape, volume, and position are commonly observed in response to treatment, which can lead to corresponding changes in pulmonary anatomy. These changes present a major complicating factor in reliable target localization for radiotherapy. Although existing localization techniques can help to mitigate setup uncertainties, large registration errors often persist. A more robust target localization strategy is warranted for efficient, accurate, and robust patient setup corrections during routine IGRT.

The purpose of the current dissertation is to improve upon existing methods of target localization by implementing an automatic registration technique known as “block-matching registration.” In the following sections, the importance of on-treatment imaging for accurate target localization is emphasized. A summary is then presented on the accuracy, benefits, and shortcomings of currently available patient setup protocols. In light of this discussion, block-matching registration is introduced as an attractive solution for many of the current limitations in lung tumor localization. Finally, an overview of specific aims in this dissertation is provided.

On-treatment imaging for patient setup corrections

Imaging is an integral and essential component of modern radiotherapy. Before initiating a treatment course, patients receive an initial CT scan to assess the extent of the gross tumor volume (GTV) and create a suitable treatment plan. The initial CT is thus referred to as the "planning" CT. The planning CT provides a snapshot of the patient's internal anatomy and represents the reference geometry for future treatment fractions. In the current work, it is assumed that a static treatment plan will be delivered for all fractions without adaption or modification. Therefore, the tumor position must be well-known at the time of radiation delivery, regardless of potential changes in tumor shape or volume. Uncertainties in tumor position throughout treatment can reduce the dose to target structures and increase the dose to neighboring risk structures. These uncertainties must be carefully controlled in order to promote safe dose escalation.

Inter-fractional uncertainties can be effectively reduced by acquiring images of the patient at the time of radiation delivery. These images, referred to as "on-treatment" images, provide new snapshots of the target volume and internal anatomy of patients in the treatment position. By comparing on-treatment images against the initial planning CT, tumor localization uncertainties can be identified and corrected by simple couch shifts or, in the case of larger discrepancies, repositioning of the patient on the treatment couch.[4] Numerous studies have shown the benefit of on-treatment imaging in reducing tumor localization uncertainties, relative to setup protocols without imaging (e.g., relying on external surrogates of tumor position such as skin tattoos or immobilization devices).[5–10] As a result, IGRT continues to be a very active area of research for reducing treatment-related uncertainties.

Throughout the past decade, much work has focused on incorporating three-dimensional (3D) and even four-dimensional (4D) imaging in the treatment room.[11–13] Currently, on-treatment kilovoltage (kV) or megavoltage (MV) CT images can be acquired using a dedicated CT scanner within the treatment room[14] or using the inherent imaging capabilities of Tomotherapy units,[15] respectively. In addition, cone-beam CT (CBCT) images can be acquired on conventional linear accelerators by tomographic reconstruction of planar projection images, either using the gantry's MV beam[16,17] or a separately mounted kV x-ray source on the gantry.[18,19] Research has even demonstrated the feasibility of integrating a linear accelerator with magnetic resonance imaging (MRI) for superior soft-tissue visualization during radiotherapy.[20] The assortment of on-treatment imaging modalities further demonstrates the importance of these images to modern radiotherapy.

On-treatment 3D imaging provides sufficient soft-tissue visualization for numerous applications to radiotherapy.[4,13,21,22] For example, routine imaging provides the means to assess changes in tumor shape, volume, or position throughout treatment and has been instrumental in identifying patients that require new or revised treatment plans.[23–26] Furthermore, the ability to directly visualize primary lung tumors has improved the accuracy of patient setup by reducing uncertainties in target localization.[4,17,27] This consequently reduces treatment-related margins, decreases the irradiation of healthy tissues, and enables the safe delivery of escalated doses. As a result, it becomes increasingly possible to improve the generally poor outcomes currently observed for lung cancer patients.

From imaging to target localization

Within the broad scope of IGRT, this dissertation focuses specifically on reducing inter-fractional uncertainties in target localization. A variety of techniques have been explored for this purpose, with methods that can be classified as either manual or automatic. Localization techniques can be further distinguished by their intended region of registration—either direct alignment of the primary tumor or indirect alignment of surrogates of tumor position. The following section begins by highlighting the benefits and limitations of surrogate registration. Current methods of direct target localization are then described, including manual tumor alignment, automatic rigid registration, and deformable registration.

Tumor surrogate registration

Perhaps the greatest benefit of tumor surrogate registration is the reproducibility that results from aligning well-defined and relatively stable structures near the primary tumor. Common surrogates of lung tumor position and motion, for example, include the carina, diaphragm, and spine. These structures are well-visualized and easily registered due to their high contrast in on-treatment images. In a recent study by Higgins *et al.*, alignment of either the spine or the carina provided more reproducible registrations than direct alignment of the primary tumor.[22] Similarly, Mohammed *et al*. established that bony anatomy registration could be just as accurate for simultaneous alignment of multiple treatment targets (i.e., primary lung tumors and involved mediastinal lymph nodes) as direct registration of these targets.[28] In retrospective analyses, surrogate registrations were shown to provide sufficient target coverage during treatment.

These findings ultimately depend on the stability of treatment targets with respect to the registered surrogates, an assumption which does not always hold. Lung cancer patients are prone to substantial variability with respect to the target volume and surrounding anatomy. Many recent studies have reported the potential for significant target volume regression in response to treatment, although tumor growth is also possible.[29–33] The anisotropic nature of tumor regression can cause apparent GTV shifts with respect to the clinical target volume and other local anatomical structures.[34] Another complicating factor is the presence of atelectasis near the primary tumor.[24,35,36] These regions obscure the surface of lung tumors, leading to uncertainties in target definition and localization throughout treatment. Furthermore, as regions of atelectasis progress or resolve, the position of lung tumors may change relative to bony anatomy or other soft-tissue surrogates.[36] Similar effects are observed for patients with pleural effusion, where changes in pulmonary anatomy lead to systematic offsets in tumor position.[24,33] Finally, baseline shifts in tumor position have been reported as a result of changes in respiratory motion.[37–39]

Changes in tumor shape, volume, and position limit the accuracy of target localization based on the alignment of tumor surrogates. To better account for these sources of uncertainty, direct registration of treatment targets is required.

Manual tumor alignment

Guckenberger *et al*. were among the first to report positional uncertainties of intrapulmonary tumors using on-treatment volumetric imaging.[40] Their study included 21 patients with early stage non-small-cell lung cancer (NSCLC) undergoing stereotactic body radiotherapy (SBRT) in 1 to 8 fractions. Patients were first immobilized using a stereotactic body frame (SBF), with kV CBCT images subsequently acquired in the treatment position. The on-treatment image was then matched to the planning CT by manual alignment of the gross tumor volume. Assuming that manual tumor registrations were the ground truth for patient setup corrections, they retrospectively determined systematic and random tumor positioning errors of 7.8 mm and 1.6 mm respectively relative to the SBF, with respective errors of 5.4 mm and 1.3 mm relative to bony anatomy alignment. Maximum errors exceeded 10 mm in both cases.

This demonstrated the importance of volumetric image guidance and direct tumor alignment to improve the accuracy of SBRT.

The group from Princess Margaret Hospital pursued similar end points in two recent studies. Purdie *et al.*[41] assessed 31 SBRT patients in a protocol similar to that of Guckenberger *et al.* above. During each treatment fraction, patient setup was based on direct, manual alignment of the primary tumor. Bony anatomy registrations were also performed retrospectively. In their analysis, the magnitude of discrepancies between these two localization strategies averaged 6.8 mm (90th-percentile: 13.9 mm). This illustrates the potential variability in tumor position relative to surrogates such as the spine.

In a second study, Bissonnette *et al.*[4] stratified a new patient population into two different cohorts: early stage NSCLC patients prescribed SBRT and locally-advanced NSCLC patients receiving conventionally fractionated radiotherapy. They instituted an action threshold of 3 mm and 5°, where patient setup errors exceeding this degree of translation or rotation were repeatedly corrected until the target was localized to within tolerance. Data was reported only after a single round of imaging and setup correction for consistency purposes. For early-stage lung cancer patients, bony-anatomy-based setup resulted in just 16% of all fractions initially within the tolerance limits, compared to 82% of fractions after manual tumor alignment. Similarly, for locally-advanced lung cancer patients, only 30% of fractions were within tolerance after bony alignment. Manual tumor registration increased this percentage to 76% using manual couch corrections and to 84% using remote (automatic) couch corrections. This study demonstrates the potential of volumetric on-treatment imaging for improved patient setup correction and illustrates the feasibility of direct tumor matching.

Despite these benefits, manual target registration suffers from several limitations. First, the studies mentioned above primarily involved SBRT treatments, for which target volume regression and other internal changes are generally not severe. The similarity between on-treatment images and the initial planning CT would thus be expected to facilitate accurate registrations. More substantial changes commonly observed throughout conventionally fractionated radiotherapy may lead to much greater uncertainties in manual registration. As a second potential limitation, primary lung tumors are not always well-visualized in on-treatment images. Guckenberger *et al*. reported 3 out of 21 patients with primary tumors near the diaphragm which were difficult to visualize on free-breathing CBCT images.[40] Tumor borders may also be partially obscured by the mediastinum or surrounding atelectasis. This complicates the registration in these regions and may lead to increased variability in target localization.

A final limitation of manual target registration is the time consuming nature of this process. Studies have reported manual registration times averaging four to five minutes, in contrast to sub-minute execution times necessary for automatic registration algorithms.[22,40] An increase in registration time may lead to subtle changes in the true tumor position relative to that observed in the on-treatment image. As a result, the final setup correction may contain some residual uncertainty. Furthermore, an inefficient setup protocol prolongs the duration of each treatment fraction, which can significantly influence the positional reproducibility of targets by the end of the fraction.[41] Fast and efficient registration algorithms are thus highly desirable to better control target localization uncertainties.

To summarize, manual tumor alignment can provide reliable target localization, but primarily for patients with hypofractionated treatments. Major limiting factors for manual tumor alignment include the time required for registration and large observer variability. For locally-advanced lung cancer patients in particular, configurational changes between multiple primary tumors or metastatic lymph nodes can further complicate manual alignment.[42] As such, automatic rigid and non-rigid registration algorithms provide an attractive alternative for direct localization of lung cancer targets.

Automatic rigid registration

The group from William Beaumont Hospital is one of several that rely on automatic rigid registration of the primary tumor between on-treatment CBCT images and the initial planning CT. Grills *et al*. describe this protocol in a study of 24 patients with peripheral early-stage lung tumors undergoing SBRT.[43] For each treatment fraction, patients were immobilized using either a SBF or an alpha-cradle. Initial setup involved the alignment of either SBF coordinates or skin tattoos with treatment-room lasers. A CBCT image was then acquired and automatically registered to the planning CT using a normalized cross-correlation similarity metric. The registration volume was limited to the extent of the target volume. Using this protocol, they found that initial setup errors of 2 to 6 mm could be reduced to 1 mm or less. Corresponding margins were initially as large as 9 to 14 mm but could be reduced to 1 to 3 mm. This provided a sufficient level of accuracy for delivering highly conformal SBRT treatments.

In a subsequent study, Galerani *et al*. reported on dosimetric improvements from online image-guidance.[21] Following the same protocol for a cohort of 20 SBRT patients, the initial setup would have reduced the dose delivered to 95% ($D_{95\%}$) of the GTV and clinical target volume (CTV) by 2.1% ± 4.4% and 3.5% ± 7.0%, respectively, relative to the planned dose distribution. The dose delivered to 99% ($D_{99\%}$) of the GTV and CTV would have likewise been reduced by 3.2% ± 4.9% and 6.1% ± 10.7%. Using volumetric image-guidance with automatic target registration, the planned and delivered doses agreed to within 0.5%.

Worm *et al*. further demonstrated the potential for automatic rigid registration during routine image-guidance.[9] Their study included 19 consecutive lung cancer patients treated with SBRT using a protocol very similar to the William Beaumont group. Patients were immobilized in a SBF and initially setup according to stereotactic coordinates. A kV CBCT image was then acquired and automatically registered based on the GTV plus an additional 10 mm of neighboring soft-tissue. The magnitude of setup corrections averaged 5.6 ± 1.8 mm. Three patients required additional manual correction following automatic tumor registration, the first due to a particularly small target volume and the other two due to respiratory motion for tumors situated near the diaphragm. A similar study has recently been published by Josipovic *et al*.[44] In their retrospective review, they computed the 3D difference between bony anatomy and automatic tumor registration to be 3.0 mm, ranging from 0.0 to 8.3 mm. They reported no registration difficulties, concluding that GTV-based automatic registration ultimately improved the precision of lung SBRT.

Based on the studies above, automatic rigid registration algorithms provide sufficient accuracy for patient setup corrections during SBRT. These treatments are executed over a period of one to two weeks, during which large internal changes are generally not observed.[29] The resulting similarity between on-treatment images and the planning CT facilitates accurate and robust registration. For conventionally fractionated radiotherapy patients, however, target volume regression and other anatomical changes may be substantial. These large-scale changes complicate automatic rigid registration and can lead to large target localization errors, as demonstrated by the following studies.

Yeung *et al*. reviewed daily CBCT scans for 13 lung cancer patients treated with conventionally fractionated radiotherapy.[7] In their retrospective study, each image was automatically registered to the planning CT using a sub-volume containing vertebrae at the level of the primary tumor. After returning the images to their initial orientation, each image was subsequently registered using a rectangular sub-volume containing the planning target volume (PTV). Visual inspection of the registration showed that the primary tumor "appeared properly aligned," even for patients with substantial tumor regression or reduced atelectasis. Although direct tumor registration reduced setup uncertainties compared to bony anatomy alignment, final margins as large as 5 to 14 mm were still necessary for adequate tumor coverage.

Preliminary work to this dissertation confirmed that bony anatomy alignment resulted in potentially large target localization errors (Appendix I).[45] However, in contrast to the conclusions of Yeung *et al.,* automatic rigid registration failed to significantly improve the localization accuracy of locally-advanced lung tumors. Briefly, a cohort of 17 patients with locally advanced NSCLC received CT scans once per week throughout conventionally fractionated radiotherapy. The initial week-1 CT scan was designated as the planning CT, to which all subsequent images were registered. Images were manually aligned to bony anatomy including the spine, sternum, and ribs at the level of the primary tumor. This resulted in mean 3D displacements of 7.3 ± 5.4 mm in the GTV centroid. Next, automatic rigid registration was performed for the GTV plus a uniform 10 mm margin using a mutual information algorithm (Pinnacle version 8.1y, Philips Medical Systems, Fitchburg, WI). Centroid localization errors were reduced to 5.8 ± 6.0 mm, although the reduction was not statistically significant. The most difficult registration cases were attributed to patients with atelectasis or pleural effusion which either progressed or resolved throughout treatment. For this subpopulation, mean centroid displacements from both bony anatomy and automatic tumor registrations were 9.2 ± 6.9 mm and 7.8 ± 8.8 mm, respectively. In general, substantial changes in target volume and shape, as well as in atelectasis and pleural effusion, were major complicating factors in the rigid registration of locally-advanced lung tumors.

Several modified registration techniques were explored in this study to improve the accuracy of target centroid localization. Although significant error reductions were possible, most of these techniques would require varying degrees of manual interaction in practice, and thus were no longer considered fully automatic. A more ideal registration algorithm should provide fast, fully automatic target localization and should be robust against large-scale changes in target volume and shape, atelectasis, and pleural effusion. The results of Appendix I demonstrated that rigid registration does not meet these criteria for lung cancer patients, and that more sophisticated alternatives must be explored.

Deformable image registration

To better address deforming anatomy and target volume changes throughout conventionally fractionated radiotherapy, deformable image registration (DIR) algorithms could be used. However, in general, computing the deformation between planning and on-treatment images provides much more information than is necessary for simple couch corrections, which only require translational and rotational degrees of freedom. Instead, fully deformable algorithms are much more commonly used for adaptive radiotherapy, where efforts have focused on modifying the initial dose distribution throughout treatment to better conform to a patient's daily anatomy. These efforts in adaptive radiotherapy are outside the scope of the current work. In this dissertation, it is assumed the initial treatment plan is static and will be delivered for every fraction throughout the treatment course.

Few studies have actually explored deformable registration for the specific purpose of patient setup corrections. One example involves the work of Brock *et al*., who developed a biomechanical model-based algorithm for localizing primary liver tumors.[46] These tumors are poorly visualized on CBCT images without contrast and are difficult to register directly. Instead, their algorithm relies on finite-element modeling to deformably register liver contours from an on-treatment image to those of the initial planning CT. The deformation field is then used to estimate the tumor position on the CBCT, from which the required setup correction can be computed. For 12 patients treated in 6 fractions, their algorithm effectively localized the GTV center-of-mass to an average of 1 mm or less in each direction. It is unclear how well this algorithm would extend to lung tumor localization. Online contouring, whether through manual or automated segmentation, may be inaccurate for patients with large pathological or anatomic variability throughout treatment. Furthermore, baseline shifts in tumor position relative to nearby anatomic landmarks would likely lead to larger localization errors than were observed for liver tumors.

Deformable algorithms have several other drawbacks as a potential solution for tumor localization. In general, these algorithms are designed to be accurate in the registration of high-quality images such as diagnostic fan-beam CTs. On-treatment CBCT images demonstrate a greater degree of noise and reduced image contrast, presenting a major challenge to conventional DIR algorithms. Another limitation is the ability of DIR to model large local deformations. For the specific case of primary lung tumors, Guckenberger *et al.* noted severe deformation artifacts in 3 of 13 patients, two with dissolving pleural effusion and the third with resolving atelectasis throughout treatment.[47] Deformable registration accuracy may also be reduced for primary lung tumors that demonstrate “infiltrative” growth patterns. This occurs when a tumor invades or dissolves from surrounding tissues without substantially displacing them. Deformable registration may incorrectly warp surrounding tissues in favor of tumor alignment, potentially leading to dosimetric consequences for nearby risk structures.

Deformable registration algorithms are much more computationally demanding than is necessary for online patient setup corrections. Recent developments have decreased execution times to several minutes or less, with substantial improvements offered by GPU implementations.[48,49] However, introducing specialized hardware into clinical practice may not always be practical. The final and perhaps most important limitation of deformable registration is the lack of effective validation and quality assurance measures for lung cancer targets. These measures are essential in order to guarantee both adequate tumor coverage and the sparing of nearby risk structures.[50]

Block-matching registration

The limitations of manual lung tumor localization include observer variability and the potential for relatively inefficient registrations. Automatic registration algorithms are therefore preferable in terms of speed and reproducibility. Rigid registration provides a straightforward and efficient method for calculating patient setup corrections; however, large localization errors have been reported for patients with substantial target volume regression or changing pathoanatomical conditions, including atelectasis or pleural effusion. Deformable image registration may be better suited for these patients, but existing algorithms are not robust and fast enough for this application.

A more ideal registration tool for lung tumor localization should balance the efficiency and reproducibility of rigid registration with the flexibility of deformable registration. This tool must also be accurate and robust with respect to the many complicating factors in conventional lung radiotherapy. These requirements are met by a sparsely-sampled deformable registration technique referred to as “block-matching”. The following section describes the background and basic formulation of block-matching registration. An overview of block-matching applications to medical image processing is then presented. Lastly, preliminary results are reported for the application of block-matching to lung tumor localization.

Background

Block-matching registration is executed in three predominant steps. The first step involves the identification of sub-volumes, termed “blocks”, in the reference (e.g., planning) image. Blocks may be uniformly distributed throughout the image[51,52] or placed non-uniformly according to distinct image features.[53,54] The choice ultimately depends on the application. Next, each block is independently registered to the moving (e.g., on-treatment) image using a rigid transform, most commonly including translations only. Rotations are typically excluded at this stage for efficiency purposes. Each block registration results in a displacement vector that maps local intensity features between reference and moving images. The set of all (rigid) block registrations yields a sparsely-sampled displacement vector field, illustrating the classification of block-matching as a sparsely-sampled deformable registration algorithm. The final step in this algorithm is to compute the global image registration from the raw displacement field. This is most commonly achieved by regularization and smoothing to obtain a fully deformable registration.[51,55] However, for the specific purpose of tumor localization, the displacement field is reduced to a global rigid transform that represents the required couch shift for patient setup corrections.[56,57]

Block-matching algorithms originated in the 1980s with applications including video compression and motion estimation.[58] More recently, these algorithms have gained popularity in medical image analysis primarily for fast deformable registration. In a series of studies, Rösch *et* *al*. described the development of a block-matching tool for deformable registration of pulmonary anatomy.[59] Their work included the optimization of block placement, including selection and rejection criteria to further improve registration quality.[53] Their algorithm was later used to measure and compensate for respiratory motion.[60] Söhn *et al*. also explored deformable lung registration via block-matching.[52] In their implementation, a uniform distribution of blocks was registered throughout the entire thoracic region. The resulting displacement field was then regularized by minimizing a measure of "deformation energy", which constrained the transform vector field to enforce locally smooth deformations. Similar algorithms were developed by Clatz *et al*., Bhattacharjee *et al*., and Liu *et al*. for deformable registration of cranial and head-and-neck anatomy.[54,55,61] However, none of these studies addressed target localization as a potential application, and none of them considered CBCT images in their registrations, relying instead on high-quality MRI scans.

For the purpose of patient setup corrections, block-matching registration must be capable of computing the nominal rigid registration between images, in which the rigid transform represents a shift of the treatment couch. Ourselin *et al*. provided such a tool, although the application of target localization was not pursued.[56] In their work, a uniform distribution of blocks were registered to obtain a sparsely sampled displacement vector field, similar to the deformable algorithms above. Then, to obtain the optimal global rigid transform, the authors implemented a least-trimmed-squares minimization of the displacement vectors. This algorithm was proven effective in aligning histological slices, computing the mid-sagittal plane for MRI and SPECT images, and performing general multimodality registration between CT and MR images.[57] This work was recently extended as part of the "NiftiReg" deformable registration tool, an open source GPU-based algorithm.[62]

Block-matching for target localization

To date, two different groups have applied a variant of block-matching registration to setup corrections for head and neck cancer patients. Birkner *et al.* relied on the alignment of manually-identified bony landmarks in two-dimensional MV portal images.[63] A principle-component analysis was applied to the resulting displacement vectors to obtain translational, rotational, and deformable measures of the setup inaccuracies. The group of Sonke *et al*. pursued a similar approach in 3D FBCT-CBCT registrations. Referred to as multiple region-of-interest (ROI) registration, their implementation began as a method to explore the degree of deformation present in head-and-neck cancer patients.[64] Eight separate blocks were identified to encompass bony structures such as the mandible and vertebrae. By individually registering each structure, the authors measured a large non-rigid component in patient setup that could potentially exceed existing treatment margins. In a second study, this group extended their registration tool to compute the optimal couch shift for patient setup corrections.[65] Indications for adaptive replanning were also considered. The multiple-ROI registration technique was implemented clinically and revealed as many as 40% of CBCT scans with at least one ROI exceeding 5 mm or 5° from the expected position.[66]

Most pulmonary tumors lack such distinct features to guide block-matching registration. Even when such features may be available, care must be taken to avoid baseline shifts that can range from 3 to 4 mm throughout treatment.[39,42] Thus, the multiple-ROI approach is not considered to be directly applicable for lung cancer patients.

Preliminary results

To assess the feasibility of block-matching registration for localizing primary lung tumors, preliminary data was collected for 15 patients who had received weekly CT scans using an active-breath hold protocol.[67] Using a similar study design as Appendix I, the first weekly CT was designated as the planning image, with all remaining CTs designated as on-treatment images. Each on-treatment image was registered to the planning CT using manual bony-anatomy alignment. Then, six blocks approximately 1 to 10 cm^3 were manually identified on the planning CT along the left, right, anterior, posterior, superior, and inferior tumor borders. Each block was independently registered to the on-treatment image in the Pinnacle treatment planning system using a mutual information cost function. The final aggregate registration was then computed as the vector mean of the block transforms, providing a translational patient setup correction. Rotational corrections were not considered in this study. Target localization errors were defined in this study as the vector distance between center-of-volumes from the planning and on-treatment GTV contours. Initial localization errors from manual bony-anatomy registration averaged 3.0 ± 2.7 mm to 3.8 ± 3.7 mm. After block-matching registration, these errors were reduced to 1.4 ± 1.2 mm to 1.9 ± 1.6 mm. For comparison, whole-target rigid registration resulted in errors ranging from 1.6 ± 1.5 mm to 2.4 ± 2.3 mm for these patients (Appendix I).

One major limitation in this preliminary analysis was the influence of tumor shape and volume changes on the reproducibility of the target centroid position. For example, consider a target volume that demonstrates anisotropic regression in a single predominant direction. A corresponding offset in the target centroid would be observed, even if the remaining cancerous tissue is stationary with respect to surrounding normal tissue structures. The potential bias in centroid position complicates the interpretation of results in this preliminary work.. The remaining analyses in this dissertation do not quantify target localization errors in terms of centroid reproducibility. Instead, studies will rely on measures of target border variability and volume overlap.[68] These analyses will be further described in the following chapters.

Results from this study demonstrated that block-matching registration can potentially provide accurate lung tumor localization. Further improvements are anticipated for a more general block-matching tool, for example, by optimizing the distribution of blocks throughout the GTV. A more reliable set of displacement vectors would be generated, leading to more accurate tumor registration.

Purpose and novelty

The purpose of the current dissertation is to implement and evaluate a block-matching registration algorithm to improve upon existing methods of lung tumor localization. All stages of this algorithm—block placement, block-matching, and target registration—will be assessed for accuracy and robustness in the final tumor alignment. Although block-matching is an established registration technique, the current work is novel in its application of block-matching to the localization of lung cancer targets for patient setup corrections in image-guided radiotherapy. The following section highlights the hypothesized advantages and limitations of block-matching for this purpose.

In contrast to the multiple-ROI registration technique, which relies on bony landmarks in the head and neck, the proposed registration algorithm will rely solely on the similarity of soft-tissue features between planning and on-treatment images. Peripheral lung tumors often contain high-contrast borders with surrounding lung tissue, providing rich image detail for reliable block-matching and robust target registration. However, portions of the target surface may also be obscured for tumors extending into the mediastinum, anchored to the chest wall or diaphragm, or bordering atelectasis. The lack of contrast between the primary tumor and neighboring tissues is anticipated to complicate block-matching in those regions.

Another advantage of block-matching is the efficiency that results from rigid registration of small image sub-volumes. This assumes that deformations in local anatomy can be approximated by a rigid transform. The block size must therefore be small enough for this assumption to apply. However, blocks must also be large enough to contain sufficient tissue structure for meaningful registrations. The balance between these competing factors may be challenging to determine for lung cancer patients, for which substantial changes in tumor shape and volume are possible.

Despite these perceived difficulties, block-matching registration has several key advantages over existing target localization strategies. The intended algorithm is fully automatic, requiring no user interaction during the registration process. This eliminates observer variability and ideally improves the reproducibility of target localization compared to manual tumor alignment. An efficient block-matching implementation may also reduce the time needed for patient setup.

In comparison to automatic rigid registration, block-matching is hypothesized to be at least as efficient by limiting block placement in regions more likely to contribute to an accurate and robust target alignment. In contrast, rigid tumor registration is typically applied to larger image regions containing the entire target volume.[45] Further efficiency gains may be realized from the highly parallel nature of block-matching through multi-core or GPU execution,[62,69] although this is outside the scope of the current work. Block-matching is also likely to be more robust against local deformations, such as those arising from changes in target volume, atelectasis, or pleural effusion. In this case, accurate registration of a majority of blocks is often sufficient for detecting and mitigating mis-registration of the remaining blocks. This reduces the impact of changes in target volume or pulmonary anatomy on the accuracy and robustness of the final target registration.[45]

Finally, in comparison to deformable registration, block-matching is again hypothesized to benefit from faster implementation and increased robustness. Fully deformable algorithms may provide more accurate registration of deforming regions within or around the primary tumor, but at the cost of increased computational complexity. This is unnecessary for computing simple couch shifts, and block-matching is projected to be more efficient in computing patient setup corrections during image-guided radiotherapy. Another advantage of block-matching is that neighboring blocks are independently registered. This may help to reduce the impact of local "discontinuities" between planning and on-treatment images, such as those arising from tumor regression or resolving atelectasis. While these complications may lead to regional failures in deformable image registration,[47] only those blocks in the immediate vicinity of these regions will be influenced, without propagating potential registration errors to other neighboring blocks. Finally, block-matching may actually be more robust against image noise typical of CBCT images, whereas deformable registration can suffer in cases of substantial noise, blurring, or image artifacts.

Overview of dissertation aims

The primary focus of this dissertation is the application and evaluation of a block-matching registration tool for lung tumor localization during IGRT. Major results, analyses, and conclusions have been organized into exclusive manuscripts provided in the appendices. Appendix I includes preliminary work on automatic rigid registration, the limitations of which have motivated the aims of this dissertation. Appendices II, III, and IV provide new contributions reporting on the three specific aims in this work. Chapters 2, 3, and 4 supplement the appendices with further details on project development and analysis. It is intended that each appendix be read prior to its corresponding chapter.

To assess target localization errors resulting from block-matching registration, physician-delineated target volumes will be used as a gold standard. However, target contours cannot be used to directly assess registration errors for individual blocks. The first specific aim therefore involves an important preliminary step to develop a measure of block registration quality. Chapter 2 and Appendix II describe the motivation and methodology behind a deformable surface mesh registration (DMR) tool for this purpose. Briefly, this tool is designed to compute the nominal orientation between tumor surfaces from planning and on-treatment images. This information can then be used to predict the rigid, intensity-based registration of individual blocks. Although DMR is capable of validating the local displacements computed by any general registration algorithm, the focus of Chapter 2 specifically involves the application of DMR as a gold standard for block-matching accuracy.

With this validation tool in place, the next major milestone is to implement a block-matching registration algorithm and to optimize its performance for the localization of primary lung tumors. Chapter 3 and Appendix III describe the major steps involved in this pursuit. First, because block-matching accuracy depends on the presence of distinct soft-tissue features, initial efforts focus on the identification of features that best indicate accurate block registrations. These features will be used to guide block placement on the planning CT. Next, the registration of individual blocks is addressed, with several developments to improve block-matching accuracy for locally advanced lung tumors. Finally, registration of the entire target volume is performed, and the accuracy of lung tumor localization is assessed.

To better evaluate the potential of block-matching registration to improve the setup of lung cancer patients, Chapter 4 and Appendix IV include a comparison study between block-matching and other possible rigid and non-rigid registration algorithms. The primary endpoint for this comparison is the accuracy with which primary lung tumors can be localized for treatment, although other clinical considerations are discussed.

Table 1.1. Overview of patient populations. In general, the first study cohort contained high-quality fan-beam CT (FBCT) images well-suited for algorithm development, whereas the second study cohort contained kilovoltage (kV) cone-beam CT (CBCT) images more representative of a true image guided radiotherapy workflow.

	Study Cohort 1	**Study Cohort 2**
Studies	Specific aim 1 Specific aim 2	Specific aim 3
Patients	18	16
Primary Tumor Site	Locally advanced non-small-cell lung cancer	
Imaging Protocol	Active breathing control	4D audiovisual-biofeedback End-of-inspiration phase only*
Planning Image	FBCT	FBCT
On-Treatment Images	FBCT	kV CBCT
Imaging Frequency	Weekly	Weekly
Duration of Treatment	4 to 7 Weeks	6 to 8 Weeks

*All registrations were performed for three-dimensional image sets.

CHAPTER 2. DEFORMABLE MESH REGISTRATION

Introduction

A major preliminary step in the development of a block-matching registration (BMR) algorithm for target localization is to establish a measure of block registration quality. This measure quantifies the accuracy of individual block registrations, and it enables the block-matching algorithm to be intercompared at various stages of development. A deformable mesh registration (DMR) tool was developed and evaluated for this purpose, the details of which are provided in Appendix II. The following chapter emphasizes the rationale for DMR in the specific context of block-matching and expand on the development of DMR as a validation tool.

To better understand the role of DMR in future BMR development, it is important to briefly introduce the intended block-matching algorithm. Primary lung tumors often contain distinct, high-contrast borders with the surrounding lung parenchyma. By distributing blocks throughout the surface of the primary GTV, it is likely that many of these blocks will lie along distinct borders and will be well-registered between images. The GTV has been delineated by a physician on all image sets for the current study population to facilitate analysis. However, block-matching registration only requires target contours on the planning CT, which are always available as part of the treatment planning process. Prior to block-matching registration, contours will first be used to guide block placement along the GTV surface. Then, after registration, these contours will serve as a gold standard for assessing block-matching accuracy.

The transform generated by DMR is intended to estimate the expected block displacement, enabling the quantification of block registration errors. The major underlying assumption in this validation technique is that changes in the GTV contours are reflective of changes in the local anatomy and pathology.

Although DMR was chosen as the most suitable method for validating block registrations, other methods were also possible. These methods are discussed briefly in Appendix II but deserve further emphasis in the context of block-matching. One major criterion for this validation tool was the ability to compute non-uniform displacements for different regions of the tumor surface. This addressed the anisotropic nature of lung tumor regression.[34] Metrics of target registration accuracy such as centroid alignment, border displacement, and volume overlap indices are therefore not applicable to the task at hand.

A viable alternative and common technique in validating DIR algorithms could be to identify corresponding landmarks between the images.[70] Alignment of these landmarks represents the ground truth for image registration, and interpolating between the landmarks (e.g., using thin plate splines) could be used to estimate the desired block registrations. The biggest perceived obstacle with this approach, however, was the ability to identify a large enough distribution of landmarks in a close enough proximity to the GTV to ensure a reliable ground truth. With the potential for large variations in the GTV and surrounding anatomy, landmark identification could become a laborious and time-consuming process for some patients. Target contours were already available for the current study population, and therefore DMR was chosen as a more practical approach for block-matching validation.

Figure 2.1. The deformable mesh registration workflow. Each transform was optimized separately in succession.

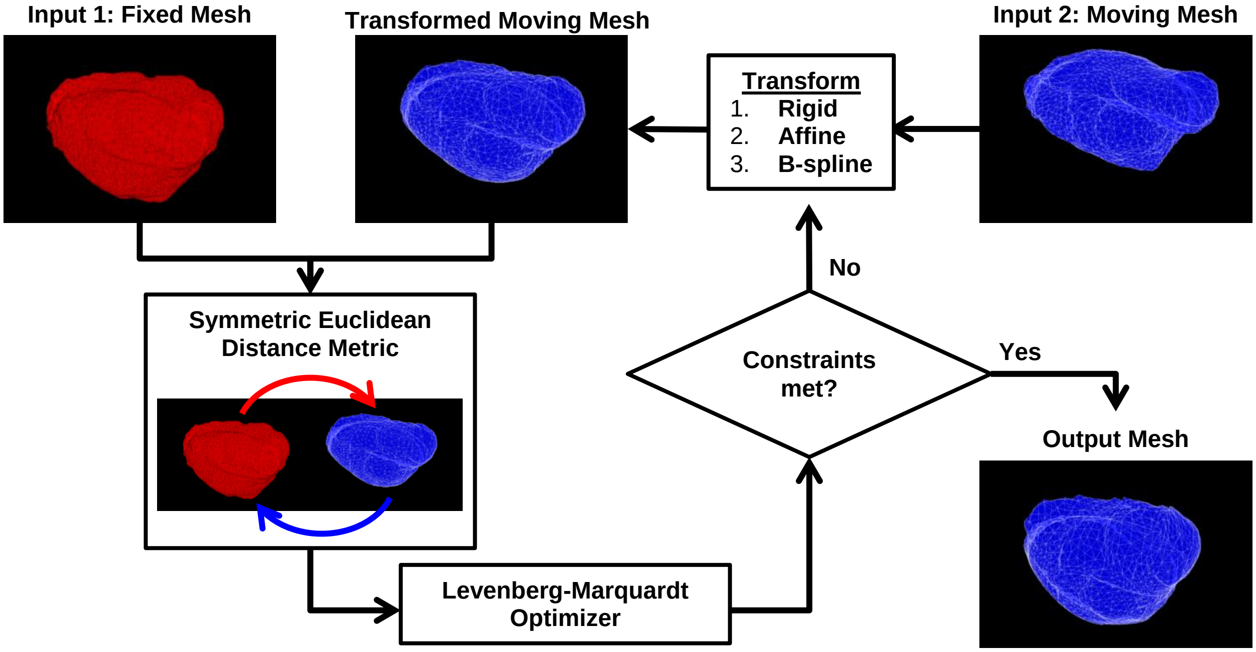

As one final alternative, DIR algorithms could potentially be used as a bronze standard for assessing block-matching accuracy. In theory, the deformation vector field generated from DIR of the primary tumor and surrounding anatomy should agree very closely with the displacements from block matching. Unfortunately, reliable DIR was not possible for all patients in the current study population. Instances of large target volume regression, re-expanding airways, and changing states of atelectasis or pleural effusion all led to DIR errors near the GTV. In contrast, DMR is independent of image intensities and is hypothesized to be more robust against these complications.

As described in Appendix II, the purpose of this work was to implement and assess DMR as a general validation tool for intensity-based registration algorithms. The true motivation, however, was to validate the accuracy of block-matching. This chapter supplements the appendix by focusing on DMR in the context of block-matching validation.

Mesh registration: Implementation and technical details

Deformable mesh registration, more accurately referred to as a point-cloud registration method, requires three major components: a transform, a similarity metric (or cost function), and an optimizer (Figure 2.1). The transform describes the degrees of freedom available in adapting the moving mesh vertices to better match those of the fixed mesh; the similarity metric quantifies how closely the moving mesh agrees with the fixed mesh; and the optimizer updates the transform parameters to drive the similarity metric to an optimum. Specific details of each component are briefly presented below.

Transforms

Rigid and affine transforms

As discussed in Appendix II, three transforms were separately optimized to gradually align a moving mesh, M, with a fixed mesh, F. Let m represent the coordinates of a single point in the moving mesh, $m \in M$, and define m' to be the coordinates of this same point following transform $\mathbf{T}(m)$. For rigid and affine registrations, the transformed point m' is given by

$$m' = \mathbf{T}(m) = R \cdot (m - C) + C + T = R \cdot m + O \,, \qquad [2.1]$$

where R is a rotation matrix, C is the center of rotation, T is the translation, and O is an offset that accounts for the combined effect of both translation and rotation about arbitrary point C. For a strictly rigid transform, R results only in rotations. For the similarity transform actually employed in this work, a single uniform scaling factor, s, is incorporated into the rotation matrix by scalar multiplication, $R_{Similarity} = s \cdot R$. Finally, for the affine transform, the rotation matrix includes the effects of rotation, scaling, and shearing in each orthogonal direction. These parameters specify the transform of any point in physical space. Application of the transform to all points in the moving mesh M results in a transformed moving mesh, M'.

Figure 2.2. Description of a one-dimensional third-order B-spline curve. (a) An individual third-order B-spline curve consists of 4 polynomial segments connected at “knots” (open circles). Its placement in space is specified by a “control point” (closed circle). (b) A fully summed B-spline curve (shown in red) is computed as the sum over all individual B-splines curves. For mesh registration, the B-spline curve represents the transform, $\mathrm{T}(\mathrm{x}, \beta^{\mathrm{n}})$, applied to point x. The shaded region represents the valid region of the B-spline grid, within which the summed B-spline curve is properly normalized. (c) Each B-spline has an associated weighting factor, or “coefficient”, that scales its magnitude. These coefficients are optimized during registration to provide the final transform of all moving mesh vertices to the fixed mesh surface.

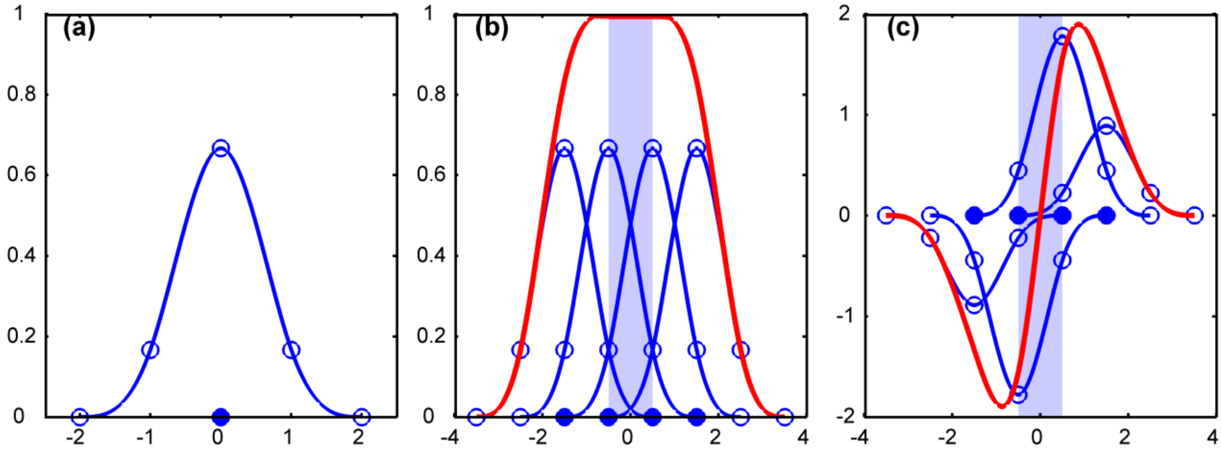

B-spline deformable transform

Unlike the rigid and affine transforms, a B-spline transform is specified within a finite, predetermined region. The results from computing the transform as the weighted sum of a series of individual B-spline curves, $\Sigma_k[w(k) \cdot \beta_k^n(p)]$.[71] Here, $\boldsymbol{\beta}^n(p)$ represents the an n-th order B-spline curve evaluated at point p. (The current work uses third-order B-spline curves, $\boldsymbol{\beta}^3(p)$.) These curves are positioned in physical space by defining a grid of “control points”, where the k-th control point defines the individual B-spline curve $\beta_k^n(p)$. Each curve contains an associated weighting factor, $w(k)$, which is referred to as the B-spline "coefficient". The weighted sum over all B-spline curves evaluated at point $m \in M$ results in the final transform,

$$m' = \mathbf{T}(m, \boldsymbol{\beta}^n) = m + \Sigma_k[w(k) \cdot \beta_k^n(p)]\,, \tag{2.2}$$

Unser *et al*.[71] provides an excellent theoretical review of B-splines. Eilers *et al*.[72] summarize the important properties of *n*-th order B-splines "in a nutshell". Figure 2.2 depicts a third-order B-spline and its application to deformable mesh registration.

The "valid region" of the B-spline grid is defined by the shaded region in Figure 2.2b-c. By definition, all initial points must lie within this valid support region.[72] The B-spline grid is specified to fully enclose the moving mesh, such that all vertices are contained within the valid region. Two parameters are used to compute the spacing between control points in each direction. First, a grid margin expands the mesh bounding box uniformly in all directions. This ensures that moving mesh vertices on the surface of the bounding box are not considered outside the valid B-spline grid region (e.g., due to rounding errors), and this enables the extrapolation of DMR transform vectors outside the surface mesh. Second, the number of control points per dimension, N_{CP}, must be specified. This corresponds to the B-spline grid density, where a denser grid is capable of deformations on a smaller scale. The least-squares optimization routine employed in this work constrains the number of B-spline coefficients to be less than the total number of values in the cost function, N_{CF}. Given that three B-spline coefficients are required per control point (one per dimension), and that an equal number of control points were used in each dimension, the total number of B-spline coefficients required for a given grid density is equal to $3 \cdot (N_{CP})^3$. The B-spline grid density must therefore be specified such that

$$3 \cdot (N_{CP})^3 \leq N_{CF}\,. \tag{2.3}$$

Details of the cost function and optimization routine are further discussed below.

Table 2.1. Summary statistics for tests of two B-spline grid parameters: the grid margin and the number of control points. In tabulating results, the standard deviation was first computed for either all grid margins or all grid densities for an individual patient. A small standard deviation indicated that the given B-spline grid parameter had little influence on the mean, RMS, or maximum target VRE (artificially-deformed meshes) or SSD (physician-delineated meshes). Then, the RMS, 90th-percentile, and maximum standard deviations were computed over all test cases, which included 14 patients from study cohort 1 (Table 1.1).

	Standard Deviation (mm)			Standard Deviation (mm)		
	Mean VRE	RMS VRE	Max VRE	Mean SSD	RMS SSD	Max SSD
Margin Test						
RMS	0.1	0.1	0.4	0.0	0.0	0.2
90%	0.1	0.1	0.7	0.0	0.0	0.3
Maximum	0.2	0.3	0.7	0.0	0.1	0.4
Control Point Test						
RMS	0.3	0.4	7.1	0.1	0.1	2.4
90%	0.6	0.6	9.5	0.1	0.2	3.7
Maximum	0.7	0.8	22.5	0.2	0.3	5.3

Abbreviations: VRE: vertex registration error, SSD: symmetric surface distance, RMS: root-mean-square, 90%: 90th-percentile

Analysis of B-spline grid parameters

The impact of the B-spline grid margin and grid density was evaluated for the primary tumor from week 4 of treatment for 14 of the 18 patients from Appendix II (Table 1.1: study cohort 1). Two patients without reliable deformable image registrations were excluded, as were two patients with too few vertices in the moving mesh for evaluation of more than 5^3 control points. The patient with two primary lung tumors was included, with each GTV separately evaluated. In the first test, a series of registrations were performed with grid margins of 0.5, 2.5, 5, 10, and 20 mm, each using 4^3 control points. Then, a second series of registration were performed with 4^3, 5^3, 6^3, and 7^3 control points, each using a fixed grid margin of 5 mm. Otherwise, all registrations were performed and data collected in the same manner as Appendix II. Vertex registration errors (VRE) were defined for the set of artificially-deformed meshes as the residual distance between corresponding vertices from fixed and registered meshes. For physician-delineated meshes, the correspondence of vertices was unknown between fixed and registered meshes, precluding the computation of VRE. Instead, symmetric surface distances (SSD) were computed to quantify surface agreement. This measure represented the average over all nearest-neighbor distances between the vertices of fixed and registered meshes.[73]

The first aim of this analysis was to determine the variability in registration accuracy resulting from each B-spline grid parameter. In general, a larger variability in VRE or SSD indicated that a given parameter influenced the accuracy of deformable mesh registration to a greater extent. This variability was assessed by computing the standard deviation over all registration results for each pair of fixed and moving meshes. Thus, for each on-treatment target, one standard deviation reflected the influence of various grid margin sizes, and a second standard deviation reflected the influence of different grid densities. The standard deviation was calculated directly from the average, root-mean-square (RMS) and maximum VRE (artificially-deformed meshes) or SSD (physician-delineated meshes). Finally, population statistics were obtained by computing the RMS, 90th-percentile, and maximum of the individual target standard deviations. These final statistics are listed in Table 2..

Figure 2.3. Mean and standard deviation of registration results for B-spline grid parameter tests, computed over 14 patients from study cohort 1 (Table 1.1) for each tested margin size (left column, 4^3 control points) or number of control points (right column, 5.0 mm margins). Top row: vertex registration errors are shown for registrations of artificially deformed meshes. Bottom row: symmetric surface distances are shown for registrations of physician meshes.

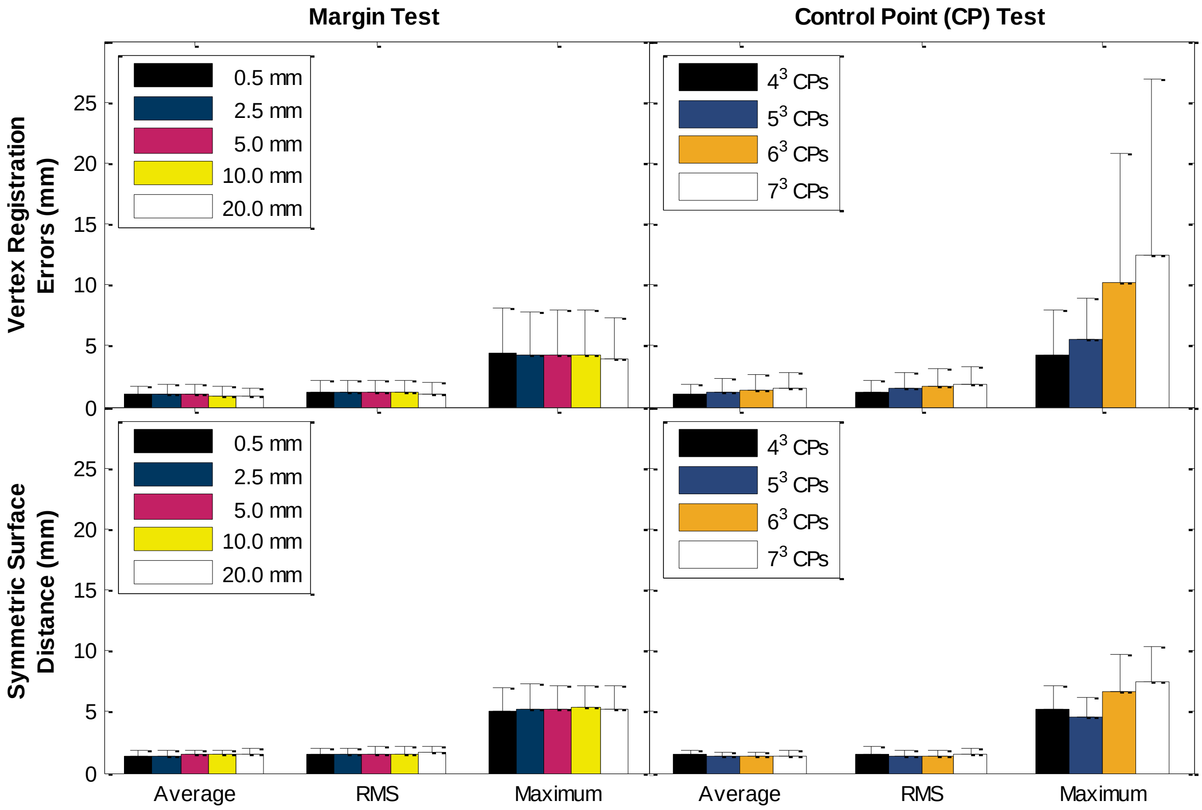

The second aim of this analysis was to assess the total registration accuracy from the combination of a single grid margin and grid density over all patients included in the current sub-population. This provided a population-based analysis to identify the most accurate set of B-spline grid parameters. The net effects of grid margin size and grid density are provided in Figure 2.3.

Table 2. shows that the standard deviation in VRE or SSD from B-spline grid margin tests was less than 1 mm for all patients. The RMS deviation in these results was 0.1 mm or less across all registrations. As shown in Figure 2.3, the mean and standard deviation of the VRE and

SSD were approximately equal for all margin sizes. Therefore, the margin size was considered to have a negligible impact on registration accuracy and was arbitrarily set to 5 mm for all registrations performed in Appendix II. This provided a reasonable expansion from which the DMR transform could be extrapolated during validation of the BMR algorithm.

In contrast, increasing the number of control points resulted in increased VRE (Figure 2.3). The magnitude of the effect was subtle for the average and RMS VRE, but the maximum VRE increased from 4.3 ± 3.6 mm using 4^3 control points to 12.4 ± 14.5 mm using 7^3 control points. Table 2. confirms the presence of large variability in these results, particularly for the standard deviation of the maximum VRE. Figure 2.4 shows the registration results for the patient with the greatest degree of variability in the maximum VRE. These observations were attributed to the fact that a denser B-spline grid provided an increased number of B-spline coefficients, which could have resulted in a transform that over-fitted the mesh models. Thus, the majority of points appeared to be well-registered at the expense of a few large point mis-registrations. For dense grids, regularization of the B-spline coefficients may be required to reduce these large errors.

For registrations of the physician meshes, these trends were not observed for the average and RMS SSD and were less obvious for the maximum SSD. However, it is likely that large registration errors were not as readily detected by the symmetric surface distance metric. Because fewer B-spline control points reduced the magnitude of large registration errors, all registrations in Appendix II were performed using 4^3 control points.

Figure 2.4. Impact of the control point density for an artificially-deformed surface mesh. Left: registered moving mesh (blue) overlaid on the fixed mesh (red). Center: translation vectors demonstrate the vertex registration error (VRE) from fixed mesh points to their corresponding location on the moving mesh. Right: magnitude of VRE on the fixed mesh surface.

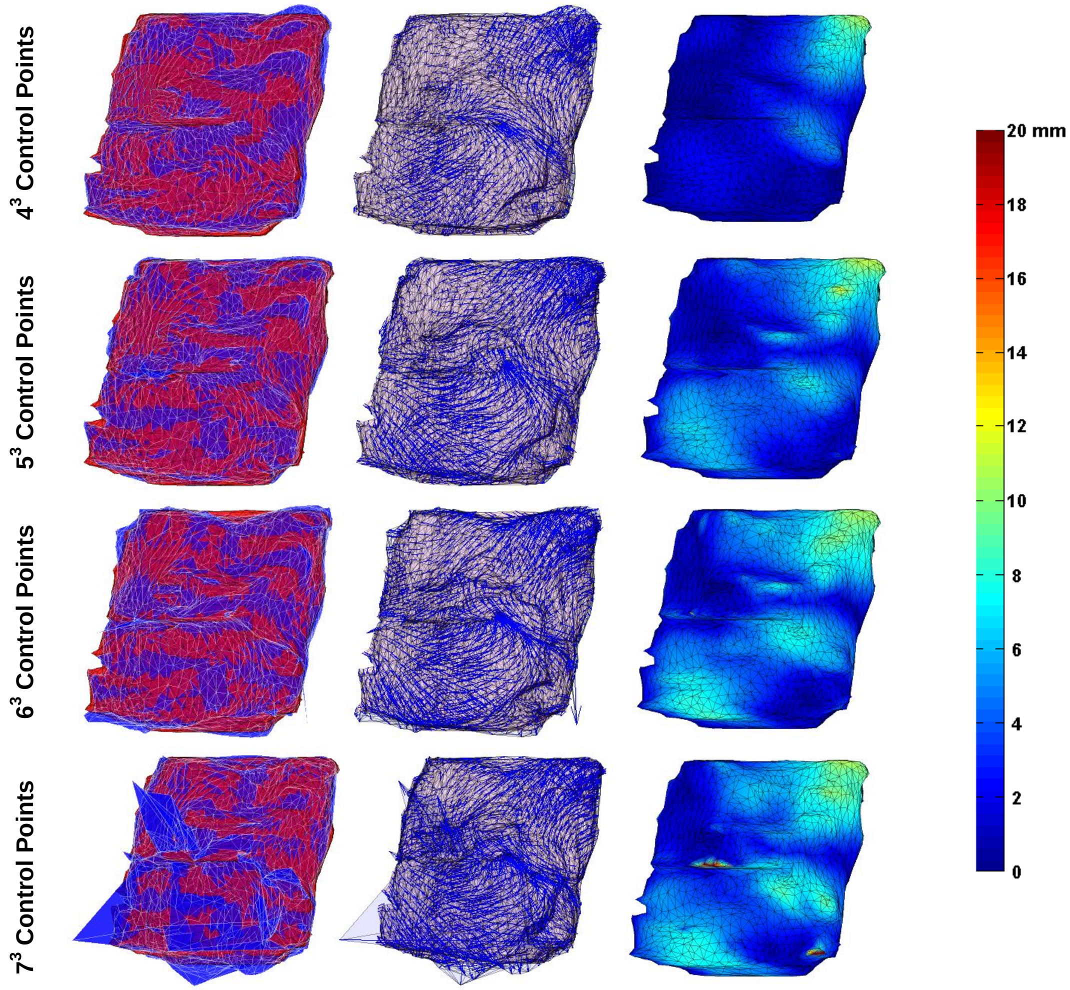

Euclidean distance similarity metric

During deformable mesh registration, the transforms described above are optimized to align the fixed and moving meshes. Assume that the fixed mesh F contains A points denoted f_a, and that the moving mesh M contains B points denoted m_b:

$$F = \{f_a | a \in (1, \dots, A)\},\ M = \{m_b | b \in (1, \dots, B)\}. \qquad [2.4]$$

The similarity between these two point clouds, $S(F,M)$, can be quantified by computing the nearest-neighbor Euclidean distances, as follows.[74] The Euclidean distance between a fixed mesh point, f_i, and a moving mesh point, m_j, is equal to the vector norm between these two points,

$$d(f_i, m_j) = \|m_j - f_i\| = \sqrt{(m_{j,x} - f_{i,x})^2 + (m_{j,y} - f_{i,y})^2 + (m_{j,z} - f_{i,z})^2}\,. \qquad [2.5]$$

From Equation 2.5, the nearest-neighbor ED from any moving mesh point, m_j, to its closest possible fixed mesh point can be defined as

$$d(m_j, F) = \min_{a\in(1,\ldots,A)}\left[d(m_j, f_a)\right]. \qquad [2.6]$$

This leads to the (unidirectional) Euclidean distance similarity metric (EDM), $S(M \to F)$, between fixed and moving meshes, given by the set of nearest-neighbor Euclidean distances for all moving mesh vertices,

$$S(M \to F) = d(M,F) = \{d(m_b, F) | b \in (1, \ldots, B)\}. \qquad [2.7]$$

Of particular interest to the registration process is the similarity $S(M' \to F) = \{d(\mathbf{T}(m_b), F)\}$ between the fixed point set and the transformed moving point set, $M' = \{m'_b\} = \{\mathbf{T}(m_b)\}$. The optimal transform of the moving point set occurs when the set of Euclidean distances, $\{d(\mathbf{T}(m_b), F)\}$, is minimized for the given transform. Optimization will be further discussed in the following section.

For some registrations, EDM resulted in poor agreement of the fixed mesh with the transformed moving mesh. Although the EDM included all moving mesh vertices in the optimization, not all fixed mesh vertices were necessarily considered. This source of error could potentially detract from the accuracy of DMR as a validation tool for block-matching registration and was resolved by modifying the existing similarity measure to produce the symmetric Euclidean distance metric (SEDM), defined as

$$S(M' \leftrightarrow F) = \{d(f_a, M'), d(\mathbf{T}(m_b), F) | a \in (1, \dots, A), b \in (1, \dots, B)\}\,. \qquad [2.8]$$

The SEDM is a set of $A + B$ elements that includes the nearest-neighbor distances of all fixed mesh points to the transformed moving mesh and of all transformed moving mesh vertices to the fixed mesh. Note that $d(f_a, M')$ is not necessarily equal to $d(\mathbf{T}(m_b), F)$.

To assess the impact of the SEDM on mesh registration accuracy, four registrations were performed for each pair of meshes: the "forward" registration with EDM, $S(M' \rightarrow F)$, the "inverse" registration with EDM, $S(F' \rightarrow M)$, the forward registration with SEDM, $S(M' \leftrightarrow F)$, and the inverse registration with SEDM, $S(F' \leftrightarrow M)$. The average, root-mean-square (RMS), and maximum symmetric surface distance (SSD) were computed between the two meshes after each registration. Then, separately for EDM and SEDM registrations, the absolute value of the difference between forward and inverse registration results was computed. Figure 2.5 shows the mean and standard deviation of these results from all patients and weeks of treatment for both the primary tumor and mediastinal lymph nodes (Table 1.1: study cohort 1).

The difference in the average and RMS SSD between forward and inverse registrations was, on average, less than 0.5 mm using either EDM or SEDM. However, using the EDM, the difference in the maximum SSD between forward and inverse (B-spline) registrations was 2.9 ± 3.1 mm for the primary tumor and 1.5 ± 2.2 mm for the lymph nodes. Using the SEDM, these differences were reduced to 0.8 ± 0.9 mm and 0.4 ± 0.4 mm for the primary tumor and lymph nodes, respectively. This shows that the SEDM improved the inverse consistency between forward and inverse registrations with respect to the maximum SSD. It should be noted, however, that SEDM does not guarantee an inverse consistent registration with respect to the transform parameters.

Figure 2.5. Comparison between the unidirectional and symmetric Euclidean distance metrics for the primary tumor (top row) and mediastinal lymph nodes (bottom row). For each pair of registered meshes, the average, root-mean-square (RMS), and maximum symmetric surface distance (SSD) of the forward registration was subtracted by the corresponding result from inverse registration. The mean and standard deviation of the absolute value of these differences were then computed for all patients and weeks of treatment (Table 1.1: study cohort 1).

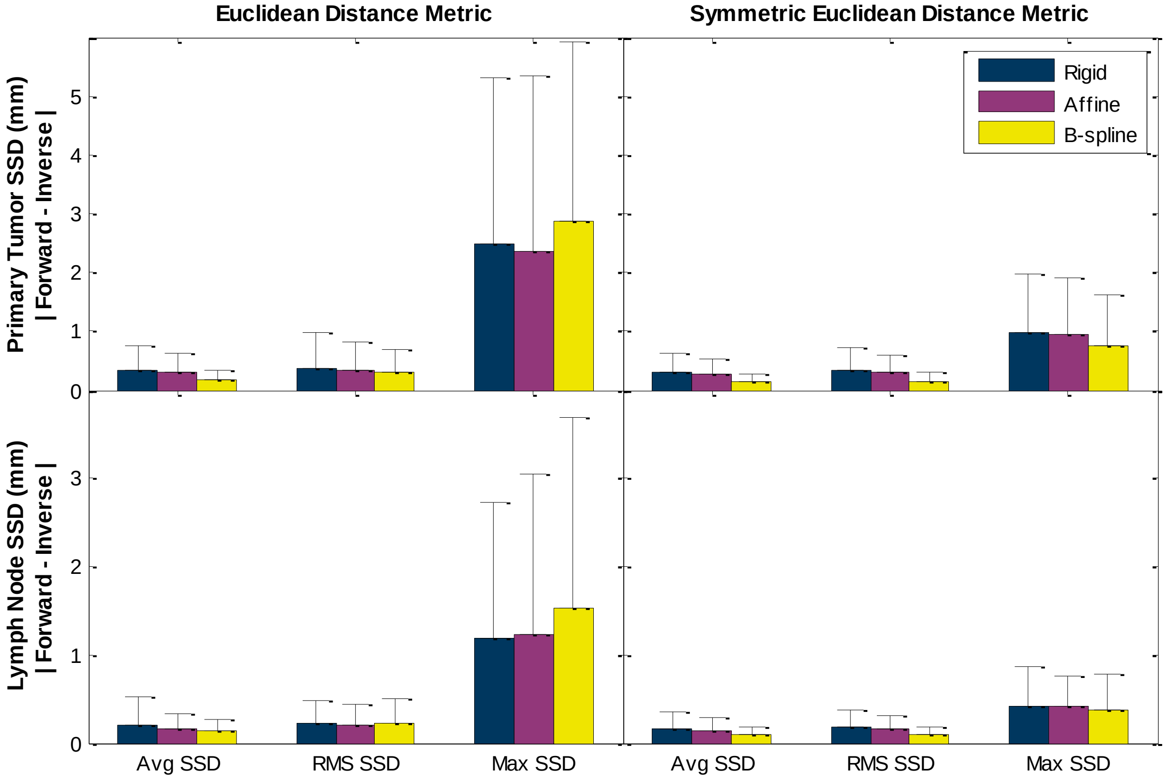

Levenberg-Marquardt optimization

As mentioned above, an optimization routine is required to determine the set of transform parameters, $\boldsymbol{\beta}$, that best aligns the fixed and moving meshes. This is accomplished in the current work using the Levenberg-Marquardt (LM) algorithm, a popular least-squares minimization technique for non-linear problems. The EDM and SEDM may be considered non-linear cost functions due to discontinuities that arise when revised transform parameters alter the nearest-neighbor point-to-point correspondences between the fixed and moving meshes. According to the mesh registration formalism, a transform $\mathbf{T}(M, \boldsymbol{\beta})$ is desired to align two point sets, F and $M' = \mathbf{T}(M, \boldsymbol{\beta})$, as closely as possible. This requires minimizing the square of the SEDM with respect to the transform parameters, given by the following cost function:

$$\Phi(\beta) = \|S(\mathbf{T}(M, \boldsymbol{\beta}) \leftrightarrow F)\|^2 . \qquad [2.9]$$

This cost function may be solved iteratively using a non-linear least-squares optimizer.

The LM algorithm may be thought of as an interpolation between Gauss-Newton (GN) and gradient-descent (GD) methods of least-squares optimization.[75] Both seek to obtain a revised set of transform parameters, $\boldsymbol{\beta} + \boldsymbol{\delta}$, by computing a vector of small corrections $\boldsymbol{\delta}$ during each iteration of the optimization process. Using the gradient-descent method, minimization is achieved by moving in the direction of the negative gradient of the cost-function, with a step size related to the gradient magnitude,

$$\boldsymbol{\delta}_{GD} = -\frac{\partial\Phi}{\partial\beta} = -\left(\frac{\partial\Phi}{\partial\beta_1}, \frac{\partial\Phi}{\partial\beta_2}, \dots, \frac{\partial\Phi}{\partial\beta_k}\right)^T . \qquad [2.10]$$

This typically promotes fast initial convergence down steep cost function gradients. However, convergence becomes much slower for shallow gradients, especially for those often found in the neighborhood of a local minimum. In the Gauss-Newton method, corrections are computed by first-order Taylor expansion, $f(x + \Delta x) = f(x) + f'(x) \cdot \Delta x$, of the cost function, $\Phi(\boldsymbol{\beta} + \boldsymbol{\delta}_{GN})$. This can be written as

$$S[\mathbf{T}(M, \boldsymbol{\beta} + \boldsymbol{\delta}_{GN}) \leftrightarrow F] = S[\mathbf{T}(M, \boldsymbol{\beta}) \leftrightarrow F] + \left(\frac{\partial S[\mathbf{T}(M, \boldsymbol{\beta}) \leftrightarrow F]}{\partial \boldsymbol{\beta}}\right)\boldsymbol{\delta}_{GN} \qquad [2.11]$$

or more simply,

$$S = S_0 + \mathbf{J} \cdot \boldsymbol{\delta}_{GN}. \qquad [2.12]$$

In Equation 2.12, $\mathbf{J} = (\partial S_0)/\partial\beta$ is the Jacobian matrix of the similarity function with respect to the transform parameters. It is computed numerically using a finite difference method, as no straightforward analytic expression exists for the SEDM gradient. Substituting Equation 2.12 into Equation 2.9 and setting $\partial\Phi/\partial\boldsymbol{\delta}_{GN} = 0$ results in

$$\mathbf{J}^T\mathbf{J} \cdot \boldsymbol{\delta}_{GN} = \mathbf{J}^T \cdot S_0 \,, \tag{2.13}$$

from which $\boldsymbol{\delta}_{GN}$ can be computed. The Gauss-Newton method can provide relatively large corrections in shallow gradient regions of the cost function. However, smaller corrections must be made near steep gradients to avoid large extrapolation errors, i.e., in $f'(x)\Delta x$.

Gauss-Newton and gradient descent can be viewed as complementary methods that excel under opposite conditions of the cost function gradient. The Levenberg-Marquardt algorithm improves the overall rate of convergence by prioritizing the method, GN or GD, that is expected to converge more rapidly during the current iteration. Priority is assigned by introducing a scalar parameter, λ, into Equation 2.13:

$$(\mathbf{J}^T\mathbf{J} + \lambda\mathbf{I}) \cdot \boldsymbol{\delta}_{LM} = \mathbf{J}^T \cdot S_0. \tag{2.14}$$

As $\lambda \to 0$, this equation reverts to the Gauss-Newton method given by Equation 2.13, whereas for larger values of λ, the diagonal elements of $\mathbf{J}^T\mathbf{J}$ are more heavily weighted to promote gradient-descent. A set of rules governs the magnitude of λ after each iteration, such that the optimization gradually transitions from GD to GN.

Mesh registration as a validation standard for block-matching

Appendix II briefly asserts that DMR can be a useful tool for general validation of intensity-based registration algorithms. However, mesh registration is particularly suited for validating the block-matching algorithm in this dissertation. As previously mentioned, blocks will be placed on or near the surface of primary lung tumors to exploit the high-contrast gradient between tumors and the surrounding lung tissue. The close proximity of blocks to the surface mesh ensures that DMR will reliably estimate the desired block transform (Appendix II).

Figure 2.6. Comparison of block-matching and deformable mesh registrations. Left: displacements from block-matching registration. Center: displacements from deformable mesh registration. Right: the difference between registration techniques (Equation 2.15). Top, middle, and bottom rows provide axial, coronal, and sagittal views, respectively.

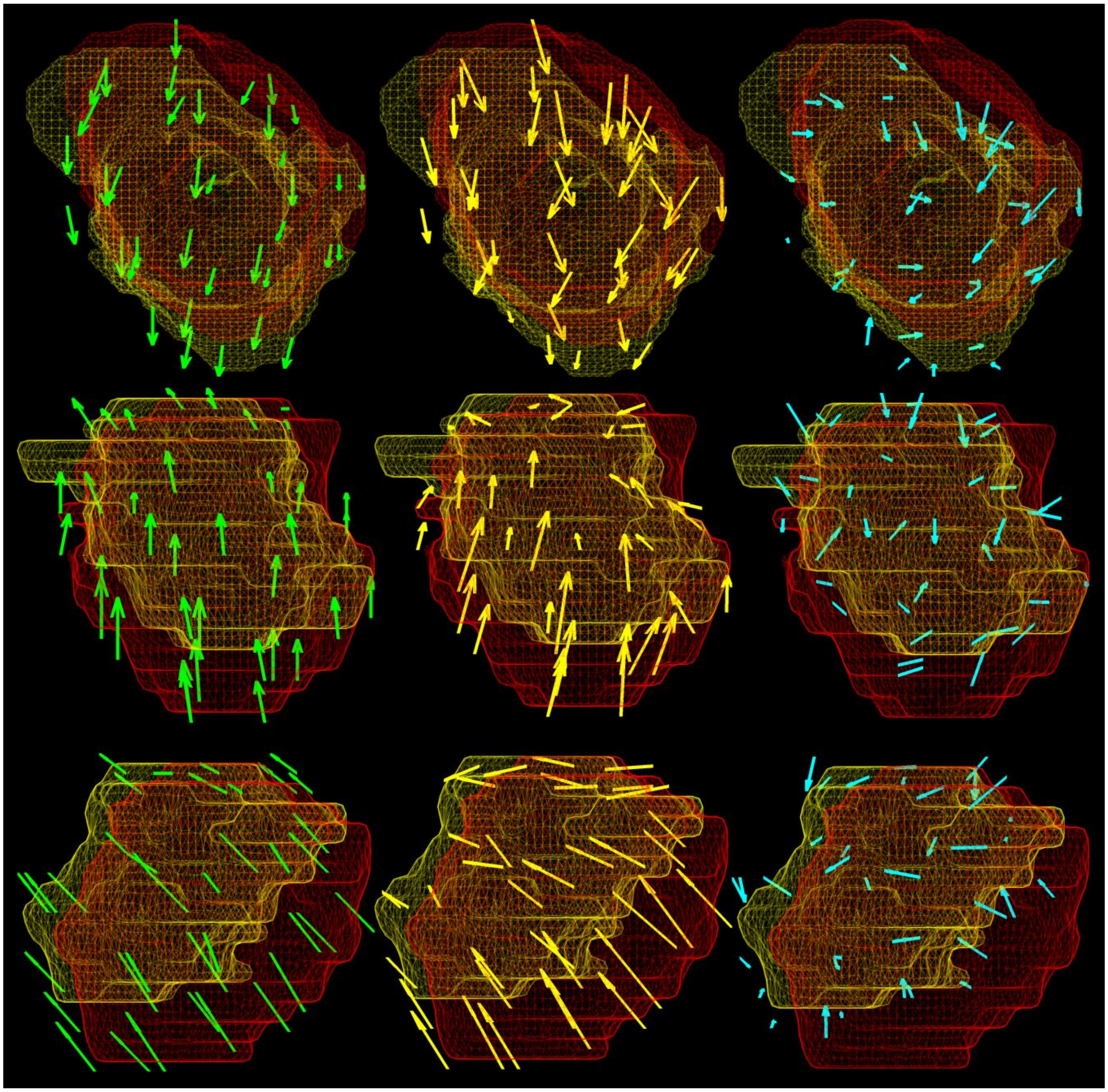

The first important consideration for DMR-based validation involves registration conventions. Specifically, it is necessary to perform the inverse registration of the fixed mesh from the planning CT to the moving mesh on weekly CTs. The associated SEDM is given by $S(F' \leftrightarrow M)$, which emphasizes that the fixed mesh is actually being transformed into the frame of reference of the moving mesh. This convention is consistent with block matching, in which blocks will always be identified on the planning CT and registered to on-treatment images. Each block displacement can thus be directly compared against a transform vector extrapolated from DMR. Given the block-matching transform $\mathbf{T}_{BMR}(b_i)$ for the i-th block centered at point b_i, a second important consideration is how to extrapolate the desired transform vector from DMR. Although the mesh registration was computed between two surfaces, the result is actually valid over a finite region within the B-spline grid (Figure 2.2). A grid margin of 5 mm was used to expand the valid B-spline region, thereby expanding the volume in which the DMR transform could be extrapolated. The mesh transform vector $\mathbf{T}_{DMR}(b_i)$ can be determined for any point within this valid region using Equations 2.1 and 2.2. The discrepancy between the actual and predicted block transforms can then be computed as

$$\Delta\mathbf{T}(b_i) = \mathbf{T}_{DMR}(b_i) - \mathbf{T}_{BMR}(b_i) \tag{2.15}$$

Figure 2.6 illustrates the application of DMR in assessing the registration of a distribution of blocks.

The metric in Equation 2.15 provides a consistency measure between two distinct registrations techniques. However, this should not be mistaken for a measure of absolute error. Although the physician contours serve as the ground truth for GTV localization, discrepancies between block-matching and deformable mesh registration may result from several sources of uncertainty. Variability in target delineation, for example, may cause slight deviations between DMR and BMR.[76] The impact should be less substantial where distinct tumor borders are present but could become larger in less distinct regions around the GTV. DMR also demonstrated vertex registration errors averaging 1 mm for artificially deformed meshes, and registration of physician-delineated targets resulted in symmetric surface distances averaging

2 mm (Appendix II). This limits the expected precision with which DMR can validate block-matching accuracy. Finally, the major underlying assumption in DMR validation was that changes in the GTV contours reflect physical changes in the primary tumor and surrounding anatomy. Systematic discrepancies between DMR and BMR may exist where this assumption is invalid. As a result of these uncertainties, DMR was a considered a bronze standard for block-matching accuracy.

Conclusions

A deformable mesh registration algorithm has been implemented for the purpose of validating intensity-based registrations algorithms, particularly the block-matching registration technique to be explored in the following chapter. This tool requires that contours exist on all registered images and is limited by the presence of both contouring and registration uncertainties. However, based on the current assessment, DMR is capable of generating accurate and reliable local displacements near the tumor surface that will be essential in the evaluation of block-matching accuracy in the following chapter.

CHAPTER 3. BLOCK MATCHING REGISTRATION: IMPLEMENTATION

Introduction

Having established the framework to assess block-matching accuracy in Chapter 2 and Appendix II, the next major aim of this dissertation is to implement a block-matching registration (BMR) algorithm and characterize its ability to localize locally-advanced lung tumors. Appendix III describes the principal components of the BMR algorithm and reports the accuracy of this tool after several important modifications. The current chapter provides supplementary information intended to better motivate developments in the algorithm design. First, a study is conducted to identify optimal image intensity features for block placement. Block-matching is then executed and evaluated based on the deformable mesh registration tool from Chapter 2. Several key results not included in Appendix III are reported here to better motivate each major development in the block-matching algorithm. Finally, the Procrustes analysis is presented, along with advantages and limitations of this approach for target localization.

3.1. Feature identification and block placement

The BMR algorithm in this dissertation was based on an existing open source physics-based non-rigid registration (PBNRR) module from the Insight Segmentation and Registration Toolkit (ITK: version 4.2.0).[54] One of the primary reasons for selecting this code was a feature extraction and block placement module consistent with the intended design of the BMR algorithm in this work. A binary image mask was used to limit block placement to the GTV surface on the planning CT. Each unmasked voxel represented the center of a potential block for registration. For each potential block, the variance of voxel intensities was computed as an estimate of the underlying tissue “structure”, where more accurate registrations were expected for blocks that contained more prominent soft-tissue features. Finally, a user-specified fraction of blocks with the highest variance was extracted for registration, subject to the constraint of a block spacing parameter.

The PBNRR workflow and all corresponding parameters were originally established for fast deformable registration of brain MRIs.[54] It was therefore important to adapt these parameters for the current purpose of lung tumor registration. The following sections summarize a series of tests to establish (1) a suitable block size and similarity metric, (2) an optimal image intensity feature for predicting accurate block registrations, and (3) a reliable strategy for distributing blocks on the planning CT to ensure robust tumor localization.

Block-matching parameters

One of the most important parameters in a block-matching algorithm is the nominal block size.[52,59] Smaller blocks reduce computational complexity and generally contain less deformation for more accurate rigid registration. However, blocks must also be large enough to provide a sufficient level of structural content for reliable registrations, which depends to some extent on the similarity metric. The combination of these two parameters—nominal block size and the similarity metric—have the potential to influence all other components of the BMR algorithm. As such, the purpose of the current evaluation was to determine the nominal block size and similarity metric most suitable for registration of primary lung tumors.

Table 3.1. Nominal and actual block sizes. Differences between the nominal and actual block sizes were the result of including an integer number of voxels in each dimension. Image resolution was 1.2 mm axially (XY) with a slice thickness (Z) of 2.0 mm. Mean relative registration times are also provided for the normalized cross correlation (NCC), correlation ratio (CR), and normalized mutual information (NMI) algorithms.

Nominal Block Size: XY / Z (mm)	Actual Block Size: XY / Z (Voxels)	Actual Block Size: XY / Z (mm)	Relative Registration Time		
			NCC	CR	NMI
5 / 5	5 / 3	5.9 / 6.0	1	2	12
10 / 10	9 / 5	10.5 / 10.0	2	4	16
15 / 15	13 / 7	15.2 / 14.0	6	10	24
20 / 20	17 / 9	19.9 / 18.0	13	21	37

This study relied on the registration of artificially-deformed images for a subset of 12 patients from study cohort 1 (Table 1.1), also described in Appendix III (section II.B.1). Block registration errors were computed as the difference between actual block displacements and the known deformation. To isolate the effect of the nominal block size on registration accuracy, the effects of block spacing and distribution parameters were mitigated by identifying a dense collection of closely spaced feature points within 2 mm of the GTV surface. The same feature point distribution was used in the separate registration of four nominal block sizes (Table 3.1) for each of three different similarity metrics including the normalized cross correlation (NCC), correlation ratio (CR), and normalized mutual information (NMI). Nominal and actual block sizes differed due to the discrete nature of voxel dimensions, as an integer number of voxels was specified in each direction.

Figure 3.1. Block registration errors as a function of block size for normalized cross correlation, correlation ratio, and normalized mutual information cost functions. Registrations were performed using artificially-deformed images for a subset of 12 patients from study cohort 1 (Table 1.1).

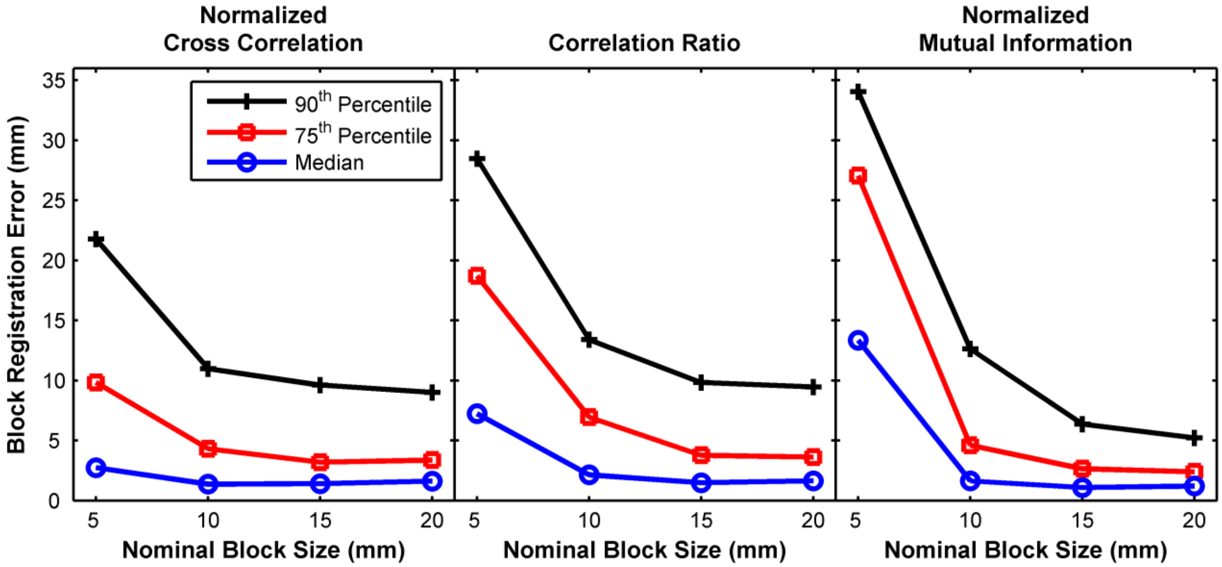

Figure 3.1 shows the median, 75th-percentile, and 90th-percentile of block registration errors as a function of nominal block size. The largest registration errors were noted for 5 mm blocks. The 10, 15, and 20 mm blocks demonstrated a decreasing trend in 75th- and 90th-percentile errors, but median errors varied by less than 1 mm. Although execution times were not a primary endpoint, the fastest registrations were provided by the NCC metric (Table 3.1). CR approximately doubled the execution time, and NMI increased registration times by a factor of 3 to 12. Note that in this preliminary evaluation, similarity metrics were not optimized for efficiency. These results were only tabulated to ensure that the block-matching algorithm was reasonably efficient for a routine clinical workflow.

In choosing an optimal block size and similarity metric, registration accuracy and robustness were most highly prioritized. From this standpoint the 15 mm and 20 mm block sizes demonstrated a slight advantage in reducing large registration errors. However, median errors were equally small for the 10 mm block size, which had the added benefit of improved efficiency (Table 3.1). Therefore, a nominal block size of 10 mm was selected for all following studies.

Finally, in choosing a suitable similarity measure, registration between CT and CBCT images was anticipated to require a multi-modality metric. This requirement was satisfied by CR and NMI, of which CR was approximately 4 times more efficient. Therefore, the correlation ratio was used in conjunction with 10 mm blocks for all subsequent work. These preliminary conclusions were amenable to future revisions as necessary, but these parameters were found to be applicable for the remainder of this dissertation.

Feature detection

Given a reasonable set of initial block registration parameters, the next stage of development addressed the problem of feature detection and block placement. Ideally, blocks should be placed in regions that are likely to be well-registered between planning and on-treatment images. This is possible by identifying image regions that contain highly discriminative intensity features, common examples of which include notable bony landmarks or distinct soft-tissue structures. The placement of blocks in such distinct regions facilitates more accurate block registrations, reduces the number of block mis-registrations, and results in a more robust displacement vector field. The purpose of the following evaluation was to compare four different intensity features in their capacity to predict accurate block registrations. The optimal intensity feature could then be incorporated into the current block placement algorithm.

One common intensity feature is the local intensity variance ("Variance"), which was computed over all voxels in each block. This is the feature detector included as part of the initial PBNRR algorithm,[54] but many other feature detectors were also possible. Because the proposed BMR algorithm in this work relied on block placement near the tumor surface, edge detectors were hypothesized to be robust predictors of block registration accuracy. Included in this evaluation were measures of the gradient magnitude (“Gradient”) and the Laplacian magnitude (“Laplacian”), the respective first and second-order derivatives with respect to voxel intensities within each block.

A final feature detector was chosen to identify corner-like structures, which were anticipated to result in the least ambiguous block registrations. This was quantified using the minimum local gradient eigenvalue (“Eigenvalue”). Let vector $\mathbf{g}_{ijk}$ represent the directional components of the intensity gradient at a single voxel within a given block,

$$\mathbf{g}_{ijk} = \left(g_x, g_y, g_z\right)_{ijk} . \qquad [3.16]$$

The gradient structure tensor for the current voxel is a 3×3 matrix computed as $\left(\mathbf{g}_{ijk}\right)^{\mathrm{T}} \cdot \left(\mathbf{g}_{ijk}\right)$, where the superscript denotes a transposed array. The element-wise summation of the structure tensors was computed for all voxels in a given block,

$$\sum_{i \in X, j \in Y, k \in Z} \left[w_{ijk} \cdot \left(\mathbf{g}_{ijk}\right)^{\mathrm{T}} \cdot \left(\mathbf{g}_{ijk}\right) \right] \qquad [3.17]$$

yielding a matrix representation of the predominant intensity changes within that block. A Gaussian weighting function w_{ijk} was used to eliminate the dependence of the final structure tensor on the image coordinate system, thus enabling the gradient to be determined at arbitrary angles. Eigen-decomposition of the final structure tensor matrix resulted in a set of orthonormal vectors that represented the predominant directions of the intensity gradients within each block. The corresponding eigenvalues indicated the gradient magnitude in each predominant direction. As the minimum eigenvalue increases, a larger intensity gradient is observed in all three orthogonal directions. This indicates that the given block is more likely to contain a corner-like structure.

Figure 3.2. Registration errors as a function of intensity feature values for the voxels contained within each block. Registrations were performed with a 10 mm nominal block size and the correlation ratio similarity metric. Data were categorized into true positives (TP: lower right quadrant), false positives (FP: upper right quadrant), true negatives (TN: upper left quadrant), and false negatives (FN: lower left quadrant).

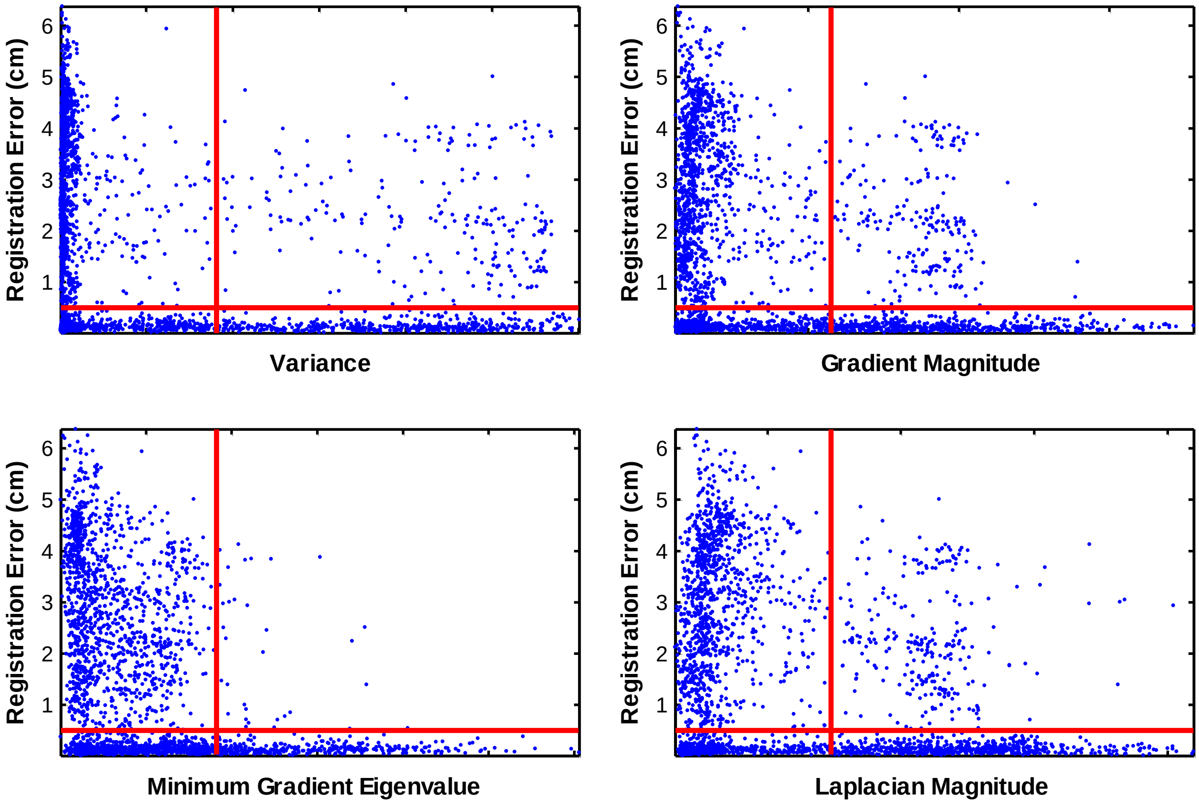

The Variance, Gradient, Laplacian, and Eigenvalue intensity features were compared using the same patient images, block distributions, and registration errors as the previous study. A receiver operating characteristic (ROC)-based analysis was used to distinguish the predictive capabilities of each feature. Block registrations were categorized as “accurate” if registration errors were less than 5 mm and “inaccurate” if registration errors exceeded this threshold. For a voxel size of 1.2 mm axially and 2.0 mm in the slice direction, inaccurate registrations included displacement errors greater than 4 voxels axially, greater than 2 voxels in the slice direction, or equal to 2 voxels simultaneously in all directions. Thresholds of 3 mm and 8 mm were also tested in preliminary work, with no observed impact on the relative results between intensity features. Figure 3.2 shows the classification of block registrations into true positives (TP), false positives (FP), true negatives (TN), and false negatives (FN).

Figure 3.3. Mean positive predictive value (PPV) for four intensity features as a function of the percent of points included in each PPV calculation. Registrations were performed using artificially-deformed images for a subset of 12 patients from study cohort 1 (Table 1.1).

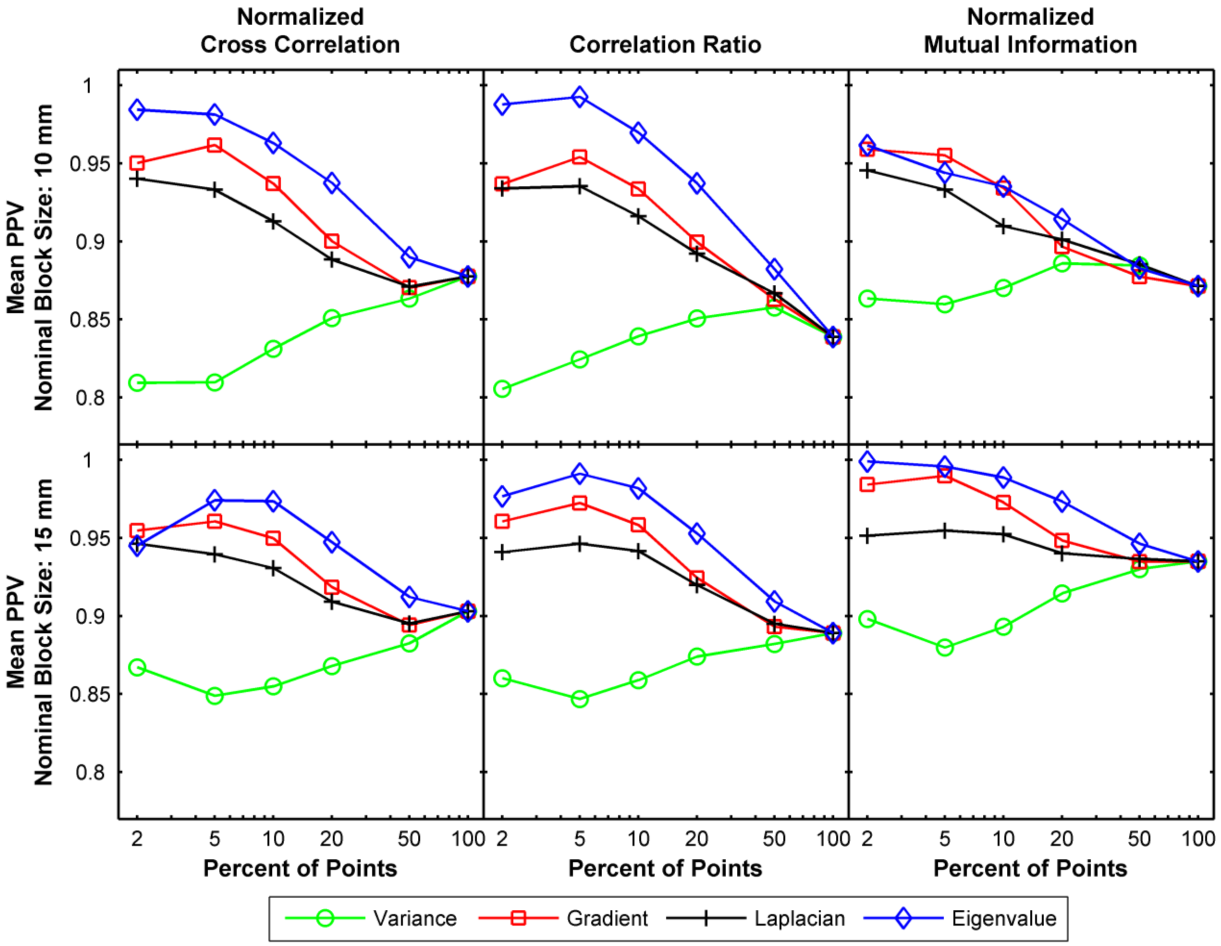

The presence of a large fraction of FN registrations caused a substantial reduction in the sensitivity, or true positive fraction (TPF), defined as TP / (TP + FN). The resulting ROC curve failed to distinguish between the intensity features. Instead, the positive predictive value (PPV) was computed for each intensity feature as TP / (TP + FP). PPV therefore represented that fraction of all blocks containing sufficient structural content (i.e., predicted to be well-registered) that were actually well-registered. A major limitation to this approach was the dependence of the PPV on the intensity feature threshold, which affected the total number of positive blocks (TP + FP) included in the analysis. To extract consistent data for all intensity features, registration errors were separately ranked according the values of each intensity feature. The PPV was then computed for the top 2%, 5%, 10%, 20%, 50%, and 100% of blocks with respect to the ranked intensity features.

Figure 3.3 shows the mean PPV for all patients as a function of the number of blocks included in each PPV calculation. At 100% of blocks, the PPV for all intensity features converged to the same value. This reflected the fact that when all blocks were included in the analysis, the fraction of accurate block registrations remained the same regardless of the intensity feature. The variance measure used in the original PBNRR algorithm resulted in the lowest PPV in this study, regardless of nominal block size or similarity metric. The top 10% of points ranked according to variance had a predictive value less than or approximately equal to that of 100% of points, indicating that feature detection with a variance measure could actually be detrimental to the final registration accuracy. For NCC and CR metrics, the highest PPV was provided by the minimum gradient eigenvalue. This was also demonstrated by NMI registration with a nominal block size of 15 mm, although less evident for 10 mm blocks. Using the combination of CR and 10 mm blocks, the top 5% of blocks with respect to Eigenvalue features were registered with 99% accuracy.

Although the similarity metrics may also be considered intensity features, they were not actually suitable for predicting accurate block registrations. This was because their values were only known after each block was registered. Selection of a subset of blocks would therefore require all blocks to be registered, resulting in a highly inefficient algorithm. Instead, block selection required intensity features that could be computed prior to registration. This enabled a large number of (indistinct) blocks to be discarded to improve the overall efficiency of registration. Furthermore, the remaining blocks were expected to contain high structural content, improving registration accuracy. While the similarity metrics may still provide useful information on the quality of block-matching, that information is best applied after block-matching has completed.

The results of this study support the existing workflow for automatic block identification, namely, sorting blocks according to a measure of distinctiveness and extracting a user-specified fraction of the most distinct blocks for registration. However, in direct contrast to the original PBNRR code, variance was found to poorly predict accurate block registrations. Instead, the minimum gradient eigenvalue is recommended in conjunction with the CR metric and 10 mm blocks. This combination was implemented for all subsequent registrations.

The previous studies relied on the registration of an extremely dense distribution of overlapping blocks, which severely limited the efficiency of the block-matching algorithm. In practice, a much smaller number of blocks are necessary for determining a reliable target registration. By selectively registering only those blocks with distinct intensity features (i.e., according to the minimum gradient eigenvalue), a greater fraction of these blocks is expected to be well-registered. The net result is a more accurate and more efficient block-matching algorithm. The workflow for extracting a sparse block distribution is described in the following section.

Sparse block distribution

A final modification of the block identification paradigm was necessary due to fundamentally different requirements for target localization, as compared with deformable registration provided by the original PBNRR code. Despite the fact that some image regions provided more discriminative structures for block-matching than other regions, the most reliable target localization required that *all* portions of the tumor surface were equally important in the block-matching algorithm. Therefore, feature points were drawn from both distinct and indistinct regions along the tumor surface. Finally, the total number of feature points was not constrained by a user-specified fraction but was given by the maximum number of points that could be identified based on block size and block spacing parameters.

Even with blocks distributed throughout the entire surface, the identification of distinct soft-tissue features was still an important requirement. The order of feature point selection depended on the magnitude of the minimum gradient eigenvalue, but in contrast to Figure 3.3, the final distribution of blocks did not correspond to a percentage of the most distinct blocks. As briefly mentioned in Appendix III, it was desirable that the first few blocks be placed in (i.e., centered on) the most distinct regions of the image. Subsequent blocks could then be placed according to a decreasing measure of distinctiveness until no additional non-overlapping blocks could be placed on the tumor surface. The block placement algorithm was fully automatic, and the block distribution was reproducible.

3.2. Block-matching modifications

Because blocks were distributed throughout the entire tumor surface, registrations were performed for both distinct and indistinct image regions. This increased the probability of block mis-registrations (Figure 3.2), which led to poor initial results as shown by Appendix III, Figures

3 and 4. Evaluation of initial block registration errors motivated two major developments to the BMR algorithm: multi-resolution pyramid registration and the multiple-candidate registrations (MCR) technique. Briefly, the multi-resolution strategy involved the registration of images down-sampled by a factor of 4, down-sampled by a factor of 2, and at full resolution. The coarse-to-fine registration sequence enables efficient and accurate block-matching within a relatively large search window. The MCR technique served to address block mis-registrations that resulted from similar anatomical features located in distinct regions of the search window. In addition to extracting a single block displacement with the maximum similarity score, this method also considers displacements with *near*-optimal similarity scores. The final displacement is then iteratively determined to better reflect local changes at the tumor surface. This section highlights the observations that motivated these improvements as well as the development process that contributed to the final block-matching algorithm.

Pyramid registration: Motivation and implementation

Large block registration errors from the initial BMR algorithm were associated with large displacements that differed substantially from the mean block displacement (Figure 3.4). It was possible to reduce the impact of these large errors by discarding statistical outliers. However, the resulting set of blocks would no longer be distributed uniformly throughout the target surface. To avoid eliminating blocks from the initial distribution, a better solution involved multi-resolution pyramid registration.

Figure 3.4. Relationship between block displacements and registration errors in left-right (LR), anterior-posterior (AP), and superior-inferior (SI) directions. Patients refer to Appendix III, Figure 3 (see also: Table 1.1, study cohort 1).

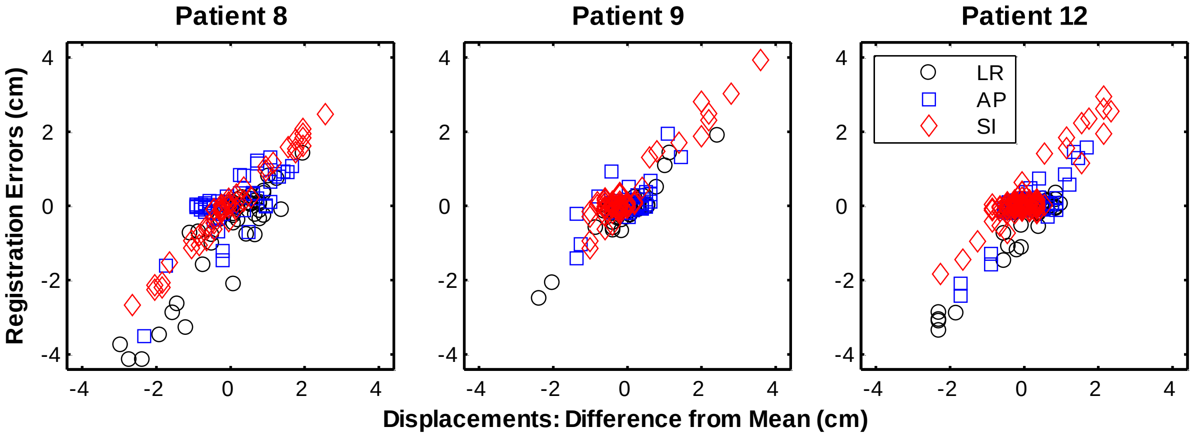

By itself, pyramid registration did not lead to dramatic improvements. In addition to the correlation between large block displacements and large registration errors, it was also observed that registration errors at coarse resolutions impacted the accuracy of higher-resolution registrations (Figure 3.5). To prevent error propagation throughout pyramid registration, displacements were regularized using a median filter.[77] The ability to correct block displacements during registration was a major advantage of the multi-resolution pyramid approach. However, this method required a sufficiently dense distribution of blocks for reliable median filtering, and it was possible that large, accurate displacements were incorrectly modified. In general, eliminating large displacement errors was more beneficial to the total registration accuracy than preserving the relatively small number of large, accurate displacements.

Figure 3.5. Block registration errors (BRE) after registration at coarse, intermediate, and full resolutions for patient 8 (Figure 3.4).

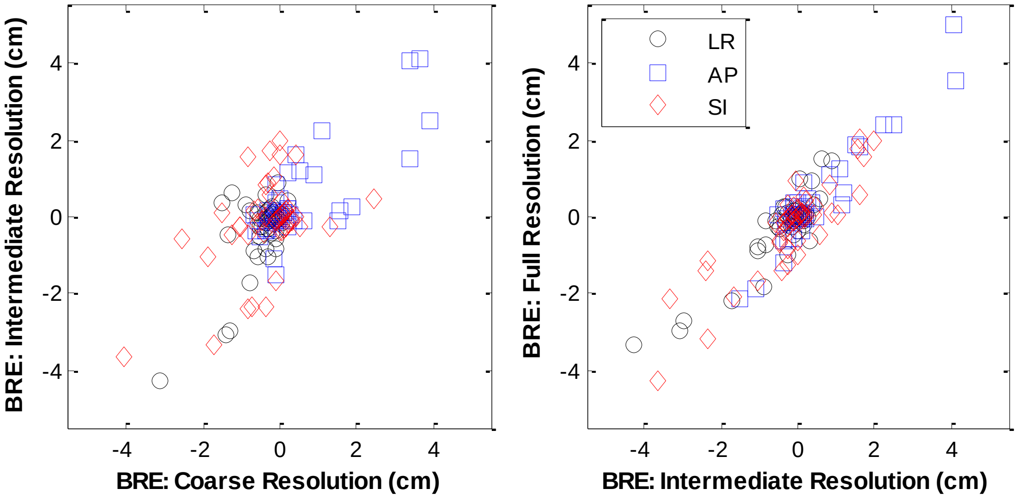

Figure 3.6 demonstrates the registration accuracy of the initial block-matching algorithm ("Initial") compared with pyramid registration without the median filter ("Pyramid-Unfiltered") and with the median filter ("Pyramid-Filtered"). For artificially-deformed images, five patients demonstrated errors of 1 mm from the Initial registration, which remained approximately 1 mm for Pyramid-Unfiltered and Pyramid-Filtered registrations. Of the remaining seven patients, Pyramid-Unfiltered and Pyramid-Filtered registrations reduced mean errors by an average of 1.9 mm and 4.3 mm, respectively. Registration of the weekly patient images better demonstrated the necessity of median filtering. Pyramid-Unfiltered registration reduced mean errors by just 1.5 mm and increased systematic and random errors by 1.2 and 0.8 mm, respectively. In contrast, Pyramid-Filtered registrations reduced errors by 6.3 mm compared to the Initial registration, with reductions in systematic and random errors by 1.7 and 6.9 mm, respectively.

Figure 3.6. Comparison of the initial block-matching algorithm against pyramid registrations with and without median filtering. Registrations were performed for a subset of 12 patients from study cohort 1 (Table 1.1).

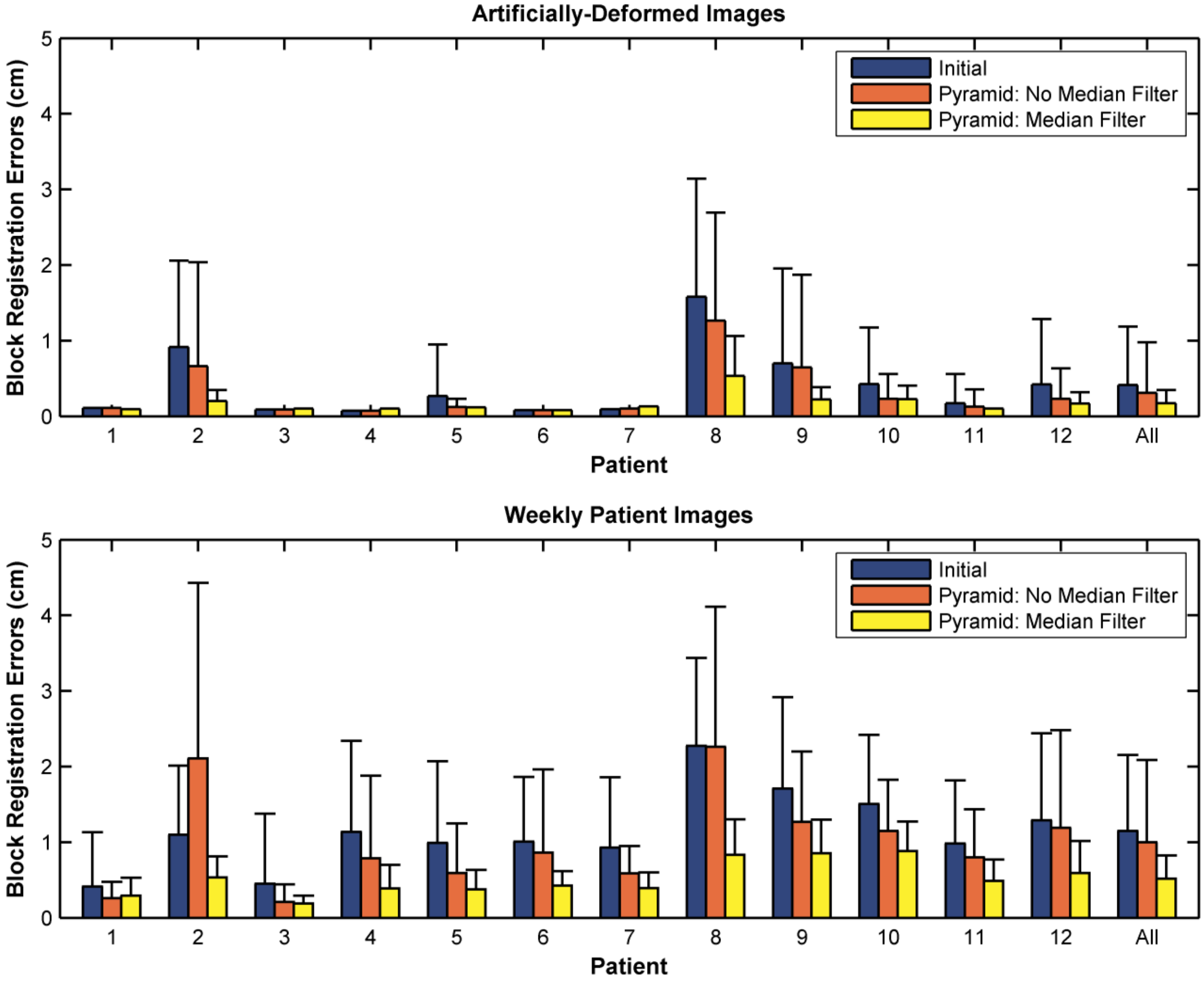

Although pyramid registration with median filtering reduced block-matching errors for all patients, the potential for large registration errors remained. For patient 8, this was attributed to complications in registering a sub-carinal tumor with more substantial deformation (due to anisotropic target volume regression and re-expanded airways) than demonstrated by other patients. For registrations of the weekly patient images, registration errors were computed by comparison against deformable mesh registration (Chapter 2, Appendix II), which introduced an inherent uncertainty of 1 to 2 mm in these results. Additional sources of error were primarily due to block mis-registrations, which motived the exploration of the multiple-candidate registrations technique.

Multiple candidate block registrations

As described in Appendix III, large registration errors were commonly observed for blocks that contained soft-tissue features matching at multiple locations in the search region. Problems arose when the highest degree of similarity (e.g., the maximum correlation ratio) was located in a region distant from the tumor surface. These large errors could be mitigated by median filtering, but the corrected displacement was only an indirect estimate of the desired registration. A better solution was to directly compute the expected registration during block-matching. This was possible by searching for all near-optimal block displacements with respect to the similarity score, then extracting the single displacement which best agreed with those of neighboring blocks. To quantify the agreement between neighboring block displacements, a measure of "local variance" (LV) was computed within each block neighborhood to reflect the consistency of displacement vectors. Large variations in neighboring block displacements, for example due to potential mis-registrations, result in a larger measure of LV. When summed over all possible block neighborhoods, the "total local variance" (TLV) can be used to compare two sets of displacement vectors resulting from the same distribution of blocks. The following formalism illustrates this calculation.

Let each block be defined by the coordinates of its central voxel, b_i. The neighborhood of blocks surrounding b_i was defined in Appendix III as

$$\mathcal{N}(b_i) = \mathcal{N}_i = \{b_j \mid \|b_j - b_i\| < 2 \cdot BlockDiameter\}. \qquad [3.18]$$

Note that block b_i is included in its own neighborhood by this definition. The factor of $2 \cdot BlockDiameter$ was used so that only immediately adjacent blocks (b_j) were considered neighbors. This parameter should be adapted for block distributions that differ from the current spacing. In the following formalism, the number of blocks in neighborhood $\mathcal{N}(b_i)$ is given by N_i, and the total number of blocks in the distribution is given by N.

Assume for now that each block is associated with a single displacement, $d_i = \left(d_{i,x}, d_{i,y}, d_{i,z}\right)$. The set of all displacements in a neighborhood of blocks is given by

$$D(\mathcal{N}_i) = \left\{d_1, d_2, \dots, d_j, \dots, d_{N_i}\right\}. \qquad [3.19]$$

The mean and variance of the displacement vectors in $D(\mathcal{N}_i)$ can be respectively computed (separately in each direction) as:

$$\langle D(\mathcal{N}_i)\rangle_x = \frac{1}{N_i}\sum_{j}^{N_i} d_{j,x} \qquad [3.20]$$

$$\mathrm{Var}[D(\mathcal{N}_i)]_x = \frac{\sum_j \left(d_{j,x} - \langle D(\mathcal{N}_i)\rangle_x\right)^2}{N_i - 1} \qquad [3.21]$$

The local variance can now be defined for the given neighborhood as the scalar sum of the variance in each direction, or

$$LV_i = \mathrm{Var}[D(\mathcal{N}_i)] = \mathrm{Var}[D(\mathcal{N}_i)]_x + \mathrm{Var}[D(\mathcal{N}_i)]_y + \mathrm{Var}[D(\mathcal{N}_i)]_z \qquad [3.22]$$

As the LV_i approaches zero, all displacement vectors within the given neighborhood of blocks become more similar. In contrast, larger values indicate an increased degree of variability in the displacement vectors. Because neighboring regions of the tumor were expected to demonstrate similar displacements, lower values of LV_i were associated with better local registration of the tumor surface. The TLV for all block neighborhoods is given by the sum of the LV for each neighborhood,

$$TLV = \sum_{i=1}^{N} LV_i \qquad [3.23]$$

TLV can be interpreted in a similar manner as the LV. Smaller values indicated that displacement vectors were more consistent across small block neighborhoods throughout the entire tumor surface.

The TLV was designed to compare multiple sets of displacement vectors for the same distribution of blocks. Specifically, this measure can be quickly recomputed for each set of displacement vectors to determine the set with the highest degree of local consistency. This strategy was used to detect the most likely registration for each block from the collection of multiple candidate registrations. Assume that a given block b_i now has a total of n candidate registrations, $\{d_{i,1}, d_{i,2}, \ldots, d_{i,n}\}$. The TLV was recomputed separately for each candidate registration, resulting in the set of TLV measures $\{TLV(d_{i,1}), TLV(d_{i,2}), \ldots, TLV(d_{i,n})\}$. The most likely registration was selected as the one with the minimum TLV,

$$d_i = \underset{d_{i,k}}{\arg\min}\left[\, \{TLV(d_{i,k}) \mid k = 1,2,\ldots,n\} \,\right]. \qquad [3.24]$$

By repeating this process for each block with multiple candidate registrations, it was possible to determine a set of displacement vectors that better registered the target surface, as compared with the initial set of displacements having the maximum correlation ratio. Figure 3.7 provides an example of this iterative process.

The primary advantage of the MCR technique is that it enables the exact calculation of the desired block registrations at the tumor surface. This is superior to regularization (e.g., using a median filter), which indirectly estimates the desired block registration and ultimately depends on the accuracy of surrounding block displacements. However, MCR also has several limitations, including the possibility that none of the candidate registrations provides the desired registration. In this case, the MCR method is not expected to detract substantially from the overall registration accuracy, and median filtering is used to mitigate large block mis-registrations. A second limitation is that convergence of the iterative solution (Figure 3.7) is not guaranteed. To avoid potential non-convergence, several constraints were imposed to limit the number of candidate registrations for each block. In Appendix III, it was found that more than 40% of block registrations resulted in a single possible displacement. These displacements were essential for influencing the selection of all other block displacements to arrive at a unique solution. Finally, although MCR demonstrated substantial improvements compared to the initial BMR implementation, the benefit of MCR was less substantial when used in conjunction with pyramid registration. This was primarily attributed to the larger search window necessary in the initial implementation, which increased the potential magnitude of individual block corrections and resulted in a larger fraction of corrected blocks (Appendix III, Figure 5). Because MCR required a very small percentage of the total registration time and reduced registration errors for patients in this study, MCR was considered to be a recommended approach for improving the robustness of block-matching registration.

Implications for capturing local tumor changes

The above modifications to the block-matching algorithm had several implications in registering small portions of the tumor surface. First, the pyramid down-sampling scheme enabled the registration of both coarse and fine-level details. At the coarsest resolution, a nominal block size of 40 mm enclosed a large portion of both the primary tumor and surrounding anatomy. This generally promoted accurate registrations even in cases of moderate to substantial target volume regression. By progressively registering finer image details, the algorithm could effectively pinpoint the desired block displacements that reflected the true underlying pathological changes. In practice, however, block mis-registrations at coarse resolutions severely limited the accuracy of the algorithm at full resolution (Figure 3.5).

Figure 3.7. One-dimensional example of the multiple candidate registrations iterative workflow. Top: candidate registrations (vertical displacements) are shown for a series of six blocks. Black vectors denote "active" displacements, which initially correspond to the registrations with maximum correlation ratio. Iteration 1: candidate registrations are tested for a single block at a time. Red vectors show modified "active" displacements. These displacements are not actually updated until all blocks have been evaluated for the current iteration. Iteration 2: additional iterations result in further modifications to the displacement vectors. Iterations continue until no more vector modifications are necessary. Bottom: the final set of displacement vectors ideally represents the most consistent spatial configuration.

To more accurately register the tumor surface at each resolution, the algorithm employed the MCR technique followed by median filtering. Both approaches regularized the sparsely sampled displacement vector field, but each method provided unique advantages and disadvantages. MCR was executed first as a method of identifying all near-optimal displacements for each block. The subsequent iterative selection process (Figure 3.7) then identified the set of displacements that best satisfied the local consistency requirement of

Equation 3.24. The resulting displacements therefore reflected some degree of interdependence, in contrast to the completely independent block displacements without MCR. The major advantage of MCR was the ability to replace large initial block mis-registrations (i.e., before MCR) with displacements that better approximated the true changes in the tumor surface (Appendix III, Figure 5). As a potential disadvantage, MCR was still prone to block mis-registrations. The accuracy of MCR ultimately depended on the successful registration of a majority of blocks in order for the iterative selection process to properly converge. Furthermore, even the best registration for an individual block could demonstrate large residual errors. This emphasizes the need for additional regularization, which was provided by a final median filtering step.

The primary benefit of the median filter was to reduce the impact of large block mis-registrations, which served two important roles in the BMR algorithm. First, block displacements computed using low resolution images initialized subsequent registration of higher resolution images. Median filtering therefore improved the initialization of block registrations for all but the first pyramid level. Second, after all pyramid levels had been evaluated, the final set of displacement vectors were likely to contain some residual uncertainties. Median filtering improved the final registration accuracy by reducing these uncertainties. As a potential disadvantage, displacement vectors after median filtering only approximated the true underlying pathological changes. Block registrations were generally close to, but not necessarily equal to, the optimal match with respect to the similarity metric. A second disadvantage was the underlying assumption that large block displacements always corresponded to large registration errors. While this assumption was generally true, it was possible that median filtering incorrectly modified large but accurate block displacements.

One example of this effect was observed for blocks partially containing bony structures. For these blocks, registrations tended to prioritize the alignment of high-intensity bone rather than the surface of the primary tumor. The resulting displacement vector therefore promoted the alignment of rigid objects such as bones. Despite the advantages of such a registration, these displacements could be modified by median filtering to obtain a better approximation of local changes in the tumor surface. This outcome was consistent with the initial design goals of the BMR algorithm. Disabling the median filter would prevent the modification of large, accurate block displacements, but this solution fails to mitigate the effect of mis-registrations. More complex regularization schemes could be devised, but the impact on block registration (and target localization) accuracy was not projected to be substantial.

The combination of multi-resolution pyramid registration, the MCR technique, and regularization through median filtering resulted in reasonably accurate block registrations for both artificially-deformed and weekly patient images, with mean block registration errors of 1.7 mm and 4.8 mm, respectively. These errors were not an indication of target localization accuracy but rather reflected the capacity of the final BMR algorithm to match small regions of the tumor surface. Further modifications to the block-matching workflow were not anticipated to substantially improve block registration accuracy, so final efforts were focused on global image alignment and the assessment of target localization accuracy.

3.3. Target localization via Procrustes analysis

To compute the optimal tumor registration, it was necessary to reduce the sparsely sampled displacement vector field to a set of three translations and three rotations representing a couch shift for patient setup corrections. This was a major departure from the existing PBNRR code. A Procrustes analysis was implemented for this purpose, the advantages and limitations of which are presented in the following section, but first, another potential solution is discussed.

Ourselin *et al*. designed a BMR algorithm for the purpose of fast and robust, general-purpose rigid registration of medical images.[56] Their solution for global image registration involved a least trimmed squares (LTS) method that explicitly accounted for potential block mis-registrations. Briefly, the residual distance between an initial and registered block pair, (a_i, b_i), is given by $r_i = a_i - T(b_i)$, where $T(x)$ represents the global rigid transform of the on-treatment image. This transform is computed such that the sum of squared residuals is minimized. According to the "trimmed" version of least-squares analysis, a given fraction of the largest residuals are excluded from the calculation. This eliminates the influence of outliers on final global registration.

Although robust from a statistical point of view, the LTS method was not optimal for the BMR algorithm in this work, in which it was undesirable to discard blocks from the initial distribution. For reliable target localization, all blocks were required to contribute to the final image registration. Eliminating displacements from a portion of the tumor surface could potentially skew the global image registration in favor of the remaining blocks, leading to suboptimal target localization. A traditional least-squares solution might have been more closely aligned with the current block-matching algorithm, but the Procrustes analysis was pursued as an alternative solution.

The Procrustes solution is a common method of shape analysis that can be used to determine the optimal orientation between two corresponding point distributions.[70] This approach benefits from straightforward calculation of the translations, rotations, and optional scaling parameters in a least squares sense. Scaling parameters do not apply to patient setup corrections, but this information may allow target volume changes to be estimated and tracked throughout treatment. The solution is analytical, requires very little computational time, and can be modified by weighting factors associated with each block. Although outlier displacements will affect the final Procrustes solution, developments in the current BMR algorithm have limited the magnitude of large registration errors to minimize their influence on the final target alignment.

The results in Appendix III highlight the improvements in target localization from BMR with an unweighted implementation of the Procrustes solution. An initial bony anatomy alignment resulted in median and 10th-percentile target volume overlaps of 0.82 and 0.51, respectively. One patient demonstrated no overlap during the final three weeks of treatment. This was due to a pleural effusion that progressed throughout treatment, causing notable systemic offsets in tumor position relative to bony anatomy. After applying the Procrustes solution, BMR increased the median and 10th-percentile volume overlaps to 0.94 and 0.79. A minimum overlap of 0.59 indicated that BMR was a more robust method of primary tumor localization than bony anatomy alignment. BMR also facilitated smaller treatment margins for all patients in the current study population (Table 1.1: study cohort 1), with reductions of 3.5 mm, 6.9 mm, and 5.0 mm in the left-right, anterior-posterior, and superior-inferior directions. Even more substantial improvements were noted for the subset of patients demonstrating atelectasis and pleural effusion.

It may be possible to further improve the Procrustes solution using block weighting factors, for example based on the minimum gradient eigenvalue, correlation ratio, or local variance from MCR. However, because the final displacement vector field is regularized through both median filtering and the MCR technique, it is currently uncertain whether such a weighting scheme would substantially influence the final target registration. This marks an area of potential improvement in the event that future registrations require more accurate target localization.

Conclusion

In this work, the three primary stages of block-matching registration were assessed for the specific purpose of lung tumor localization. Several developments were necessary to improve robustness including more reliable feature detection, multi-resolution pyramid registration, and a novel multiple candidate registration technique. Although the BMR algorithm has only been tested for CT-CT registration, similar results are anticipated for the CT-CBCT registrations that will be explored in the following chapter. The final specific aim involves a comparison between BMR and several other registration algorithms for direct tumor localization. Registrations will be performed for a broader dataset including CBCT images, providing a more clinically relevant assessment of these algorithms.

CHAPTER 4. COMPARISON OF AUTOMATIC REGISTRATION ALGORITHMS FOR LUNG TUMOR LOCALIZATION

Introduction

The previous chapter and the results of Appendix III indicate that block-matching registration (BMR) is capable of robust lung tumor localization. However, these preliminary findings were based on the registration of high-quality computed tomography (CT) images, and improvements were only demonstrated relative to bony anatomy alignment. To establish BMR as a viable tool for online image-guided patient setup, robust registrations must be demonstrated for cone-beam computed tomography (CBCT) images more representative of online image-guided patient setup. Furthermore, it is necessary to compare BMR against other potential solutions for direct lung tumor localization. The purpose of this final study was to evaluate the accuracy of automatic registration algorithms for the direct localization of locally-advanced lung tumors. This study is presented in Appendix IV. In the following sections, the extension of BMR to CT-CBCT registration is first discussed, followed by a summary of the implications of this work.

Figure 4.1. Rigid tumor localization resulting from four automatic soft-tissue-based registration algorithms. The primary gross tumor volume (GTV) is shown for the planning CT (yellow) and CBCT (blue). For block-matching, SICLE, and Demons, deformation vectors were computed at the surface of the GTV, from which the global rigid transform was computed. Differences between these images were the result of rigid shifts alone.

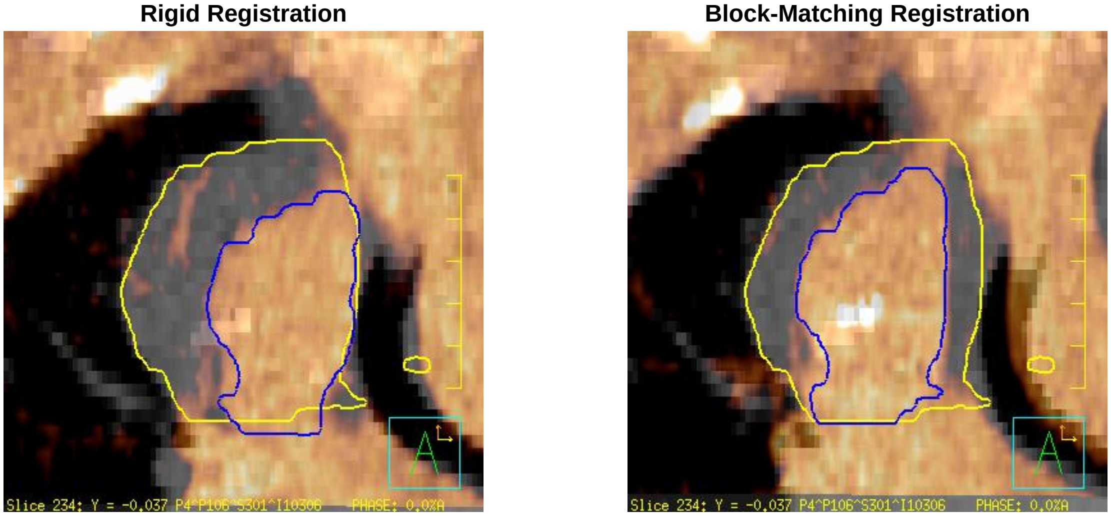

Rigid Registration

Block-Matching Registration

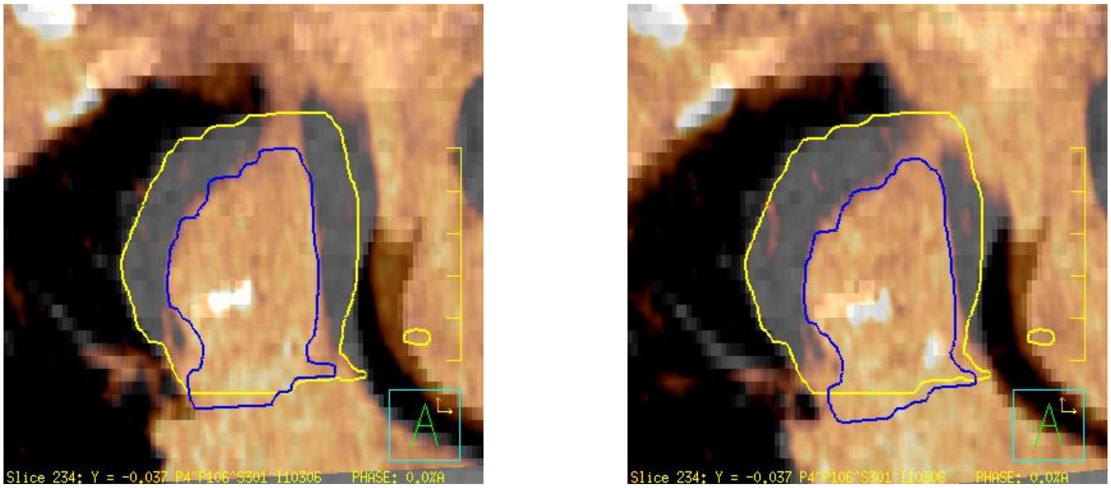

SICLE

Demons

Block-matching registration for CBCT images

Figure 3.4 shows an example of the automatic soft-tissue-based registrations included in Appendix IV. For rigid registration, the translations and rotations were computed directly. For the remaining registrations, it was necessary to reduce the resulting displacement vector fields to a global image transform. This was accomplished by applying the Procrustes solution to displacement vectors computed at the surface of the target on the planning CT. Thus, regardless of the complexity of the various registration algorithms, the final comparison addressed target registration errors due to rigid shifts alone.

All automatic registration algorithms significantly improved target volume overlap (VO) compared to the initial bony anatomy alignment. This highlights the importance of computing setup corrections based directly on the primary tumor, as opposed to tumor surrogates. BMR significantly improved target VO over all other automatic registration algorithms. The minimum VO for BMR was 0.61, whereas the minimum VO for the other algorithms ranged from 0.23 to 0.34. This further illustrates the robustness of BMR in localizing primary lung tumors. Finally, BMR required the smallest overall treatment margins, which averaged 11.7 mm in all directions. The remaining algorithms required margins ranging from 12.8 to 14.9 mm on average. The accuracy and robustness of BMR makes this algorithm appealing for routine clinical use. However, with treatment margins still exceeding 10 mm, purely rigid shifts were unable to account for all sources of inter-fractional variability throughout treatment.

While the primary goal of Chapter 3 was to develop an accurate and robust BMR algorithm, additional consideration was given to the efficiency and versatility of the algorithm. This was reflected in the choice of the correlation ratio (CR) as a reasonably efficient similarity metric that was also capable of multi-modality registration.[78] This metric is similar to the correlation coefficient, but rather than computing linear relationships, CR quantifies functional relationships in the data. Therefore, differences in the intensity values of CT and CBCT images were not expected to affect block registration accuracy.

Another potential complicating factor was the presence of increased noise and reduced contrast in CBCT images. These factors reduced the clarity of distinct tissue features, potentially increasing the proportion of block mis-registrations. Optimization of the block-matching algorithm specifically for CT-CBCT registrations remains the subject of future work. As shown in Figure 4.2, the volume overlap for registrations in Appendix IV was significantly lower than results from CT-CT registration in Appendix III (Wilcoxon rank sum test, $p < 0.001$). These differences must be interpreted with caution, however, as multiple factors were likely to contribute. For example, images were acquired in the previous study using an active breath-hold protocol, whereas registrations in the current study included the end-of-inspiration phase image from four-dimensional scans. Furthermore, delineation uncertainties are generally larger on CBCT images due to decreased visualization of soft-tissue borders.[79] The results of this study may therefore include a greater degree of uncertainty in target definition. Finally, volume overlap differences could be a direct result of differences in target volume regression or shape change throughout treatment. A more conclusive comparison between CT-CT and CT-CBCT registrations would require evaluation of both registration types for the same patient cohort. Despite the fact that improvements in the BMR algorithm may be possible for CT-CBCT registrations, the current implementation still provided the most robust results in Appendix IV and demonstrated significantly greater overlap than all other automatic registration algorithms. Modifications to the current algorithm would only serve to further distinguish BMR as the recommended approach for localizing locally-advanced lung tumors.

Figure 4.2. Differences in target volume overlap between study cohorts (Table 1.1). Study cohort 1 included CT-CT registrations, whereas study cohort 2 included CT-CBCT registrations. Although these cohorts were not directly comparable, significant differences highlighted the potential for reduced CBCT image quality to negatively impact the accuracy of block-matching registration.

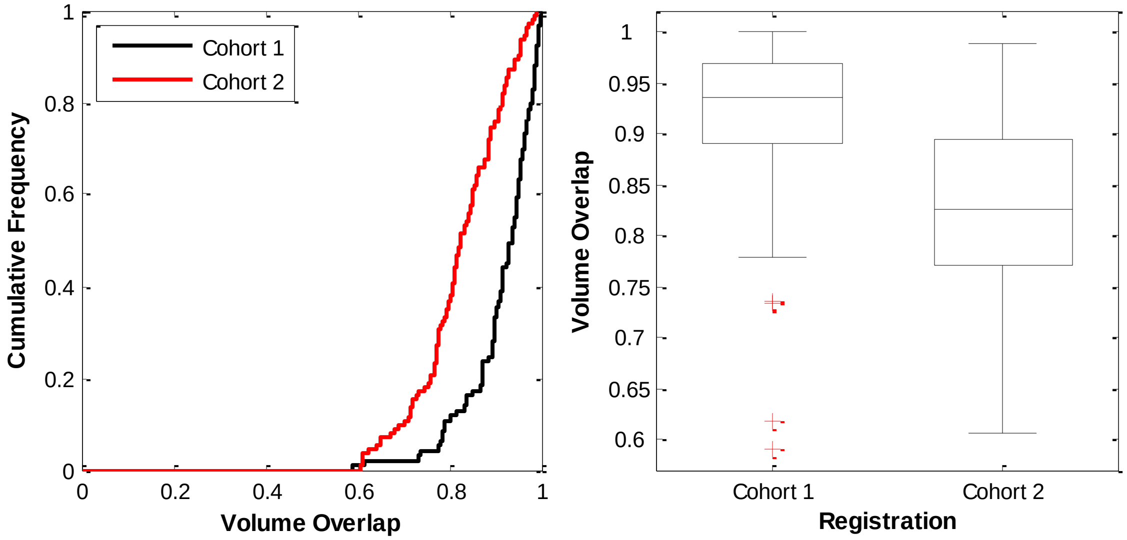

Implications and future direction

In addition to the demonstrated improvements in lung tumor localization, BMR may provide a wide assortment of other benefits to image-guided patient setup corrections. This algorithm is fast and efficient to implement, yet provides a wealth of information throughout the registration process. This has several implications that may help to further reduce inter-fractional uncertainties throughout treatment.

Simultaneous registration of multiple targets

To this point, analyses have only considered the alignment of the primary lung tumor resulting from intensity-based registration of blocks on the tumor surface. Because such small portions of the planning and on-treatment images were included in the registration, the final tumor alignment cannot guarantee that other structures in the thorax are properly aligned. These uncertainties can lead to under-dosing of other cancerous lesions (e.g., mediastinal lymph node involvement) as well as over-dosing of risk structures. For reliable setup corrections in a true clinical setting, the block-matching algorithm must incorporate these additional structures into the final registration.

The fast and efficient nature of BMR should lend well to the simultaneous localization of multiple structures. For patients presenting with two or more primary lesions, blocks can be distributed throughout the surface of each individual target. Then, after all blocks have been registered, one of several aggregation strategies may be employed. It is possible to perform the Procrustes analysis for all blocks simultaneously, although targets with a greater number of blocks will have a greater influence over the final registration. A second and more preferable option may be to compute a weighted Procrustes solution, with weighting factors computed to remove the influence of different tumor sizes. As a final option, the Procrustes analysis could be performed for each individual target, from which the simultaneous alignment of all targets may be obtained.

In addition to the registration of multiple primary tumors, these methods may also extend to the registration of metastatic lymph nodes or neighboring risk structures. BMR could potentially be used to register each target directly. However, it is equally possible that each different target benefits from a unique registration strategy. As an example, registration of the carina has been recommended as a reliable surrogate for mediastinal lymph nodes.[68] A reasonable patient setup correction could potentially incorporate BMR-based alignment of the primary tumor and carina-based alignment of the mediastinum. Although such studies remain the subject of future work, the versatility of the BMR algorithm provides much flexibility in registering multiple structures simultaneously.

Identifying tumor trends

Each of the three stages of BMR (feature identification, block-matching, and target localization) provides important information related to the final tumor alignment. This information may also be useful for detecting trends in tumor position or volume over time. Examples of useful information include the minimum gradient eigenvalue from feature detection, the correlation ratio from block-matching, or the total local variance from the multiple candidate registrations technique. While these measures may not be particularly meaningful for individual blocks, more reliable statistics could be obtained by averaging over the entire block distribution. Changes in this data over time could then be used as an indicator of potential tumor changes, leading to timely clinical decisions that could help to reduce uncertainties throughout treatment.

The Procrustes analysis provides two additional noteworthy quantities. The first is a measure of relative scaling between the initial and registered block distributions. This parameter does not influence the accuracy of target localization, but it could potentially be used to estimate tumor growth or regression throughout treatment. The second measure represents how closely the registered block distribution matches the initial distribution. Known as the Procrustes distance, this measure is computed as the square root of the sum-of-squared distances between all corresponding initial and registered block pairs. Large deviations in this measure throughout treatment may indicate corresponding changes in tumor shape. Correlation studies or receiver operating characteristic (ROC)-based analyses (Chapter 3) could be used to elucidate these trends in future work.

Reducing treatment margins

As acknowledged in Appendix IV, treatment margins were undesirably large even after robust localization with BMR. This is not necessarily a limitation of the current BMR algorithm but rather indicates the inability of rigid couch shifts to correct for all sources of inter-fractional variability. Adaptive radiotherapy (ART) may be required to further reduce treatment margins.[39] However, ART is not always indicated for improving the efficacy of treatment delivery. Tanyi and Fuss found that routine image-guidance increased the frequency of adaptive re-planning at their oncology center, but that less than a quarter of patients required plan modifications.[23] Woodford *et al*. observed that for ART to benefit outcomes for lung cancer patients, a 30% or greater reduction in the target volume was necessary within the first 20 treatment fractions.[80] For patients not meeting this requirement, an accurate and robust target registration tool is essential to ensure that the initial static treatment plan is adequately delivered. It is therefore anticipated that high quality target localization, such as provided by the current BMR algorithm, will remain an important part of image-guided radiotherapy.

Conclusion

Block-matching registration is a promising approach for high-quality localization of locally-advanced lung tumors. In addition, this tool may be useful in identifying patient and tumor-specific trends to influence clinical decisions throughout treatment. Before implementing this tool in a clinical setting, further assessment is needed for simultaneous registration of multiple treatment targets and risk structures.

CHAPTER 5. CONCLUSION

This dissertation focused on the direct, automatic registration of primary lung tumors to reduce target localization uncertainties throughout image-guided radiotherapy. By reducing these uncertainties, it becomes possible to decrease the size of treatment margins without sacrificing dosimetric target coverage. Smaller treatment fields spare a greater volume of normal tissue from radiation-related toxicities, enabling more aggressive doses to be delivered to the patient and potentially improving outcomes for advanced-stage disease.

Safe dose escalation requires that normal tissues are adequately spared from excess radiation during treatment and, even more importantly, that primary tumors are well-localized within the highly conformal radiation fields. Therefore, accurate and robust target localization is essential to safe dose escalation. Postulating that the most reliable tumor alignment is obtained through direct target registration, preliminary research was conducted to assess automatic rigid registration of lung cancer targets. As demonstrated in Appendix I, rigid registration resulted in poor lung tumor localization, especially for patients with large target volume regression, atelectasis, or pleural effusion. A more complex registration algorithm was necessary to capture potentially large internal changes often demonstrated by lung cancer patients. This motivated the implementation and evaluation of a block-matching registration (BMR) algorithm as the primary focus of this dissertation. Chapter 1 introduced the rationale for this approach and the intended algorithm design.

To ensure that individual blocks were accurately registered, a gold standard was required for computing local deformations near the tumor surface. Chapter 2 presented a deformable mesh registration (DMR) tool for this purpose that was capable of registering the tumor surface with an average error of 1 to 2 mm. The deformable transform could also be extrapolated up to 2 voxels away from the tumor surface with only marginal reductions in registration accuracy. These results indicated that DMR is a reliable validation standard for BMR when blocks are placed near the physician-delineated tumor surface. One limitation of DMR in this capacity was that mesh registration errors could potentially contribute to the magnitude of block registration errors. However, this contribution was observed to be relatively small and did not impact the interpretation of block matching results.

In Chapter 3, the BMR algorithm was implemented with careful attention to each stage of the registration process. First, the minimum eigenvalue of the local intensity gradient was shown to predict the greatest fraction of accurate block registrations. This measure was used to guide the placement of blocks in order of decreasing distinctiveness, with the first blocks containing prominent soft-tissue features and the final blocks confined to less prominent regions. Next, evaluation of block registration errors motivated two major revisions to the initial code, including multi-resolution pyramid registration and a novel multiple-candidate-registration technique. Median filtering was also included to regularize block displacements, further improving registration accuracy. Finally, a Procrustes analysis was used to compute the nominal global tumor registration, corresponding to the couch shift for patient setup correction. Compared to an initial bony anatomy alignment, substantial improvements in target localization accuracy were observed for all patients regardless of changes in target shape, target volume, atelectasis, or pleural effusion.

Chapter 4 involved further evaluation of the BMR algorithm against other potential solutions for direct, automatic target localization during image-guided radiotherapy. In this analysis, BMR provided significantly better target volume overlap than all other registration algorithms. Furthermore, BMR provided the most robust target alignment as the only algorithm without any failed registrations. Based on the reproducibility of tumor borders, BMR required the smallest treatment margins averaging 11.7 mm in each direction. Block-matching was thus the recommended algorithm for automatic registration of locally-advanced lung tumors.

Despite providing superior target localization, BMR still resulted in relatively large treatment margins for the given study population. Registration uncertainties contributed to these large margins, but the predominant source of uncertainty was attributed to variability in tumor shape and size throughout treatment. This demonstrated that couch shifts alone could not account for all sources of inter-fractional uncertainty, and that adaptive radiotherapy may be necessary to address more substantial changes. Future work is needed to differentiate between cases that require plan adaptation to improve patient outcomes and those for which high-quality target localization is sufficient.

REFERENCES

[1] F.-M. Kong, R. K. Ten Haken, M. J. Schipper, M. A. Sullivan, M. Chen, C. Lopez, G. P. Kalemkerian, and J. A. Hayman, “High-dose radiation improved local tumor control and overall survival in patients with inoperable/unresectable non-small-cell lung cancer: long-term results of a radiation dose escalation study,” Int. J. Radiat. Oncol., Biol., Phys. **63**, 324–333 (2005).

[2] M. Partridge, M. Ramos, A. Sardaro, and M. Brada, “Dose escalation for non-small cell lung cancer: analysis and modelling of published literature,” Radiother. Oncol. **99**, 6–11 (2011).

[3] American Cancer Society, Cancer Facts and Figures 2013, www.cancer.org (2013).

[4] J.-P. Bissonnette, T. G. Purdie, J. A. Higgins, W. Li, and A. Bezjak, “Cone-beam computed tomographic image guidance for lung cancer radiation therapy,” Int. J. Radiat. Oncol., Biol., Phys. **73**, 927–934 (2009).

[5] T. Juhler-Nøttrup *et al.*, “Interfractional changes in tumour volume and position during entire radiotherapy courses for lung cancer with respiratory gating and image guidance,” Acta Oncol. **47**, 1406–1413 (2008).

[6] L. Wang *et al.*, “The effect of radiation dose and chemotherapy on overall survival in 237 patients with stage III non-small-cell lung cancer,” Int. J. Radiat. Oncol., Biol., Phys. **73**, 1383–1390 (2009).

[7] A. R. Yeung, J. G. Li, W. Shi, H. E. Newlin, A. Chvetsov, C. Liu, J. R. Palta, and K. Olivier, “Tumor localization using cone-beam CT reduces setup margins in conventionally fractionated radiotherapy for lung tumors,” Int. J. Radiat. Oncol., Biol., Phys. **74**, 1100–1107 (2009).

[8] M. M. Knap, L. Hoffmann, M. Nordsmark, and A. Vestergaard, “Daily cone-beam computed tomography used to determine tumour shrinkage and localisation in lung cancer patients,” Acta Oncol. **49**, 1077–1084 (2010).

[9] E. S. Worm, A. T. Hansen, J. B. Petersen, L. P. Muren, L. H. Præstegaard, and M. Høyer, “Inter- and intrafractional localisation errors in cone-beam CT guided stereotactic radiation therapy of tumours in the liver and lung,” Acta Oncol. **49**, 1177–1183 (2010).

[10] H. Ikushima *et al.*, “Daily alignment results of in-room computed tomography-guided stereotactic body radiation therapy for lung cancer,” Int. J. Radiat. Oncol., Biol., Phys. **79**, 473–480 (2011).

[11]D. Verellen, M. D. Ridder, and G. Storme, “A (short) history of image-guided radiotherapy,” Radiother. Oncol. **86**, 4–13 (2008).

[12]D. Verellen, M. De Ridder, K. Tournel, M. Duchateau, T. Reynders, T. Gevaert, N. Linthout, and G. Storme, “An overview of volumetric imaging technologies and their quality assurance for IGRT,” Acta Oncol. **47**, 1271–1278 (2008).

[13]W. W. K. Fung and V. W. C. Wu, “Image-guided radiation therapy using computed tomography in radiotherapy,” J. Radiother. Pract. **10**, 121–136 (2011).

[14]C.-M. C. Ma and K. Paskalev, “In-room CT techniques for image-guided radiation therapy,” Med. Dosim. **31**, 30–39 (2006).

[15]T. R. Mackie *et al*., “Image guidance for precise conformal radiotherapy,” Int. J. Radiat. Oncol., Biol., Phys. **56**, 89–105 (2003).

[16]J. Pouliot *et al*., “Low-dose megavoltage cone-beam CT for radiation therapy,” Int. J. Radiat. Oncol., Biol., Phys. **61**, 552–560 (2005).

[17]O. Morin, A. Gillis, J. Chen, M. Aubin, M. K. Bucci, M. Roach III, and J. Pouliot, “Megavoltage cone-beam CT: system description and clinical applications,” Med. Dosim. **31**, 51–61 (2006).

[18]D. A. Jaffray, J. H. Siewerdsen, J. W. Wong, and A. A. Martinez, “Flat-panel cone-beam computed tomography for image-guided radiation therapy,” Int. J. Radiat. Oncol., Biol., Phys. **53**, 1337–1349 (2002).

[19]F.-F. Yin *et al*., “The Role of In-Room kV X-Ray Imaging for Patient Setup and Target Localization,” Med. Phys. (2009).

[20]J. J. W. Lagendijk *et al*., “MRI/Linac Integration,” Radiat. Oncol. **86**, 25–29 (2008).

[21]A. P. Galerani *et al*., “Dosimetric impact of online correction via cone-beam CT-based image guidance for stereotactic lung radiotherapy,” Int. J. Radiat. Oncol., Biol., Phys. **78**, 1571–1578 (2010).

[22]J. Higgins, A. Bezjak, K. Franks, L. W. Le, B. C. Cho, D. Payne, and J.-P. Bissonnette, “Comparison of spine, carina, and tumor as registration landmarks for volumetric image-guided lung radiotherapy,” Int. J. Radiat. Oncol., Biol., Phys. **73**, 1404–1413 (2009).

[23]J. A. Tanyi and M. H. Fuss, “Volumetric image-guidance: Does routine usage prompt adaptive re-planning? An institutional review,” Acta Oncol. **47**, 1444–1453 (2008).

[24]M. van Zwienen, S. van Beek, J. Belderbos, S. van Kranen, C. Rasch, M. van Herk, and J. Sonke, “Anatomical Changes during Radiotherapy of Lung Cancer Patients,” Int. J. Radiat. Oncol., Biol., Phys. **72**, S111 (2008).

[25]K. R. Britton *et al*., “Consequences of anatomic changes and respiratory motion on radiation dose distributions in conformal radiotherapy for locally advanced non-small-cell lung cancer,” Int. J. Radiat. Oncol., Biol., Phys. **73**, 94–102 (2009).

[26]J. P. Santoro, J. McNamara, E. Yorke, H. Pham, A. Rimner, K. E. Rosenzweig, and G. S. Mageras, “A study of respiration-correlated cone-beam CT scans to correct target positioning errors in radiotherapy of thoracic cancer,” Med. Phys. **39**, 5825–5834 (2012).

[27]G. R. Borst, J.-J. Sonke, A. Betgen, P. Remeijer, M. van Herk, and J. V. Lebesque, “Kilo-voltage cone-beam computed tomography setup measurements for lung cancer patients; First clinical results and comparison with electronic portal-imaging device,” Int. J. Radiat. Oncol., Biol., Phys. **68**, 555–561 (2007).

[28]N. Mohammed, L. Kestin, I. Grills, C. Shah, C. Glide-Hurst, D. Yan, and D. Ionascu, “Comparison of IGRT registration strategies for optimal coverage of primary lung tumors and involved nodes based on multiple four-dimensional CT scans obtained throughout the radiotherapy course,” Int. J. Radiat. Oncol., Biol., Phys. **82**, 1541–1548 (2012).

[29]M. L. Siker, W. A. Tomé, and M. P. Mehta, “Tumor volume changes on serial imaging with megavoltage CT for non-small-cell lung cancer during intensity-modulated radiotherapy: how reliable, consistent, and meaningful is the effect?” Int. J. Radiat. Oncol., Biol., Phys. **66**, 135–141 (2006).

[30]E. Weiss, S. P. Robertson, N. Mukhopadhyay, and G. D. Hugo, “Tumor, lymph node, and lymph node-to-tumor displacements over a radiotherapy series: Analysis of interfraction and intrafraction variations using active breathing control (ABC) in lung cancer,” Int. J. Radiat. Oncol., Biol., Phys. **82**, e639–e645 (2012).

[31]K. R. Britton *et al*., “Assessment of gross tumor volume regression and motion changes during radiotherapy for non-small-cell lung cancer as measured by four-dimensional computed tomography,” Int. J. Radiat. Oncol., Biol., Phys. **68**, 1036–1046 (2007).

[32]J. Fox, E. Ford, K. Redmond, J. Zhou, J. Wong, and D. Y. Song, “Quantification of tumor volume changes during radiotherapy for non-small-cell lung cancer,” Int. J. Radiat. Oncol., Biol., Phys. **74**, 341–348 (2009).

[33]G. Lim *et al*., “Tumor regression and positional changes in non-small cell lung cancer during radical radiotherapy,” J. Thorac. Oncol. **6**, 531–536 (2011).

[34]G. D. Hugo, E. Weiss, A. Badawi, and M. Orton, “Localization accuracy of the clinical target volume during image-guided radiotherapy of lung cancer,” Int. J. Radiat. Oncol., Biol., Phys. **81**, 560–567 (2011).

[35]F.-M. Kong, K. K. Wong, and T. Ritter, “Imaging during radiation therapy captures abrupt and dramatic changes,” J. Thorac. Oncol. **7**, 1736–1737 (2012).

[36]B. C. J. Cho, A. Bezjak, and L. A. Dawson, “Image guidance in non-small cell lung cancer,” Semin. Radiat. Oncol. **20**, 164–170 (2010).

[37] G. D. Hugo, C. Vargas, J. Liang, L. Kestin, J. W. Wong, and D. Yan, "Changes in the respiratory pattern during radiotherapy for cancer in the lung," Radiother. Oncol. **78**, 326–331 (2006).

[38] C. K. Glide-Hurst, E. Gopan, and G. D. Hugo, "Anatomic and pathologic variability during radiotherapy for a hybrid active breath-hold gating technique," Int. J. Radiat. Oncol., Biol., Phys. **77**, 910–917 (2010).

[39] J.-J. Sonke and J. Belderbos, "Adaptive radiotherapy for lung cancer," Semin. Radiat. Oncol. **20**, 94–106 (2010).

[40] M. Guckenberger, J. Meyer, J. Wilbert, K. Baier, G. Mueller, J. Wulf, and M. Flentje, "Cone-beam CT based image-guidance for extracranial stereotactic radiotherapy of intrapulmonary tumors," Acta Oncol. **45**, 897–906 (2006).

[41] T. G. Purdie, J.-P. Bissonnette, K. Franks, A. Bezjak, D. Payne, F. Sie, M. B. Sharpe, and D. A. Jaffray, "Cone-beam computed tomography for on-line image guidance of lung stereotactic radiotherapy: localization, verification, and intrafraction tumor position," Int. J. Radiat. Oncol., Biol., Phys. **68**, 243–252 (2007).

[42] J.-J. Sonke, J. Lebesque, and M. van Herk, "Variability of four-dimensional computed tomography patient models," Int. J. Radiat. Oncol., Biol., Phys. **70**, 590–598 (2008).

[43] I. S. Grills, G. D. Hugo, L. L. Kestin, A. P. Galerani, K. K. Chao, J. Wloch, and D. Yan, "Image-guided radiotherapy via daily online cone-beam CT substantially reduces margin requirements for stereotactic lung radiotherapy," Int. J. Radiat. Oncol., Biol., Phys. **70**, 1045–1056 (2008).

[44] M. Josipovic, G. F. Persson, Á. Logadottir, B. Smulders, G. Westmann, and J. P. Bangsgaard, "Translational and rotational intra- and inter-fractional errors in patient and target position during a short course of frameless stereotactic body radiotherapy," Acta Oncol. **51**, 610–617 (2012).

[45] S. P. Robertson, E. Weiss, and G. D. Hugo, "Localization accuracy from automatic and semi-automatic rigid registration of locally-advanced lung cancer targets during image-guided radiation therapy," Med. Phys. **39**, 330–341 (2011).

[46] K. K. Brock, M. Hawkins, C. Eccles, J. L. Moseley, D. J. Moseley, D. A. Jaffray, and L. A. Dawson, "Improving image-guided target localization through deformable registration," Acta Oncol. **47**, 1279–1285 (2008).

[47] M. Guckenberger, K. Baier, A. Richter, J. Wilbert, and M. Flentje, "Evolution of surface-based deformable image registration for adaptive radiotherapy of non-small cell lung cancer (NSCLC)," Radiat. Oncol. **4**, 68 (2009).

[48] G. Pratx and L. Xing, "GPU computing in medical physics: A review," Med. Phys. **38**, 2685 (2011).

[49] R. Shams, P. Sadeghi, R. Kennedy, and R. Hartley, "A Survey of Medical Image Registration on Multicore and the GPU," IEEE Signal Process. Mag. **27**, 50–60 (2010).

[50] M. Sharpe and K. K. Brock, "Quality assurance of serial 3D image registration, fusion, and segmentation," Int. J. Radiat. Oncol., Biol., Phys. **71**, S33–S37 (2008).

[51] E. Suárez-Santana, R. Nebot, C.-F. Westin, and J. Ruiz-Alzola, "Fast block matching registration with entropy-based similarity," Insight J. (2007).

[52] M. Söhn, M. Birkner, Y. Chi, J. Wang, D. Yan, B. Berger, and M. Alber, "Model-independent, multimodality deformable image registration by local matching of anatomical features and minimization of elastic energy," Med. Phys. **35**, 866–878 (2008).

[53] P. Rösch, T. Mohs, T. Netsch, M. Quist, G. P. Penney, D. J. Hawkes, and J. Weese, "Template selection and rejection for robust nonrigid 3D registration in the presence of large deformations," in *Medical Imaging 2001: Image Processing*, 545–556 (2001).

[54] Y. Liu, A. Kot, F. Drakopoulos, A. Enquobahrie, O. Clatz, and N. Chrisochoides, "An ITK implementation of physics-based non-rigid registration method," Insight J. (2012).

[55] O. Clatz, H. Delingette, I.-F. Talos, A. J. Golby, R. Kikinis, F. A. Jolesz, N. Ayache, and S. K. Warfield, "Robust nonrigid registration to capture brain shift from intraoperative MRI," IEEE Transactions on Medical Imaging **24**, 1417–1427 (2005).

[56] S. Ourselin, A. Roche, S. Prima, and N. Ayache, "Block matching: A general framework to improve robustness of rigid registration of medical images," in *Proceedings of MICCAI*, 557–566 (2000).

[57] S. Ourselin, R. Stefanescu, and X. Pennec, "Robust registration of multi-modal images: Towards real-time clinical applications," in *Proceedings of MICCAI*, 140–147 (2002).

[58] E. Chan and S. Panchanathan, "Review of block matching based motion estimation algorithms for video compression," in *Canadian Conference on Electrical and Computer Engineering, 1993*, 151–154 (1993).

[59] P. Rösch, T. Netsch, M. Quist, G. P. Penney, D. L. G. Hill, and J. Weese, "Robust 3D deformation field estimation by template propagation," in *Proceedings of MICCAI*, 521–530 (2000).

[60] P. Rösch, T. Netsch, M. Quist, and J. Weese, "3D respiratory motion compensation by template propagation," in *Proceedings of MICCAI*, 639–646 (2002).

[61] M. Bhattacharjee, A. Pitiot, A. Roche, D. Dormont, and E. Bardinet, "Anatomy-preserving nonlinear registration of deep brain ROIs using confidence-based block-matching," in *Proceedings of MICCAI*, 956–963 (2008).

[62] M. Modat, J. McClelland, and S. Ourselin, "Lung registration using the NiftyReg package," in *Medical Image Analysis for the Clinic: A Grand Challenge*, 33–42 (2010).

[63] M. Birkner, D. Thorwarth, A. Poser, F. Ammazzalorso, and M. Alber, "Analysis of the rigid and deformable component of setup inaccuracies on portal images in head and neck radiotherapy," Phys. Med. Biol. **52**, 5721–5733 (2007).

[64] S. van Kranen, S. van Beek, C. Rasch, M. van Herk, and J.-J. Sonke, "Setup uncertainties of anatomical sub-regions in head-and-neck cancer patients after offline CBCT guidance," Int. J. Radiat. Oncol., Biol., Phys. **73**, 1566–1573 (2009).

[65] S. van Kranen, S. van Beek, A. Mencarelli, C. Rasch, M. van Herk, and J.-J. Sonke, "Correction strategies to manage deformations in head-and-neck radiotherapy," Radiother. Oncol. **94**, 199–205 (2010).

[66] S. van Beek, S. van Kranen, A. Mencarelli, P. Remeijer, C. Rasch, M. van Herk, and J.-J. Sonke, "First clinical experience with a multiple region of interest registration and correction method in radiotherapy of head-and-neck cancer patients," Radiother. Oncol. **94**, 213–217 (2010).

[67] S. P. Robertson, E. Weiss, A. Badawi, and G. D. Hugo, "Improving localization of lung cancer targets for radiotherapy using semi-deformable featurelet registration," Med. Phys. **38**, 3845 (2011).

[68] G. D. Hugo, E. Al Sulaimani, E. Weiss, and S. P. Robertson, "Evaluation of the carina as a surrogate for daily localization of mediastinal lymph nodes during radiation therapy of locally-advanced lung cancer," Pract. Radiat. Oncol. (submitted).

[69] A. Wang, B. Disher, J. Battista, and T. Peters, "Use of a graphics processor (GPU) for high-performance deformable registration of cone beam (kV) and megavoltage (MV) CT images," Med. Phys. **37**, 3909 (2010).

[70] D. L. G. Hill, P. G. Batchelor, M. Holden, and D. J. Hawkes, "Medical image registration," Phys. Med. Biol. **46**, R1–R45 (2001).

[71] M. Unser, A. Aldroubi, and M. Eden, "B-spline signal processing. I. Theory," IEEE Transactions on Signal Processing **41**, 821–833 (1993).

[72] P. H. C. Eilers and B. D. Marx, "Flexible Smoothing with B-splines and Penalties," Statistical Science **11**, 89–102 (1996).

[73] T. Heimann *et al*., "Comparison and evaluation of methods for liver segmentation from CT datasets," IEEE Trans. Med. Imaging **28**, 1251–1265 (2009).

[74] P. J. Besl and H. D. McKay, "A method for registration of 3-D shapes," IEEE Trans. Pattern Anal. Mach. Intell. **14**, 239–256 (1992).

[75] D. W. Marquardt, "An Algorithm for Least-Squares Estimation of Nonlinear Parameters," SIAM J. Appl. Math **11**, 431–441 (1963).

[76]M. G. Jameson, L. C. Holloway, P. J. Vial, S. K. Vinod, and P. E. Metcalfe, “A review of methods of analysis in contouring studies for radiation oncology,” J. Med. Imaging Radiat. Oncol. **54**, 401–410 (2010).

[77]Y. H. Lau, M. Braun, and B. F. Hutton, “Non-rigid image registration using a median-filtered coarse-to-fine displacement field and a symmetric correlation ratio,” Phys. Med. Biol. **46**, 1297–1319 (2001).

[78]A. Roche, G. Malandain, X. Pennec, and N. Ayache, “The correlation ratio as a new similarity measure for multimodal image registration,” in *Proceedings of MICCAI*, 1115–1124 (1998).

[79]E. Weiss *et al.*, “Clinical evaluation of soft tissue organ boundary visualization on cone-beam computed tomographic imaging,” Int. J. Radiat. Oncol., Biol., Phys. **78**, 929–936 (2010).

[80]C. Woodford, S. Yartsev, A. R. Dar, G. Bauman, and J. Van Dyk, “Adaptive radiotherapy planning on decreasing gross tumor volumes as seen on megavoltage computed tomography images,” Int. J. Radiat. Oncol., Biol., Phys. **69**, 1316–1322 (2007).

APPENDIX I

LOCALIZATION ACCURACY FROM AUTOMATIC AND SEMI-AUTOMATIC RIGID REGISTRATION OF LOCALLY-ADVANCED LUNG CANCER TARGETS DURING IMAGE-GUIDED RADIATION THERAPY

Localization accuracy from automatic and semi-automatic rigid registration of locally-advanced lung cancer targets during image-guided radiation therapy

Scott P. Robertson, Elisabeth Weiss, and Geoffrey D. Hugo[a)]
Department of Radiation Oncology, Virginia Commonwealth University, Richmond, Virginia 23298

(Received 19 July 2011; revised 29 November 2011; accepted for publication 1 December 2011; published 21 December 2011)

Purpose: To evaluate localization accuracy resulting from rigid registration of locally-advanced lung cancer targets using fully automatic and semi-automatic protocols for image-guided radiation therapy.
Methods: Seventeen lung cancer patients, fourteen also presenting with involved lymph nodes, received computed tomography (CT) scans once per week throughout treatment under active breathing control. A physician contoured both lung and lymph node targets for all weekly scans. Various automatic and semi-automatic rigid registration techniques were then performed for both individual and simultaneous alignments of the primary gross tumor volume (GTV_P) and involved lymph nodes (GTV_{LN}) to simulate the localization process in image-guided radiation therapy. Techniques included "standard" (direct registration of weekly images to a planning CT), "seeded" (manual prealignment of targets to guide standard registration), "transitive-based" (alignment of pretreatment and planning CTs through one or more intermediate images), and "rereferenced" (designation of a new reference image for registration). Localization error (LE) was assessed as the residual centroid and border distances between targets from planning and weekly CTs after registration.
Results: Initial bony alignment resulted in centroid LE of 7.3 ± 5.4 mm and 5.4 ± 3.4 mm for the GTV_P and GTV_{LN}, respectively. Compared to bony alignment, transitive-based and seeded registrations significantly reduced GTV_P centroid LE to 4.7 ± 3.7 mm ($p = 0.011$) and 4.3 ± 2.5 mm ($p < 1 \times 10^{-3}$), respectively, but the smallest GTV_P LE of 2.4 ± 2.1 mm was provided by rereferenced registration ($p < 1 \times 10^{-6}$). Standard registration significantly reduced GTV_{LN} centroid LE to 3.2 ± 2.5 mm ($p < 1 \times 10^{-3}$) compared to bony alignment, with little additional gain offered by the other registration techniques. For simultaneous target alignment, centroid LE as low as 3.9 ± 2.7 mm and 3.8 ± 2.3 mm were achieved for the GTV_P and GTV_{LN}, respectively, using rereferenced registration.
Conclusions: Target shape, volume, and configuration changes during radiation therapy limited the accuracy of standard rigid registration for image-guided localization in locally-advanced lung cancer. Significant error reductions were possible using other rigid registration techniques, with LE approaching the lower limit imposed by interfraction target variability throughout treatment. [DOI: 10.1118/1.3671929]

Key words: non-small cell lung cancer, lymph nodes, image registration, image-guided radiation therapy

I. INTRODUCTION

One of the major limitations in lung cancer radiotherapy involves the localization of targets before and during a treatment fraction.[1] Geometric uncertainties inherent in the preparation and execution of each fraction are typically mitigated by the use of treatment margins to ensure that target coverage is maintained to within a clinically acceptable probability.[2] Improving target localization will therefore decrease the size of treatment margins and spare an increased volume of healthy tissue from irradiation.[3] This increases the potential for dose escalation,[4] which has been shown in numerous studies to increase local tumor control and ultimately lead to better patient outcomes.[5,6]

Image-guided radiotherapy has become a widespread clinical tool[7] with numerous applications to the treatment process,[8] one of which includes patient setup. Three-dimensional and even four-dimensional pretreatment imaging techniques facilitate substantially better target localization than traditional guidance practices, such as the use of in-room lasers or planar portal imaging.[9,10] With these older methods, patient setup was generally accomplished by aligning external surrogates or bony-anatomy.[11] However, the correlation between these features and lung cancer targets may be poor.[12–14] Pretreatment volumetric imaging provides superior visualization of internal anatomy and makes possible the use of soft-tissue surrogates,[15–17] although these features may also fail to correlate with the position and motion of lung cancer targets.[5,18]

In theory, direct registration of targets should provide optimal localization,[19] but this strategy presents difficulties as well. Significant pathological changes are possible throughout treatment, including lung tumor regression[20–24] and changes in metastatic nodal volume.[10,25] In addition, pathology of the ipsilateral lung such as pleural effusion and atelectasis (which we term "pathology-induced changes") can alter the local environment surrounding lung cancer targets.[4] Finally, the configuration between primary tumors and lymph nodes may change over time due to intertarget variability.[18,25,26] These effects complicate manual target alignment and the use of rigid registration algorithms.[24,26] Deformable registration may be better suited to address moderate pathological and pathology-induced changes, but substantial variation throughout treatment may lead to misregistration.[27] Furthermore, validation of deformable algorithms is not yet available for the setup of lung cancer patients, and relatively long computation times have inhibited clinical implementation to date for patient setup.[28] As a result of the limitations of deformable registration, and because rigid registration is the current clinical standard for image-guided radiation therapy, we set out to assess the performance and limitations of rigid registration algorithms for the setup of lung cancer patients. The purpose of this study was to evaluate localization error resulting from automatic rigid registration applied directly to the alignment of primary lung tumors and involved lymph nodes. The secondary purpose was to develop and evaluate practical adaptations of this rigid registration protocol to reduce the residual localization error.

II. METHODS

II.A. Patient population

Seventeen patients with stage IIA to IV locally-advanced non-small cell lung cancer received weekly computed tomography (CT) scans under active breathing control according to a protocol approved by the local institutional review board. Details of the imaging protocol were described by Glide-Hurst *et al.*[29] Briefly, all patients completed an initial coaching session on the Active Breathing Coordinator (version 2.0, Elekta, Stockholm, Sweden). Breath-holds were conducted at 80% of the end-of-normal inspiration lung volume for 8–15 s. Patient characteristics are summarized in Table I.

II.B. Image acquisition

Weekly CT images were acquired without contrast using a 16-slice helical CT scanner (Brilliance Big Bore, Philips Medical Systems, Andover, MA). Four to seven imaging sessions were completed for each patient throughout treatment, for a total of 99 images. The week 1 planning CT was designated as the reference image, R, and all other weekly CTs were designated as secondary images, S_n, for registration. To eliminate patient setup uncertainties, each secondary image was manually translated and rotated to match the bony-anatomy of the reference CT [Figs. 1(a) and 1(b)] in a research version of the PINNACLE[3] treatment planning system (version 8.1y, Philips Medical Systems, Fitchburg, WI). The gross tumor volume (GTV) was contoured by a physician for all lung cancer targets, including primary tumors ($\mathrm{GTV_P}$) and metastatic lymph nodes ($\mathrm{GTV_{LN}}$). For patients with multiple targets of each type, the final $\mathrm{GTV_P}$ and $\mathrm{GTV_{LN}}$ were defined as the union of all contoured primary tumors and involved lymph nodes, respectively. Bony alignment error was defined as the centroid and border displacements between corresponding targets from R and S_n in this initial alignment.

TABLE I. Population characteristics.

Description	Treatment target: Primary tumor	Treatment target: Lymph nodes
Total number of patients	17	14
With pathology-induced changes		
Atelectasis	5	5
Pleural effusion	2	2
Number of patients with:		
1 Contoured target	16	9
2 Contoured targets	1	4
3 Contoured targets	0	1
Number of imaging sessions	4–7	4–7
Total number of CT scans	99	83
Number of registrations	82	69
Target volume:		
Average ± St dev (cm^3)	67.8 ± 83.0	5.7 ± 7.2
Range (cm^3)	0.4–377.4	0.2–27.0
Change per week[a]	−7.6% ($R^2 = 0.28$, $p < 1 \times 10^{-6}$)	−6.5% ($R^2 = 0.17$, $p < 1 \times 10^{-3}$)

[a] As determined from linear regression between normalized tumor volume (relative to week 1 for each patient) and treatment week.

II.C. Individual target registration

Table II lists the registration strategies evaluated in this study. We first explored "standard" registration of all secondary images to the planning CT in the PINNACLE[3] treatment planning system. Automatic, intensity-based rigid registrations were used to directly align the treatment targets from each S_n to R [Figs. 1(c) and 1(d)]. The registration volume on R was limited to either the $\mathrm{GTV_P}$ or $\mathrm{GTV_{LN}}$ plus a uniform 1 cm margin, which was found in initial tests to provide the best target localization compared to other margin sizes. No volume limits were applied to S_n to avoid potentially cropping the secondary target, which was assumed to be uncontoured and unknown *a priori* on weekly images. Only translational degrees of freedom were performed to simulate shifts in the treatment couch. Separate registrations were performed for the $\mathrm{GTV_P}$ and $\mathrm{GTV_{LN}}$ using each of the available algorithms in PINNACLE:[3] local correlation, cross correlation, and normalized mutual information (NMI). Localization error (LE) was computed as the residual displacement between manually-delineated targets from R and S_n after automatic registration. To address instances of large residual LE from standard registration, a "seeded" registration strategy was also explored in which secondary images were

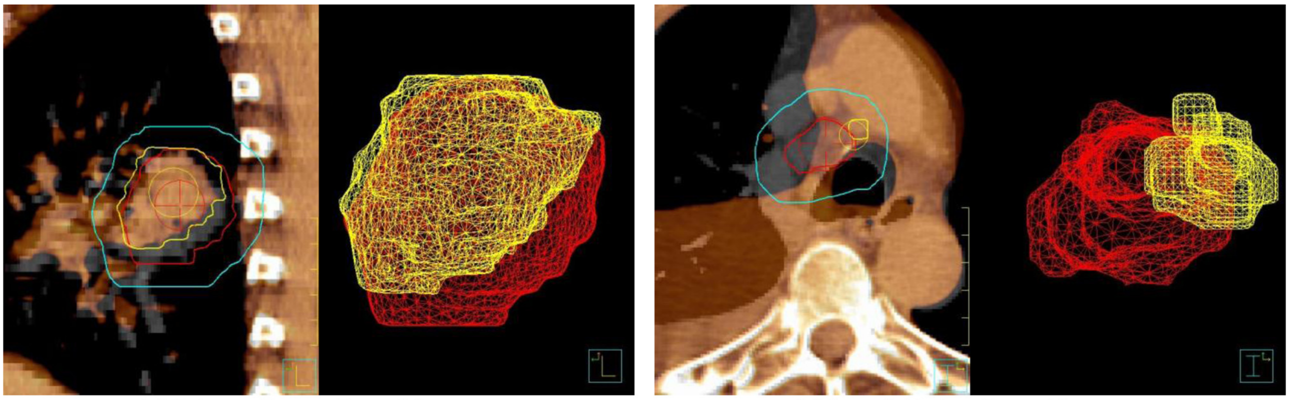

(a) Primary Tumor: Bony Alignment

(b) Lymph Nodes: Bony Alignment

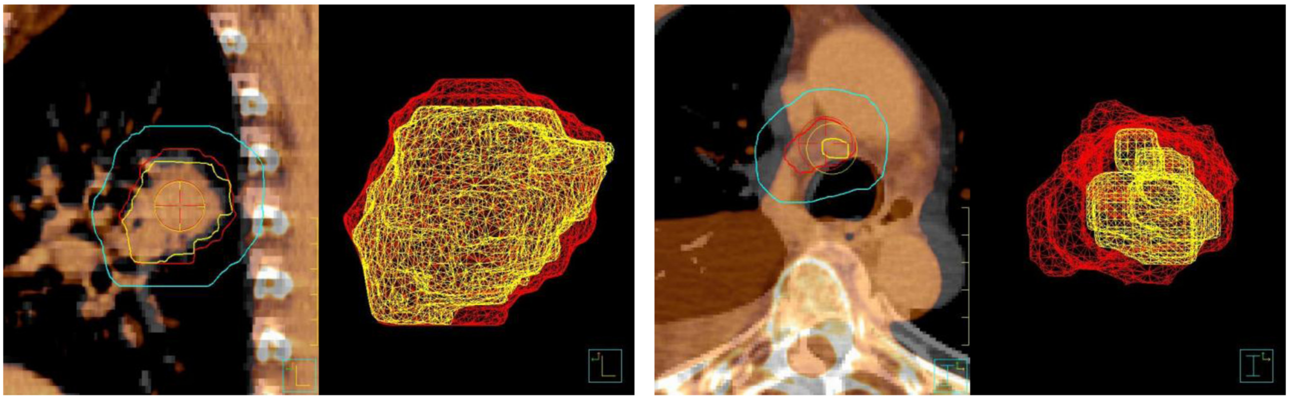

(c) Primary Tumor: Automatic Registration

(d) Lymph Nodes: Automatic Registration

FIG. 1. Overlay image showing the registration of targets from reference and secondary CTs from two different patients. Images were initially aligned using bony-anatomy (a)–(b). Pleural effusion likely contributed to the initial misalignment of an involved lymph node in (b). Automatic, rigid registration improved the localization of both the primary tumor (c) and involved lymph nodes (d) for patients in this study. The smaller surface meshes (foreground) represent targets from weekly CT images, whereas the larger surface meshes (background) represent targets from the initial planning CT. An additional contour is provided to demonstrate the registration volume obtained by a 10 mm isotropic expansion of targets from the planning CT.

brought into better initial alignment to guide standard registration. Specifically, secondary images were manually translated to align the centroids of planning and weekly target volumes to reduce the impact of large initial displacements on the accuracy of automatic registration. Because seeded registration required a manual pre-alignment of targets, it was considered a semi-automatic localization strategy.

Further reductions in target LE were sought by mitigating the gradual but sometimes substantial deformations observed throughout treatment, including both pathological and pathology-induced changes. This was accomplished using a "transitive-based" (TB) registration technique similar to that explored by Škrinjar *et al.*[30] Briefly, any two images in a sequence (e.g., R and S_n) can be registered by matching each to an arbitrary intermediate image, S_m, where $1 < m < n$ for the present study. According to the transitivity property,[30] the registration between S_n and R should be equal to the composition of intermediate registrations

$$\mathbf{T}(S_n \rightarrow R) = \mathbf{T}(S_m \rightarrow R) \circ \mathbf{T}(S_n \rightarrow S_m), \quad (1)$$

where $\mathbf{T}(A \rightarrow B)$ is the transformation resulting from registration of image A to image B, and $\circ$ denotes the composition of two separate registrations. In general, CT scans acquired with fewer fractions between them demonstrated less substantial deformation of internal anatomy. Transitive-based registrations were therefore expected to achieve lower LE than standard registrations as long as the composition of intermediate steps did not propagate target LE substantially.

Two subtypes of TB registration were explored, termed "intermediate" and "consecutive." Intermediate-TB registration involved the alignment of all weekly images acquired during or after the fourth week of treatment to the week 3 CT, S_3. This result, in turn, was composed with the registration between S_3 and R, or

$$\mathbf{T}^{TB}_{\text{intermed}}(S_n \rightarrow R) = \begin{cases} \mathbf{T}(S_3 \rightarrow R) \circ \mathbf{T}(S_n \rightarrow S_3) & 3 < n \\ \mathbf{T}(S_n \rightarrow R) & 1 < n \leq 3 \end{cases}. \quad (2)$$

The week 3 CT was designated as the sole intermediate image for several reasons. Underberg *et al.* showed that significant target volume regression was possible by the fourth week of treatment.[31] Similarly, Woodford *et al.* observed that adaptive planning is most beneficial for targets regressing by at least 30% within the first 20 fractions.[32] Although adaptive planning was not considered in this study, the week 3 CT was still hypothesized to provide reasonable localization accuracy between targets from intermediate and reference images, while enabling reasonable registration of all subsequent weekly images that may be subject to these large

TABLE II. Summary of nine registration techniques explored in this study. The nominal techniques provide a lower bound on LE for each metric. As such, it is unnecessary to compute border LE for centroid alignment and centroid LE for border alignment. Therefore, only eight registration techniques are presented for each LE metric in the remaining tables and in Figs. 3–6. NMI: normalized mutual information.

Registration	Short name	Description	Implementation
Bony-anatomy	Bony	Manual alignment of the spine, sternum, and ribs using translations and rotations. All other registrations use translational degrees of freedom only	Manual
Standard NMI	Standard	Direct, automatic registration of lung cancer targets, including the primary tumor and/or involved lymph nodes, between on-treatment and planning images	Automatic
Seeded NMI	Seeded	Quick, approximate manual prealignment of targets, followed by standard registration	Semi-automatic
Intermediate transitive-based	Intermediate-TB	Alignment of on-treatment and planning images by composing the separate registrations of each to a single intermediate image [Eq. (2)]	Automatic
Consecutive transitive-based	Consecutive-TB	Alignment of on-treatment and planning images by composing the separate registrations between all consecutive weekly images [Eq. (3)]	Automatic
Intermediate rereferenced	Intermediate-RR	Designation of a single, intermediate weekly CT as the new reference for registration of all subsequent treatment fractions, given that the relative orientation is known between the new reference and planning images [Eq. (4)]	Semi-automatic
Consecutive rereferenced	Consecutive-RR	Designation of the previous weekly CT as the new reference for registration of the current on-treatment image, given that the relative orientation is known between the new reference and planning images [Eq. (5)]	Semi-automatic
Nominal centroid alignment	Centroid	Registration to minimize centroid localization errors for all targets simultaneously	Computed from target contours
Nominal border alignment	Border	Registration to minimize the distance between reference and secondary target borders in the left–right, anterior–posterior, and superior–inferior directions, computed directly from the manual contours	Computed from target contours

volume deformations. In the consecutive-TB strategy, each weekly CT was registered to the on-treatment image from the previous week. The relative orientation between secondary and reference images was then computed as the composition of all consecutive registrations, or

$$\mathbf{T}^{TB}_{\text{sequential}}(S_n \rightarrow R) = \mathbf{T}(S_2 \rightarrow R) \circ \mathbf{T}(S_3 \rightarrow S_2) \circ \ldots \circ \mathbf{T}(S_n \rightarrow S_{n-1}). \quad (3)$$

Each individual registration in this series exploited the greatest similarity of internal anatomy by matching sequential weekly CTs. However, the propagation of residual LE from each consecutive registration could also result in unacceptable target localization if not carefully controlled at each step. Both intermediate-TB and consecutive-TB registrations were considered fully automatic, as the composition of multiple registrations should not require manual interaction.

The final localization technique, termed "rereferenced" (RR) registration, was similar to the transitive-based strategy. Weekly images were still registered to an intermediate CT, but the intermediate CT was established as a new reference image for registration, requiring the relative orientation between new and original reference images to be determined (e.g., through offline review prior to the current treatment fraction). Specifically, this was accomplished by performing a nominal centroid alignment between contoured targets from the new and original reference images. Because this transform was known, it did not contribute to the propagation of residual target LE. As with TB registration, two subtypes of RR registration were explored. Intermediate-RR registration involved the registration of all weekly CTs acquired during or after the fourth week of treatment directly to the week 3 CT, given that the transformation between the week 3 CT and the reference image was known,

$$\mathbf{T}^{RR}_{\text{intermed}}(S_n \rightarrow R) = \begin{cases} \mathbf{T}_{\text{known}}(S_3 \rightarrow R) \circ \mathbf{T}(S_n \rightarrow S_3) & 3 < n \\ \mathbf{T}(S_n \rightarrow R) & 1 < n \leq 3 \end{cases}. \quad (4)$$

Consecutive-RR registration required that each weekly CT was registered directly to the on-treatment image from the previous week, given that the transformation between the previous weekly CT and the reference image was known,

$$\mathbf{T}^{RR}_{\text{sequential}}(S_n \rightarrow R) = \mathbf{T}_{\text{known}}(S_{n-1} \rightarrow R) \circ \mathbf{T}(S_n \rightarrow S_{n-1}). \quad (5)$$

In both cases, we assumed that manual interaction was necessary to determine the known transformations, resulting in semi-automatic registration techniques.

II.D. Simultaneous target registration

Because lung cancer targets are not typically treated as separate structures in planning, a single transformation was sought that simultaneously optimized the alignment of both the primary tumor and lymph nodes for treatment. Only, the fourteen patients presenting with both primary and lymph node GTVs were considered for this analysis. Two strategies were tested for localizing these two volumes concurrently. In the first method, termed "collective" registration, the GTV_P and GTV_LN were combined into a single structure for registration, but with LE determined for each target separately. The second method, referred to as "averaged" registration, involved separate registrations of the GTV_P and

GTV_{LN}, with a final transformation computed as the unweighted average of the two individual alignments. All registration strategies for individual target localization were also implemented for both collective and averaged simultaneous target alignment.

II.E. Data analysis

Evaluation of registration accuracy was based on target centroid and border LE. Centroid LE was defined as the displacement in the center-of-volume of secondary targets from that of the corresponding reference target. Because centroid LE may not be fully sufficient to characterize localization accuracy in cases of large target deformation and volume change,[29] target border LE was considered as an alternative metric. Border LE was defined as the shift of a secondary target border radially outward from the corresponding border of a reference structure in each of the cardinal directions: left–right (LR), anterior–posterior (AP), and superior–inferior (SI). A radially inward shift implied that the border of the secondary target was contained within the reference structure, resulting in an increased probability of adequate target coverage along that border. Therefore, only outward shifts were considered in this analysis, similar to the method used previously by Hugo *et al.*[33] A threshold of 2 mm for border LE was selected as a reasonable clinical action level, below which corrections would not be performed.[33] Because the number of targets with border LE varied among registration strategies, the mean border LE provided an inconsistent comparison. Instead, we compared the fraction of targets with border LE, defined as the percentage of all target borders with errors greater than the given threshold. For example, a value of 1 implied that all borders had LE greater than 2 mm, whereas a value of 0 indicated that no borders had LE exceeding 2 mm.

Using these error metrics, nominal registrations were determined to provide optimal target localization from the manually-delineated structures, as follows. First, nominal centroid alignments were computed as the transformation minimizing the displacement of target centroids, considering only translational degrees of freedom. The nominal centroid alignment for an individual target volume was given by perfectly overlapped centroids (i.e., LE of 0 mm) and was not considered for statistical analysis. For simultaneous target registration, all centroid displacements were minimized concurrently, yielding a nonzero error magnitude. Nominal border alignments were also performed to minimize the distance between reference and secondary target borders in the cardinal directions (i.e., along the LR, AP, and SI axes), again considering only translational degrees of freedom. Potentially nonzero border LE was possible for both individual and simultaneous nominal border alignment. Note that optimal centroid and border LE were determined from separate registrations. Also, because these nominal, contour-based registrations served only to determine the lower bound of each respective LE metric, it was not necessary to compute border LE for centroid alignment or centroid LE for border alignment.

To test for significant differences between various registration techniques, a one-way, repeated measures analysis of variance known as the Friedman test was performed for centroid LE. Because the centroid LE was non-normally distributed, this nonparametric test was chosen to perform analysis of variance using the ranks of centroid LE data across all registration techniques, providing a more conservative analysis than the corresponding parametric test. Intercomparisons between registration techniques were made using the Tukey range test. For individual target registration, this analysis was applied separately for GTV_P and GTV_{LN} centroid LE (Fig. 3), whereas for simultaneous target registration, a single analysis was applied over the centroid LE from both targets collectively (Fig. 5).

Studies have shown that target volume regression can compromise target shape and position reproducibility.[4,29,34] Linear regression was used to determine correlation of LE magnitude with regressing target volumes throughout treatment. Registrations were considered more robust against volume regression as the R^2 value decreased. In addition to these effects, pathology-induced changes, including atelectasis and pleural effusion, may affect tissue contrast adjacent to targets and impact the accuracy of rigid registration. In this study, five patients demonstrated atelectasis and two patients demonstrated pleural effusion, all of which either fully or partially resolved or progressed during treatment. To determine the significance of these effects, we compared the centroid LE for patients with and without pathology-induced changes using a Wilcoxon rank sum test. This nonparametric analysis was chosen to address the non-normal distribution of centroid LE. If patients with pathology-induced changes did not demonstrate centroid LE significantly greater than patients without such changes, then registrations were considered robust against this influence.

III. RESULTS

III.A. Individual target registration

Manual alignment of bony-anatomy resulted in initial centroid LE of 7.3 ± 5.4 mm for the GTV_P and 5.3 ± 3.4 mm for the GTV_{LN}. As shown in Fig. 2(a), bony alignment error demonstrated moderate correlation with the normalized primary tumor volume throughout treatment ($R^2 = 0.396$). This relationship was less evident for lymph nodes [Fig. 2(b), $R^2 = 0.197$]. In this initial alignment, patients with pathology-induced changes had mean GTV_P LE of 9.2 ± 6.9 mm, compared to 6.0 ± 3.7 mm for patients without these changes ($p = 0.10$). GTV_{LN} LE were 7.3 ± 3.6 mm and 3.5 ± 1.7 mm for patients with and without these changes, respectively ($p < 0.001$).

Automatic registration using the cross correlation algorithm increased centroid LE to 10.0 ± 8.5 mm and 6.9 ± 4.4 mm for the GTV_P and GTV_{LN}, respectively. Local correlation slightly reduced corresponding LE to 6.5 ± 5.5 mm and 4.8 ± 4.1 mm, but the NMI cost function provided the lowest absolute mean LE of 5.8 ± 6.0 mm and 3.2 ± 2.5 mm. NMI registration also reduced the correlation of centroid LE with normalized target volume throughout treatment (GTV_P, $R^2 = 0.203$;

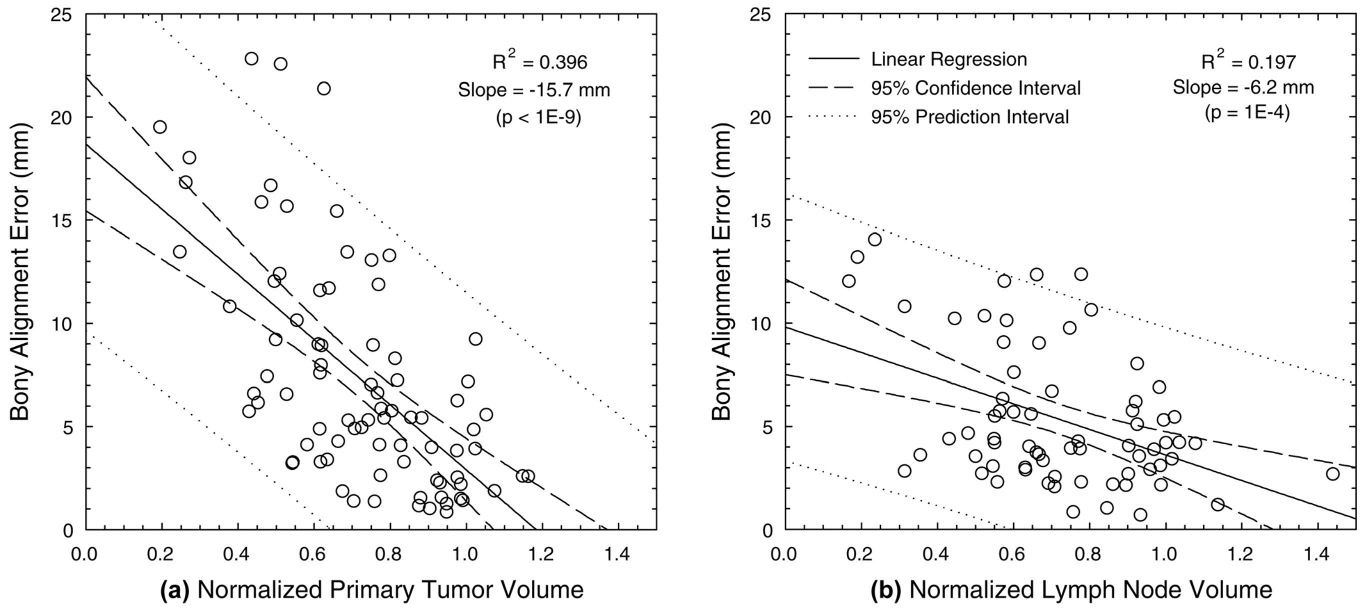

FIG. 2. Magnitude of centroid LE after manual bony-anatomy registration, plotted against the normalized target volume relative to the beginning of treatment for (a) the primary tumor and (b) involved lymph nodes.

GTV_{LN}, $R^2 = 0.080$). Patients with pathology-induced changes still demonstrated GTV_P LE approximately 1.5 times larger than patients without these changes ($p > 0.10$); however, the difference between GTV_{LN} LE was reduced to just 0.8 mm for these patient subgroups as a result of NMI registration ($p > 0.10$). Because NMI demonstrated the most potential to improve target localization, this similarity metric was used for all remaining studies.

Seeded NMI registration further improved centroid LE for both the GTV_P and GTV_{LN}, respectively (Table III and Fig. 3). The overall reduction in LE, however, stemmed from just a handful of registrations with substantially improved localization. Compared to standard NMI alignment, only 8 out of 82 seeded GTV_P registrations improved LE by more than 2 mm, but with an average improvement of 15.9 mm (range: 3.7–28.5 mm). Likewise, only 4 out of 69 seeded lymph node registrations improved LE, but with an average improvement of 7.1 mm (range: 2.8–10.5 mm). Large centroid LE persisted for remaining registrations, with 35% of GTV_P and 10% of GTV_{LN} registration errors still exceeding 5 mm. Despite these limitations, seeded registrations reduced the difference in centroid LE to just 0.5 mm between patient subgroups with and without pathology-induced changes ($p > 0.10$). The correlation between centroid LE and normalized target volume was also weak (GTV_P, $R^2 = 0.03$; GTV_{LN}, $R^2 = 0.11$).

Similar LE magnitudes were obtained from intermediate-TB and consecutive-TB registration techniques. Linear propagation of residual errors contributed to the magnitude of LE for these registrations. Rereferenced registrations demonstrated the lowest centroid LE for both targets in this study, although the improvements in target localization were much more pronounced for the GTV_P than the GTV_{LN}. As with seeded registrations, TB and RR registration strategies produced negligible differences in centroid LE between patient subgroups with and without pathology-induced changes for

TABLE III. Mean (standard deviation) of the magnitude of *centroid* LE for both individual target registration (GTV_P or GTV_{LN}) and simultaneous target registration (collective or averaged). “Collective” registration involved the simultaneous alignment of the GTV_P and GTV_{LN} using a single registration, whereas “averaged” registration consisted of separate alignments for each individual target volume, which were then averaged together to obtain the final transform.

		Primary tumor registration (mm)			Lymph node registration (mm)		
Registration	Short name	GTV_P	Collective	Averaged	GTV_{LN}	Collective	Averaged
Bony-anatomy	Bony	7.3 (5.4)	7.3 (5.7)	7.3 (5.7)	5.3 (3.4)	5.3 (3.4)	5.3 (3.4)
Standard NMI	Standard	5.8 (6.0)	6.7 (6.9)	5.7 (5.5)	3.2 (2.5)	4.9 (4.1)	4.0 (2.7)
Seeded NMI	Seeded	4.3 (2.5)	6.0 (6.1)	4.6 (3.1)	2.8 (1.8)	5.1 (4.4)	3.9 (2.3)
Intermediate transitive-based	Intermediate-TB	4.7 (3.7)	6.3 (7.2)	4.9 (4.2)	3.0 (2.0)	5.7 (5.0)	3.6 (2.1)
Consecutive transitive-based	Consecutive-TB	4.8 (3.7)	7.8 (12.3)	5.1 (3.8)	3.3 (1.7)	6.9 (10.7)	3.8 (2.2)
Intermediate rereferenced	Intermediate-RR	3.2 (3.0)	5.5 (5.8)	4.2 (3.3)	2.6 (2.2)	5.2 (4.3)	3.9 (2.5)
Consecutive rereferenced	Consecutive-RR	2.4 (2.1)	5.0 (5.2)	3.9 (2.7)	2.2 (1.4)	4.9 (3.7)	3.8 (2.3)
Nominal centroid alignment	Centroid	0.0 (0.0)	3.3 (2.3)	3.3 (2.3)	0.0 (0.0)	3.3 (2.3)	3.3 (2.3)

Note: GTV_P: primary gross tumor volume; GTV_{LN}: lymph node gross tumor volume; NMI: normalized mutual information algorithm.

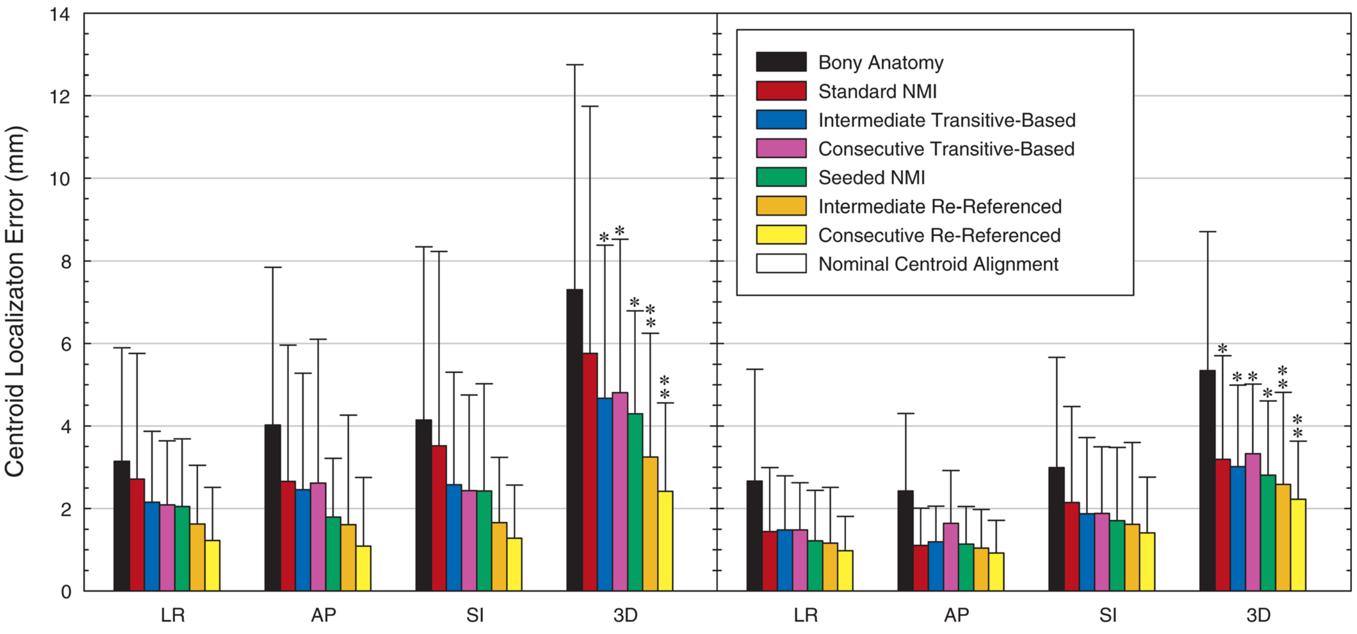

(a) Primary Tumor **(b)** Lymph Nodes

FIG. 3. Mean absolute centroid LE in the LR, AP, and SI directions and in three-dimensional (3D) magnitude after individual registration of (a) the primary tumor and (b) involved lymph nodes. Standard normalized mutual information (NMI) and transitive-based registrations were fully automatic, whereas seeded NMI and rereferenced registrations required varying degrees of manual interaction and were considered semi-automatic. Single asterisks denote significantly improved target localization relative to the initial bony-anatomy alignment, and double asterisks show additional significant improvement relative to other automatic registration techniques. Nominal centroid alignment of individual target volumes (GTV_P or GTV_{LN}) resulted in perfect centroid overlap, corresponding to zero centroid LE.

both the GTV_P ($p > 0.07$) and GTV_{LN} ($p > 0.10$). In addition, RR registrations were also robust against target volume regression, as the correlation between centroid LE and normalized target volume was largely eliminated (GTV_P, $R^2 \leq 0.07$; GTV_{LN}, $R^2 \leq 0.006$).

A Friedman test was used to compare initial bony alignment errors against centroid LE from individual target registration using the NMI algorithm (Table III). Significant LE reductions were observed for both the primary tumor ($p < 1 \times 10^{-9}$) and lymph nodes ($p < 1 \times 10^{-9}$). As shown in Fig. 3(a), all GTV_P registration techniques significantly improved primary tumor LE over bony alignment except for standard registration. In addition, rereferenced registrations demonstrated significant improvement over standard and transitive-based techniques. No significant difference was found between intermediate-RR and sequential-RR registrations. For the lymph nodes, all registration techniques provided significant improvement over bony alignment [Fig. 3(b)]. The consecutive-RR technique provided additional significant reductions over standard and transitive-based techniques but was not significantly better than seeded or intermediate-RR alignments.

Unlike centroid LE, the frequency of border LE greater than 2 mm, defined as the fraction of all target borders with LE greater than this threshold, demonstrated less substantial variation between different registration techniques (Table IV and Fig. 4). The frequency of GTV_P border LE decreased from 0.21 for bony alignment to between 0.12

TABLE IV. Fraction of all target borders demonstrating *border* LE greater than 2 mm for both individual target registration (GTV_P or GTV_{LN}) and simultaneous target registration (collective or averaged), as defined by the Table III caption.

		Primary tumor registration			Lymph node registration		
Registration	Short name	GTV_P	Collective	Averaged	GTV_{LN}	Collective	Averaged
Bony-anatomy	Bony	0.185	0.169	0.169	0.126	0.126	0.126
Standard NMI	Standard	0.152	0.169	0.133	0.082	0.140	0.106
Seeded NMI	Seeded	0.132	0.143	0.109	0.072	0.157	0.111
Intermediate transitive-based	Intermediate-TB	0.124	0.145	0.111	0.080	0.171	0.099
Consecutive transitive-based	Consecutive-TB	0.128	0.147	0.123	0.063	0.135	0.111
Intermediate rereferenced	Intermediate-RR	0.124	0.147	0.106	0.068	0.157	0.114
Consecutive rereferenced	Consecutive-RR	0.140	0.152	0.114	0.070	0.162	0.126
Nominal border alignment	Border	0.077	0.116	0.116	0.010	0.099	0.099

Note: GTV_P: primary gross tumor volume; GTV_{LN}: lymph node gross tumor volume; NMI: normalized mutual information algorithm.

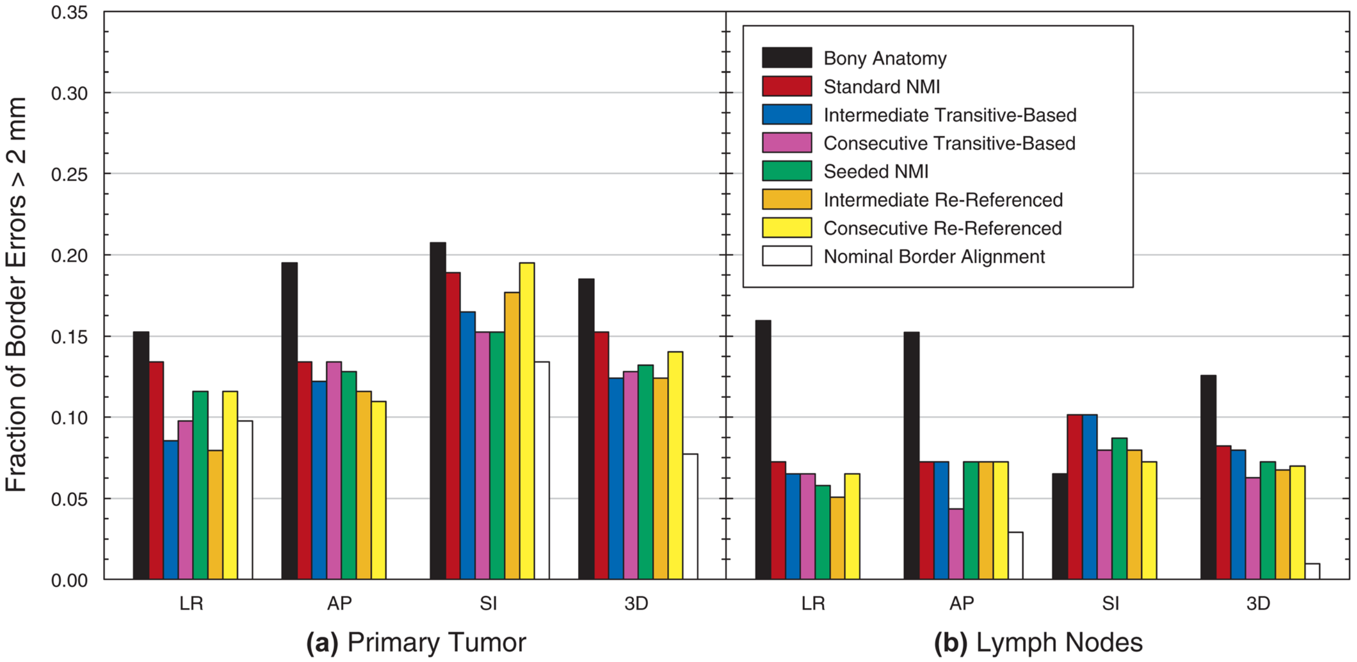

FIG. 4. Frequency of target border LE greater than 2 mm in the LR, AP, and SI directions and in all three dimensions (3D) after individual registration of (a) the primary tumor and (b) involved lymph nodes. Nominal border alignment was defined as the transformation that minimized localization errors for opposing target borders in each cardinal direction. In several cases, this provided localization of all borders in a given direction to within 2 mm, corresponding to a frequency of zero. NMI: normalized mutual information.

and 0.15 for the automatic and semi-automatic registration techniques. Nominal $\mathrm{GTV_P}$ border alignment indicated that border LE frequencies as low as 0.09 were possible. This nonzero frequency was attributed to target growth and shape change throughout treatment. For the $\mathrm{GTV_{LN}}$, the frequency of border LE was reduced from 0.17 for bony alignment to between 0.06 and 0.08 for automatic and semi-automatic registration. Nominal border alignment showed that a frequency of 0.01 was possible for the lymph nodes.

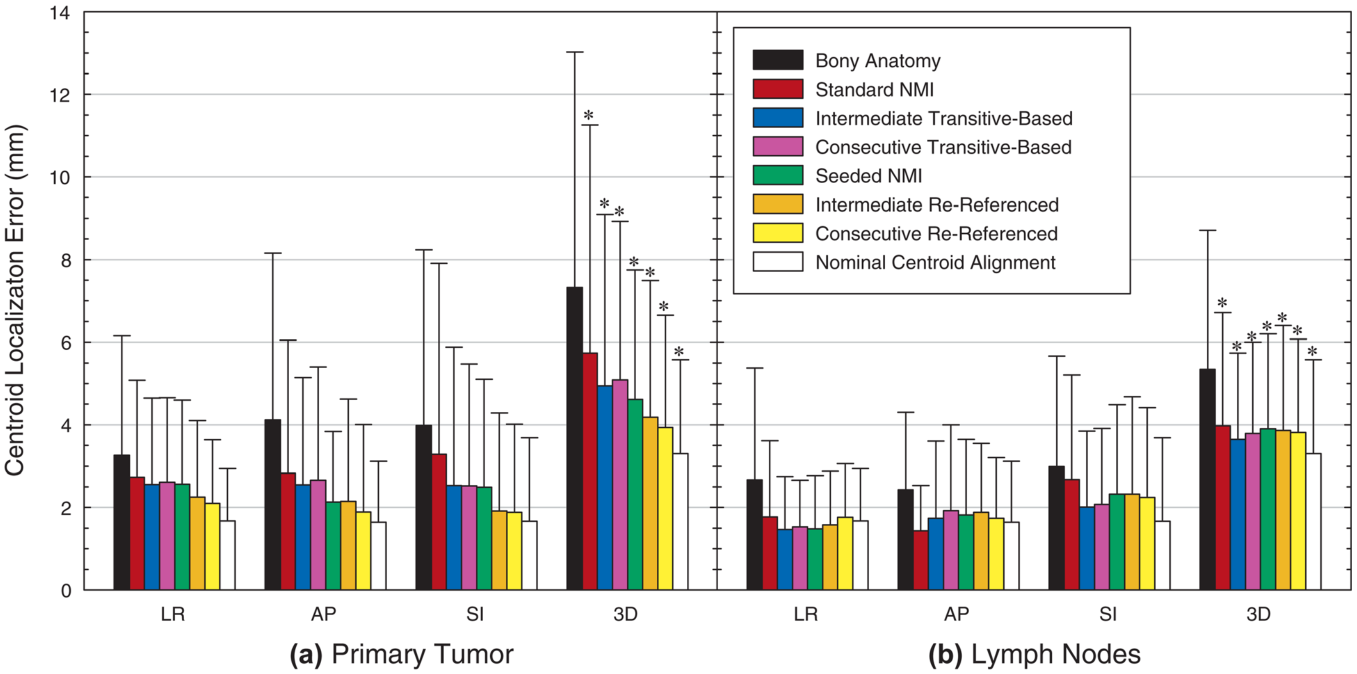

FIG. 5. Mean absolute centroid LE in the LR, AP, and SI directions and in three-dimensional magnitude (3D) after simultaneous "Averaged" registration of both the primary tumor and involved lymph nodes. This registration technique involved separate alignments of each individual target volume, which were then averaged together to obtain the final transform. Nominal centroid alignment was defined as the registration that minimized centroid LE for all targets simultaneously using only translational degrees of freedom, indicating the degree of intertarget variability throughout treatment. Asterisks denote significantly improved target localization relative to the initial bony-anatomy alignment. NMI: normalized mutual information.

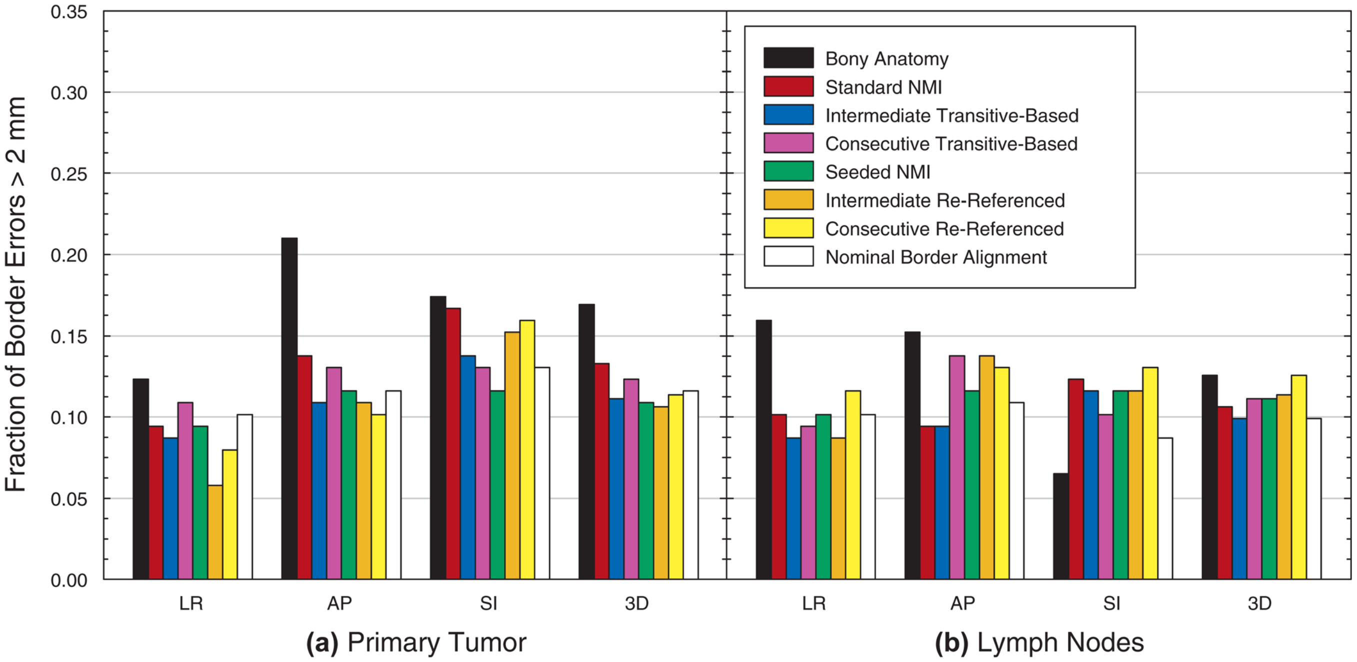

FIG. 6. Frequency of target border LE greater than 2 mm in the LR, AP, and SI directions and in all three dimensions (3D) after simultaneous "Averaged" registration of both the primary tumor and involved lymph nodes. This registration technique involved separate alignments of each individual target volume, which were then averaged together to obtain the final transform. Nominal border alignment was defined as the transformation that minimized localization errors for opposing target borders in each cardinal direction. NMI: normalized mutual information.

III.B. Simultaneous target registration

The collective method for simultaneous target registration demonstrated centroid LE ranging from 1.2 to 1.8 times greater than the corresponding averaged technique (Table III). Because averaged registrations consistently performed better for the current study population, this technique was exclusively chosen for further analysis. Figure 5 shows the mean absolute centroid LE for the primary tumor and involved lymph nodes using the averaged method of simultaneous target registration. Using a Friedman test, all automatic and semi-automatic registrations provided significant improvement over the initial bony alignment ($p < 0.020$). Consecutive-RR registration also reduced target centroid LE relative to standard registration by a significant margin ($p = 0.012$). Using nominal centroid alignment, minimum centroid LE of 3.3 ± 2.3 mm from manual target alignment was possible. These errors were significantly lower than all other registrations ($p < 0.012$) and provided an indication of intertarget variability throughout treatment.

In terms of border localization (Table IV, Fig. 6), the frequencies of border LE greater than 2 mm from bony alignment were 0.169 for the GTV_P and 0.126 for the GTV_{LN}. As with centroid LE, border LE frequencies were generally larger for collective registration than for averaged registration. The frequency of errors for averaged registration approached and in some cases surpassed the LE frequency from manual border alignment, generally at the expense of larger border LE for the other target. Seeded, averaged registration provided the most consistent border alignment, with frequencies of 0.11 for both targets. For comparison, minimum frequencies of 0.12 and 0.10 for the GTV_P and GTV_{LN}, respectively, were obtained from nominal border alignment.

IV. DISCUSSION

In this study, we aimed to evaluate the performance of rigid registration for localizing targets in locally-advanced lung cancer and to devise techniques to reduce LE for this task. Despite the use of active breathing control, the initial bony alignment resulted in large interfraction LE for the GTV_P, with systematic and random components consistent with those from other studies involving active breathing control.[29,34,35] Initial lymph node LE was also large and was comparable to centroid errors reported by Juhler-Nøttrup *et al.* from respiratory gated CTs acquired throughout treatment.[10] It was possible to reduce LE for both targets using automatic rigid registration. In particular, the NMI algorithm demonstrated better centroid alignment than either the local correlation or cross correlation algorithms. Significant improvements were observed for the GTV_{LN}; however, large GTV_P LE persisted, due in part to pathological and pathology-induced changes throughout treatment.

Seeded NMI registrations further reduced LE for the both targets. This strategy simulated a quick, approximate, manual pre-alignment of treatment targets performed by a clinician to guide the automatic registration. Although not a fully automated technique, manual pre-alignment of targets prior to automatic registration substantially improved 38% of GTV_P and 18% of GTV_{LN} cases having initial bony alignment errors greater than 10 mm. In addition, substantial improvements were demonstrated in 67% of both targets that had LE greater than 10 mm from standard registration.

A more profound improvement was noted for primary tumor localization, as only slight overall LE reductions were noted for the lymph nodes. In practice, no means exist to assess target LE during online image guidance, so this error threshold of 10 mm would be difficult to implement. Instead, clinician judgment would be required to gauge the necessity of seeding to guide automatic registrations.

Transitive-based registrations addressed the potentially large deformations observed in some patients but resulted in larger centroid LE than seeded registrations. Ideally, alignment of images acquired with fewer fractions between them should be more robust against such changes. Transitive-based registrations therefore resulted in the alignment of targets with increased similarity in size, shape, and configuration, which helped to reduce LE. In practice, during routine online guidance, intermediate-TB and consecutive-TB techniques only require a single registration between the on-treatment and intermediate images, as the relative orientation between intermediate and planning CTs will have been established during a previous treatment fraction. Therefore, transitive-based registration is no more costly than standard registration. One disadvantage of transitive-based registration, however, is the propagation of target LE.

While a quality assurance protocol should be an integral part of any automatic registration strategy, this would be especially important for transitive-based registration to avoid composing poor intermediate alignments.[36] Not only would this improve the localization of lung cancer targets but quality assurance may also prevent risk structures from entering treatment fields. For example, as Fig. 1 demonstrates, the correction of lymph node targets may induce large shifts in risk structures, potentially causing sensitive organs like the spinal cord and esophagus to be overdosed. It may be argued that automatic registration with quality assurance would overcomplicate the patient setup process, as an experienced therapist could provide adequate target alignment in a reasonable amount of time. However, for less experienced therapists, and for challenging patient cases (e.g., multiple targets, substantial pathological changes, or pathology-induced changes), an accurate automatic registration tool would greatly assist with target localization. Automatic registration may also improve the consistency of target localization, as manual alignments, including those performed by experts, are prone to some degree of variability.[16]

The most accurate target localization in this study was achieved using the intermediate-RR and consecutive-RR techniques. By establishing an intermediate weekly CT as the new reference for registration, transitive error propagation no longer impacted localization accuracy. The consequence, however, involved offline review to determine the relative orientation between new and original reference images. In the current study, this was accomplished by computing a nominal centroid alignment using existing target contours, which in practice would require recontouring of all target structures for each new reference image. As an alternative, new and original reference images could also be aligned using manual target localization[16] or deformable registration,[27,28] requiring the propagation of corresponding geometric uncertainties into the final LE. Because of the workload associated with rereferencing all intermediate images, consecutive-RR registration was considered too demanding for routine clinical protocols. Instead, we recommend intermediate-RR registration, particularly for patients with substantial target volume regression or pathology-induced changes.

The optimal week for rereferencing was found to be patient specific and difficult to predict *a priori*. The week 3 CT proved to be a reasonable intermediate image for most patients in the current study population, although this was not necessarily the optimal week for rereferencing. Both the normalized target volume and the time span between on-treatment and reference images were poor predictors of the potential improvement of rereferenced registration, relative to standard registration. However, rereferenced registration was considered robust against normalized target volume regression and provided insignificant LE differences between patient subgroups with and without pathology-induced changes. Therefore, establishing a new reference image may only be necessary for patients demonstrating these changes. Such a decision could be implemented as part of a quality assurance protocol. That is, if pathological or pathology-induced changes are observed to complicate automatic registration, centroid LE may be reduced by establishing the current on-treatment image as a new reference for subsequent fractions. More than one intermediate image may be necessary for patients with extraordinarily large deformations, as was the case for one patient whose $\mathrm{GTV_P}$ regressed 51% by week 3 and 81% by week 7. Replanning may be required to mitigate the dosimetric effect of such significant geometrical changes. This introduces the additional complication of target volume redefinition, as microscopic disease within the clinical target volume (CTV) may not necessarily demonstrate the same changes as the GTV. Rather than regenerating the CTV by expansion of each newly contoured GTV throughout treatment, the original CTV could be deformably propagated using the methods of Hugo *et al.*, thus preserving the original volume of soft-tissue for irradiation.[33] Note that recontouring does not necessarily imply replanning, as the orientation of each weekly image is ultimately determined relative to the original planning CT [Eqs. (4) and (5)]. Replanning may further improve treatment delivery but evaluating this hypothesis was outside the scope of the current study.

Prioritizing the alignment of primary tumors at the expense of lymph node targets produced substantial LE due to intertarget variability, consistent with findings from other studies.[18,37] This could lead to clinically relevant deviations in lymph node dose as well as increased dose to nearby risk structures.[38] Knap *et al.* reported that registration of the internal target volume (containing both the $\mathrm{GTV_P}$ and $\mathrm{GTV_{LN}}$) was preferable to the alignment of bony-anatomy or individual targets.[39] However, even though collective registration tended to reduce centroid LE relative to bony alignment, large residual errors persisted for patients in this study. Better target localization was achieved by registering the primary tumor and lymph node targets separately, then computing the unweighted average of individual target registrations. Using nominal centroid alignment based on target contours, minimum centroid LE exceeding 3 mm were observed due to differential variability between primary lung tumors and involved lymph nodes throughout treatment. This indicates that simple couch shifts were not sufficient to correct all interfractional geometric uncertainties.[16,37] Various adaptations of standard registration provided simultaneous target localization that approached this lower threshold, particularly using rereferenced registrations. Further reductions in centroid LE would likely require some form of adaptive radiotherapy, which could compensate for changes in target shape, volume, and configuration.

Coupling adaptation with optimal target localization techniques may provide a more efficient form of adaptive radiotherapy, where rereferenced registration and replanning are not required daily. For example, daily online replanning could theoretically reduce interfractional geometric uncertainties to near zero. However, online replanning remains an expensive process in terms of personnel, process costs, and the time each patient would spend on the treatment table. Instead, a high quality online registration could help to identify cases where replanning is required or where a simple online couch shift is sufficient for target localization. This would reduce the frequency of online replanning in many cases, improving the efficiency of the adaptive process. Furthermore, replanning implies the selection of a new reference image for registration of future fractions. This form of adaptation could therefore reduce the lower bound of target LE and minimize registration errors. More treatment fractions would rely on automatic registration, improving the efficiency of adaptive radiotherapy by reducing the necessary frequency of replanning.

One limitation of this study involved the registration of helical CT scans to simulate patient setup. More realistic clinical protocols would require registration between a planning CT and a cone-beam or megavoltage CT, in which image quality will differ. With cone-beam CT, no difference would be expected in the alignment of high-contrast boundaries between lung tumors and the surrounding lung parenchyma, but poor soft-tissue differentiation of mediastinal tumors and involved lymph nodes may increase LE and complicate registration techniques explored in the current study. Soft-tissue surrogates such as the carina may be necessary to assist with the localization of mediastinal targets from CBCT images. As such, the reader should consider the results of this study to be a lower bound on LE for lung cancer targets during image-guided radiotherapy. This also implies a lower limit on the required size of treatment margins. However, we refrain from computing margins for the current study population because only one source of uncertainty—interfractional geometric variability—was considered. Margin formulations are most useful only when they consider all sources of uncertainty throughout treatment.

As a second potential limitation, comparison of the various registration techniques was based solely on centroid and border LE for the GTV, which may not necessarily correlate with those of the CTV.[33] Optimal GTV localization may also place nearby critical structures at higher risk of irradiation, particularly for tumors demonstrating anisotropic regression. CTV and critical structure localization is the subject of future study. Despite the use of PINNACLE[3] as the only tested platform for data collection, the registration algorithms of this treatment planning system should be generalizable to other registration platforms as well. Finally, only translational degrees of freedom were used in this study to simulate couch shifts, but further improvements in target alignment may be possible by including rotations,[40] especially for simultaneous registration. All of these considerations are important to achieve optimal tumor coverage and normal tissue sparing.

V. CONCLUSIONS

Locally-advanced lung cancer presents a challenge to standard, rigid image registration due to target shape, volume, and configuration changes commonly observed in this disease. To improve target alignment with image-guided radiation therapy, periodically establishing a new reference image for automatic or semi-automatic registration is suggested, particularly for primary lung tumors. For simultaneous alignment of the primary tumor and involved lymph nodes, individual targets should be registered separately and the resulting transformations averaged, rather than aligning the collective volume of all targets with a single registration. Despite improvement in target alignment with these methods, intertarget variability limits the accuracy of simultaneous target registration, indicating that couch shifts cannot be used to correct all localization errors.

ACKNOWLEDGMENTS

The authors wish to thank Dr. Matthew Orton for assisting with delineation and Dr. Nitai Mukhopadhyay for verifying all statistical analyses. This work was partially supported by NIH R01CA116249. None of the authors has any actual or potential conflicts of interest.

[a] Author to whom correspondence should be addressed. Electronic mail: gdhugo@vcu.edu.; Telephone: 804-628-3457; Fax: 804-628-0271.

[1] J. Y. Chang *et al.*, "Image-guided radiation therapy for non-small cell lung cancer," J. Thorac. Oncol. **3**, 177–186 (2008).

[2] M. van Herk *et al.*, "The probability of correct target dosage: Dose-population histograms for deriving treatment margins in radiotherapy," Int. J. Radiat. Oncol., Biol., Phys. **47**, 1121–1135 (2000).

[3] G. K. Beckmann *et al.*, "How can we further improve radiotherapy for stage-III non-small-cell lung cancer?," Lung Cancer **45**, S125–S132 (2004).

[4] J.-J. Sonke and J. Belderbos, "Adaptive radiotherapy for lung cancer," Semin. Radiat. Oncol. **20**, 94–106 (2010).

[5] F.-M. Kong *et al.*, "High-dose radiation improved local tumor control and overall survival in patients with inoperable/unresectable non-small-cell lung cancer: Long-term results of a radiation dose escalation study," Int. J. Radiat. Oncol., Biol., Phys. **63**, 324–333 (2005).

[6] M. Partridge *et al.*, "Dose escalation for non-small cell lung cancer: analysis and modelling of published literature," Radiother. Oncol. **99**, 6–11 (2011).

[7] D. R. Simpson *et al.*, "A survey of image-guided radiation therapy use in the United States," Cancer **116**, 3953–3960 (2010).

[8] D. Verellen, M. D. Ridder, and G. Storme, "A (short) history of image-guided radiotherapy," Radiother. Oncol. **86**, 4–13 (2008).

[9] G. R. Borst *et al.*, "Kilo-voltage cone-beam computed tomography setup measurements for lung cancer patients; first clinical results and

comparison with electronic portal-imaging device," Int. J. Radiat. Oncol., Biol., Phys. **68**, 555–561 (2007).

[10] T. Juhler-Nøttrup *et al.*, "Interfractional changes in tumour volume and position during entire radiotherapy courses for lung cancer with respiratory gating and image guidance," Acta Oncol. **47**, 1406–1413 (2008).

[11] L. A. Dawson and D. A. Jaffray, "Advances in image-guided radiation therapy," J. Clin. Oncol. **25**, 938–946 (2007).

[12] T. G. Purdie *et al.*, "Cone-beam computed tomography for on-line image guidance of lung stereotactic radiotherapy: localization, verification, and intrafraction tumor position," Int. J. Radiat. Oncol., Biol., Phys. **68**, 243–252 (2007).

[13] I. S. Grills *et al.*, "Image-guided radiotherapy via daily online cone-beam CT substantially reduces margin requirements for stereotactic lung radiotherapy," Int. J. Radiat. Oncol., Biol., Phys. **70**, 1045–1056 (2008).

[14] A. R. Yeung *et al.*, "Tumor localization using cone-beam CT reduces setup margins in conventionally fractionated radiotherapy for lung tumors," Int. J. Radiat. Oncol., Biol., Phys. **74**, 1100–1107 (2009).

[15] G. D. Hugo *et al.*, "Changes in the respiratory pattern during radiotherapy for cancer in the lung," Radiother. Oncol. **78**, 326–331 (2006).

[16] J. Higgins *et al.*, "Comparison of spine, carina, and tumor as registration landmarks for volumetric image-guided lung radiotherapy," Int. J. Radiat. Oncol., Biol., Phys. **73**, 1404–1413 (2009).

[17] F. O. B. Spoelstra *et al.*, "An evaluation of two internal surrogates for determining the three-dimensional position of peripheral lung tumors," Int. J. Radiat. Oncol., Biol., Phys. **74**, 623–629 (2009).

[18] E. D. Donnelly *et al.*, "Assessment of intrafraction mediastinal and hilar lymph node movement and comparison to lung tumor motion using four-dimensional CT," Int. J. Radiat. Oncol., Biol., Phys. **69**, 580–588 (2007).

[19] J. Higgins *et al.*, "Effect of image-guidance frequency on geometric accuracy and setup margins in radiotherapy for locally advanced lung cancer," Int. J. Radiat. Oncol., Biol., Phys. **80**, 1330–1337 (2011).

[20] K. R. Britton *et al.*, "Assessment of gross tumor volume regression and motion changes during radiotherapy for non-small-cell lung cancer as measured by four-dimensional computed tomography," Int. J. Radiat. Oncol., Biol., Phys. **68**, 1036–1046 (2007).

[21] S. C. Erridge *et al.*, "Portal imaging to assess set-up errors, tumor motion and tumor shrinkage during conformal radiotherapy of non-small cell lung cancer," Radiother. Oncol. **66**, 75–85 (2003).

[22] P. A. Kupelian *et al.*, "Serial megavoltage CT imaging during external beam radiotherapy for non-small-cell lung cancer: Observations on tumor regression during treatment," Int. J. Radiat. Oncol., Biol., Phys. **63**, 1024–1028 (2005).

[23] G. Lim *et al.*, "Tumor regression and positional changes in non-small cell lung cancer during radical radiotherapy," J. Thorac. Oncol. **6**, 531–536 (2011).

[24] M. L. Siker, W. A. Tomé, and M. P. Mehta, "Tumor volume changes on serial imaging with megavoltage CT for non-small-cell lung cancer during intensity-modulated radiotherapy: How reliable, consistent, and meaningful is the effect?," Int. J. Radiat. Oncol., Biol., Phys. **66**, 135–141 (2006).

[25] G. Bosmans *et al.*, "Time trends in nodal volumes and motion during radiotherapy for patients with stage III non-small-cell lung cancer," Int. J. Radiat. Oncol., Biol., Phys. **71**, 139–144 (2008).

[26] J. R. Pantarotto *et al.*, "Motion analysis of 100 mediastinal lymph nodes: Potential pitfalls in treatment planning and adaptive strategies," Int. J. Radiat. Oncol., Biol., Phys. **74**, 1092–1099 (2009).

[27] M. Guckenberger *et al.*, "Evolution of surface-based deformable image registration for adaptive radiotherapy of non-small cell lung cancer (NSCLC)," Radiat. Oncol. **4**, 68 (2009).

[28] K. K. Brock *et al.*, "Improving image-guided target localization through deformable registration," Acta Oncol. **47**, 1279–1285 (2008).

[29] C. K. Glide-Hurst, E. Gopan, and G. D. Hugo, "Anatomic and pathologic variability during radiotherapy for a hybrid active breath-hold gating technique," Int. J. Radiat. Oncol., Biol., Phys. **77**, 910–917 (2010).

[30] O. Škrinjar, A. Bistoquet, and H. Tagare, "Symmetric and transitive registration of image sequences," Int. J. Biomed. Imaging **2008**, 1–9 (2008).

[31] R. W. M. Underberg *et al.*, "Time trends in target volumes for stage I non-small-cell lung cancer after stereotactic radiotherapy," Int. J. Radiat. Oncol., Biol., Phys. **64**, 1221–1228 (2006).

[32] C. Woodford *et al.*, "Adaptive radiotherapy planning on decreasing gross tumor volumes as seen on megavoltage computed tomography images," Int. J. Radiat. Oncol., Biol., Phys. **69**, 1316–1322 (2007).

[33] G. D. Hugo *et al.*, "Localization accuracy of the clinical target volume during image-guided radiotherapy of lung cancer," Int. J. Radiat. Oncol., Biol., Phys. **81**, 560–567 (2011).

[34] N. Panakis *et al.*, "Defining the margins in the radical radiotherapy of non-small cell lung cancer (NSCLC) with active breathing control (ABC) and the effect on physical lung parameters," Radiother. Oncol. **87**, 65–73 (2008).

[35] J. Brock *et al.*, "The use of the active breathing coordinator throughout radical non-small-cell lung cancer (NSCLC) radiotherapy," Int. J. Radiat. Oncol., Biol., Phys. **81**, 369–375 (2011).

[36] M. Sharpe and K. K. Brock, "Quality assurance of serial 3D image registration, fusion, and segmentation," Int. J. Radiat. Oncol., Biol., Phys. **71**, S33–S37 (2008).

[37] J.-J. Sonke, J. Lebesque, and M. van Herk, "Variability of four-dimensional computed tomography patient models," Int. J. Radiat. Oncol., Biol., Phys. **70**, 590–598 (2008).

[38] W. van Elmpt *et al.*, "Should patient setup in lung cancer be based on the primary tumor? An analysis of tumor coverage and normal tissue dose using repeated positron emission tomography/computed tomography imaging," Int. J. Radiat. Oncol., Biol., Phys. (in press).

[39] M. M. Knap *et al.*, "Daily cone-beam computed tomography used to determine tumour shrinkage and localisation in lung cancer patients," Acta Oncol. **49**, 1077–1084 (2010).

[40] M. Guckenberger *et al.*, "Magnitude and clinical relevance of translational and rotational patient setup errors: A cone-beam CT study," Int. J. Radiat. Oncol., Biol., Phys. **65**, 934–942 (2006).

APPENDIX II

DEFORMABLE MESH REGISTRATION FOR THE VALIDATION OF AUTOMATIC TARGET LOCALIZATION ALGORITHMS

Deformable Mesh Registration for the Validation of Automatic Target Localization Algorithms

Scott Robertson, B.Sc., Elisabeth Weiss, M.D., Geoffrey D. Hugo, Ph.D.

Department of Radiation Oncology, Virginia Commonwealth University, Richmond, VA, 23298

Corresponding author

Geoffrey D. Hugo, Ph.D.

Department of Radiation Oncology

Virginia Commonwealth University

401 College Street

PO Box 980058

Richmond, VA 23298

Phone: 804-628-3457

Fax: 804-628-0271

E-mail: gdhugo@vcu.edu

Conflicts of interest

None of the authors has any actual or potential conflicts of interest.

ABSTRACT

Purpose: To evaluate deformable mesh registration (DMR) as a tool for validating automatic target registration algorithms used during image-guided radiation therapy.

Methods: DMR was implemented in a hierarchical model, with rigid, affine, and B-spline transforms optimized in succession to register a pair of surface meshes. The gross tumor volume (primary tumor and involved lymph nodes) were contoured by a physician on weekly CT scans in a cohort of lung cancer patients and converted to surface meshes. The meshes from weekly CT images were registered to the mesh from the planning CT, and the resulting registered meshes were compared with the delineated surfaces. Known deformations were also applied to the meshes, followed by mesh registration to recover the known deformation. Mesh registration accuracy was assessed at the mesh surface by computing the symmetric surface distance (SSD) between vertices of each registered mesh pair. Mesh registration quality in regions within 10 mm of the mesh surface was evaluated with respect to a high quality deformable image registration.

Results: For 18 patients presenting with a total of 19 primary lung tumors and 24 lymph node targets, the SSD averaged 1.3 ± 0.5 mm and 0.8 ± 0.2 mm, respectively. Vertex registration errors (VRE) relative to the applied known deformation were 0.8 ± 0.7 mm and 0.2 ± 0.3 mm for the primary tumor and lymph nodes, respectively. Inside the mesh surface, corresponding average VRE ranged from 0.6 to 0.9 mm and 0.2 to 0.9 mm, respectively. Outside the mesh surface, average VRE ranged from 0.7 to 1.8 mm and 0.2 to 1.4 mm. The magnitude of errors generally increased with increasing distance away from the mesh.

Conclusions: Provided that delineated surfaces are available, deformable mesh registration is an accurate and reliable method for obtaining a reference registration to validate automatic target

registration algorithms for image-guided radiation therapy, specifically in regions on or near the target surfaces.

Key words

Image-guided radiation therapy, deformable registration, localization, lung cancer

I. INTRODUCTION

Image-guided radiotherapy has facilitated substantial improvements in target localization accuracy.[1] Many studies have explored the use of direct target alignment to reduce treatment margins and improve the overall precision of radiotherapy delivery.[2–4] For lung cancer alone, several groups have demonstrated the feasibility and benefit of automatic or semi-automatic soft-tissue-based rigid registration for localizing primary tumors.[5,6] The ability of these registration algorithms to provide fast, reproducible target alignment makes them attractive for patient positioning. However, large anatomical changes during treatment and the limited image quality of onboard imaging systems can impact the accuracy of automated rigid target registration.[7] As a result, interest in deformable and semi-deformable registration during image-guided radiation therapy is mounting, with efforts including the multi-region of interest registration technique for head-and-neck tumors[8] and model-based registration for liver tumors.[9] In locally-advanced non-small cell lung cancer, targets are often dynamic, demonstrating substantial shape and volume change throughout conventionally fractionated radiotherapy.[10,11] Development and implementation of deformable registration to guide online tumor localization would also be warranted in this site.

During algorithm development and before clinically implementing deformable registration algorithms for the purpose of target localization, an important preliminary step involves their validation and establishing residual error that can be used to help determine appropriate margins. A tumor is considered to be well-localized during treatment if its surface can be positioned inside the same target from the planning CT. Validation must therefore be capable of identifying potential misalignments in the tumor surface resulting from automatic registration. A common strategy involves physician delineation of targets on both planning and localization images. By propagating the target contour through registration from one image to the other, the propagated and delineated contours can be compared as an assessment of registration quality.

An appropriate measure must be selected for comparing propagated and delineated contours that provides information on the accuracy of the registration algorithm. In this application, strategies such as volume overlap[3] are not useful for comparing the contours, as they provide no information on spatial error that can be used for margin formulation. Surface border error[12,13] and other distance-to-surface methods provide a measure of spatial accuracy. However, because manual delineated contours lack point-to-point correspondence information, distance-to-surface metrics measure radial errors between surfaces, and cannot identify exact distance between corresponding points on the surfaces. Identification of a distribution of corresponding intensity features or landmarks between the two registered images may solve this problem, but seems superfluous if the physician-delineated target contours are already available on both images.

Furthermore, direct comparison of surfaces with a distance-to-surface metric results in high sensitivity to the high-frequency component of manual delineation error. For example, delineation on axial slices is known to result in substantial slice-to-slice variability, which leads to rough surface contours. In the case of perfect registration, the rough surface contours would result in the distance-to-surface metric being on the order of the slice-to-slice contour variability.

This issue makes it difficult for distance-to-surface metrics to distinguish between registration accuracy and delineation error.

To solve these problems, we propose to use deformable mesh registration (DMR) algorithm to align surface meshes from physician-delineated targets, and to parameterize the resulting transform with a cubic B-spline algorithm. This basis was selected 1) so that the transform can be estimated near as well as on the surface, and 2) so that the coarseness of the B-spline grid can be controlled to reduce the effect of manual delineation error on the registration. The primary purpose of this study is to evaluate the accuracy of an in-house DMR algorithm using meshes with known vertex-to-vertex correspondence. The accuracy of this tool is assessed by comparison against a known transform from intensity-based deformable image registration (DIR). Evaluation is conducted for the target surface as well as for regions near the surface. We also assess the ability of DMR to align physician-delineated surface meshes where the vertex-to-vertex correspondence is unknown.

II. METHODS

A deformable mesh registration tool was developed for the non-rigid alignment of a pair of surface meshes. The accuracy of this tool was assessed using physician-delineated targets as well as deformably-propagated targets generated from a known transform. Deformable mesh registration was then compared against this known deformation to evaluate the registration accuracy both on and near the mesh surface.

II.A. Deformable mesh registration

An in-house DMR tool was implemented using the Insight Segmentation and Registration Toolkit[14] (v3.20) to consist of three transforms optimized sequentially, as shown in Figure 1. First, a rigid similarity transform provided translational and rotational degrees of freedom in addition to a single uniform scaling parameter. This scaling promoted a more robust initial alignment for regressing target structures than rigid registration without scaling. The next step involved an affine transform with three-dimensional scaling and shearing parameters in addition to any further translational and rotational corrections. Lastly, a deformable B-spline transform fine-tuned the registration and yielded the final mesh alignment.

The similarity between reference and moving meshes was computed using the symmetric Euclidean distance. Briefly, the magnitude of all nearest-neighbor distances was calculated in both directions: from reference mesh vertices to the moving mesh and from moving mesh vertices to the reference mesh. This accounted for the orientation of both surfaces relative to each other, as opposed to the unidirectional Euclidean distance commonly employed in point set registrations.[15] Although this did not guarantee symmetry in the final forward and inverse transforms, preliminary tests demonstrated that the symmetric Euclidean distance did increase the consistency between these transforms. These distances were minimized during the registration process using the Levenberg-Marquardt algorithm, which was applied separately for each of the three sequential transforms.[16]

II.B. Physician-delineated and deformably-propagated surface meshes

Computed tomography (CT) images were acquired once per week throughout radiotherapy treatment for 18 lung cancer patients using an active breath-hold technique. Four to seven weekly CTs were available for each patient. Refer to Weiss *et al.* for details on the study population and to Glide-Hurst *et al.* regarding the imaging protocol.[10,17] One patient presented with two primary tumors, and 15 patients presented with between 1 and 4 involved lymph nodes, for a total of 19 tumors and 24 involved lymph nodes in this study. Treatment targets were contoured on all images by a physician and converted to surface meshes using the Pinnacle^3

treatment planning system (version 8.1, Philips Medical Systems, Fitchburg, WI). Primary tumors ranged in size from 0.6 to 377.3 cm^3 (median: 50.8 cm^3) and contained between 414 and 3097 mesh vertices (median: 2350). The lymph node targets ranged from 0.4 to 17.8 cm^3 (median: 2.2 cm^3) and contained 266 to 2170 mesh vertices (median: 448). Meshes contained an average of 50 vertices per cm^2 surface area, which provided sufficiently accurate registrations without demanding extensive run times. Registrations were performed on the Pinnacle workstation and required between 5 and 25 minutes to compute all three transforms.

The first image (labeled 'week 1') generally corresponded to the planning CT, so all targets from the week 1 CT were designated as reference meshes for deformable registration. Corresponding weekly tumors and involved nodes designated as moving meshes. All weekly images were initially registered to the planning CT by manually aligning bony-anatomy. A total of 93 primary tumor registrations and 119 lymph node registrations were then performed using these surface meshes. For patients presenting with multiple primary tumors and/or multiple metastatic lymph nodes, each individual target structure was contoured and registered separately.

Physician-delineated meshes marked the ground truth for this study, but no correspondence existed between the vertices from reference and moving meshes, which precluded the calculation of mesh registration errors. To provide a known correspondence for initial validation of the deformable mesh registration, a second set of moving meshes was generated by deformably propagating the reference meshes to all other weekly images using a known transform. The known transform was obtained from previous intensity-based deformable image registration studies in this dataset[18] using the small deformation, inverse consistent linear elastic (SICLE) algorithm.[19] Briefly, SICLE uses a cost function composed of a sum of squared distances similarity metric, a linear elasticity penalty term, an inverse consistency penalty term, and a Fourier basis to represent the transform. For two patients, resolving atelectasis throughout treatment prohibited accurate image registration with SICLE, so their treatment targets were excluded from the analysis of deformably-propagated meshes. Thus, 104 and 135 primary tumor and lymph node meshes were included in 86 and 112 registrations, respectively.

II.C. Analysis

II.C.1. Mesh registration accuracy

Registrations were first performed for the deformably-propagated meshes. Because the correspondence of vertices was preserved after applying the known transform, it was possible to compute the distance from each vertex on the moving mesh to its known location on the reference mesh. These distances provided a measure of the **vertex registration error** (VRE). Prior to and after each step in the registration process, the average, root-mean-square (RMS), and maximum VRE were tabulated. The mean and standard deviation for each of these statistics was then computed separately over all primary tumor registrations and all lymph node registrations.

Next, registrations were performed for the physician-delineated meshes. In this case, no correspondence existed between vertices of reference and moving meshes, precluding the calculation of VRE. The quality of mesh alignment was instead computed using the **symmetric surface distance** (SSD), a metric very closely related to the symmetric Euclidean distance utilized in DMR.[20] Prior to and after each step in the registration, the average SSD was given by the mean of all nearest-neighbor vertex distances in both directions (reference mesh vertices to the moving mesh as well as moving mesh vertices to the reference mesh); the RMS SSD was given by the square root of the mean of the squared nearest-neighbor distances in both directions; and the maximum SSD was given by the single largest nearest-neighbor distance in either direction (also known as the Hausdorff distance). As with VRE, the mean and standard deviation for each of these statistics was computed separately over all primary tumor registrations and all lymph node registrations. Note that the SSD did not constitute a true error metric. This measure only indicated how closely the vertices of two surface meshes were aligned.

II.C.2. Mesh registration regional consistency

In order for mesh registration to provide a useful validation for target localization from intensity-based registration algorithms, the mesh registration tool must be accurate not just on the surface but near it as well, since presumably a deformable target localization algorithm will use intensity information near the surface to drive the registration. The following methods were designed to extend the VRE analysis to regions surrounding the surface of target meshes. After deformable registration of propagated meshes, the resulting B-spline transform was sampled at the center of all voxels on or near the surface of the reference mesh. The resulting deformation vectors were compared against the known intensity-based deformation that was used to generate these propagated meshes. At the surface of the meshes, the two deformation fields were expected to demonstrate accuracy similar to the VRE measured above. Therefore, the goal of this analysis was to quantify the accuracy of deformable mesh registration near, but not on, the surface.

To accomplish this goal, the reference mesh was converted to a binary surface mask to limit the analysis to only those voxels within a narrow band on the mesh surface. A distance map was then used to compute the proximity of all neighboring voxels to the binary mask, measured in an integer number of voxels.[14,21] This allowed the binary mask to be expanded (positive voxels) or contracted (negative voxels) for analysis of additional bands of image voxels which varied with proximity to the surface of the reference mesh. Expansions and contractions of up to 5 voxels were considered in this study, corresponding to distances of up to 10 mm from the mesh surface for 1.2×1.2×2.0 mm^3 voxels. On a voxel-by-voxel basis within each narrow band, the difference vectors were computed between the deformation fields from DMR and the known transform. The absolute mean, RMS, and maximum of the magnitude of the difference vectors were tabulated for each propagated mesh registration. These statistics were then averaged over all primary tumor registrations and all lymph node registrations.

To further evaluate the regional consistency of DMR with respect to the known deformation, a sub-volume was defined around each voxel, spanning a diameter of 1 to 17 voxels. Then, all difference vectors within a given sub-volume were averaged to obtain a measure of the local agreement between DMR and the known deformation. This analysis was conducted as a function of distance from the mesh surface, with the absolute mean and maximum magnitude of difference vectors recorded for each propagated mesh registration.

III. RESULTS

III.A. Mesh registration accuracy

Figure 2 shows the vertex registration errors (VRE) for the deformably-propagated target meshes in their initial alignment and following each transform in the registration process. Errors for the unregistered primary tumor averaged 7.2 ± 4.5 mm, but individual vertices demonstrated maximum errors as large as 11.9 ± 7.2 mm. The rigid transform reduced the average and maximum errors to 2.3 ± 1.6 mm and 5.3 ± 3.5 mm, respectively, with additional improvements provided by the affine and B-spline transforms. After registration, the final average VRE was 0.8 ± 0.7 mm (range: 0.0 to 1.5 mm), with maximum errors of 3.2 ± 2.9 mm (range: 0.0 to 10.1 mm). Lymph node registrations demonstrated a similar trend. Average VRE for this target was 5.9 ± 3.9 mm prior to registration and 0.8 ± 0.5 mm after the rigid transform. Final average and maximum VRE were 0.2 ± 0.3 mm (range: 0.0 to 0.8 mm) and 0.8 ± 1.1 mm (range: 0.0 to 3.4 mm), respectively.

For comparison between VRE and SSD metrics, we also computed the SSD for the deformably-propagated target meshes. After the final B-spline transform, the average and maximum SSD were 0.7 ± 0.5 mm and 2.0 ± 1.5 mm for the primary tumor, and 0.2 ± 0.2 mm and 0.6 ± 0.7 mm for lymph nodes.

For physician-delineated meshes, Figure 3 summarizes the SSD throughout the registration process. The average primary tumor SSD was 4.1 ± 2.8 mm prior to registration, with maximum SSD of 15.2 ± 7.9 mm. After deformable mesh registration, the B-spline transform resulted in an average SSD of 1.3 ± 0.5 mm (range: 0.1 to 9.0 mm) and a maximum SSD of 4.5 ± 1.9 mm (range: 1.2 to 9.9 mm). For the lymph nodes, the average SSD prior to registration was 3.2 ± 2.1 mm, with a maximum SSD of 8.4 ± 4.4 mm. The B-spline transform resulted in an average SSD of 0.8 ± 0.2 mm (range: 0.1 to 0.9 mm), with a maximum SSD of 2.1 ± 0.8 mm (range: 1.3 to 3.7 mm).

III.B. Mesh registration regional consistency

Figure 4 highlights the results of a voxel-by-voxel comparison of the transform vectors from deformable mesh registration and the known deformation field. At the surface of primary lung tumors, the magnitude of transform vector differences averaged 0.6 ± 0.5 mm and demonstrated maximum differences of 2.5 ± 2.5 mm. These differences were noted to increase with increasing distance from the mesh. Inside the reference mesh (represented by negative voxel distances), differences averaged 0.6 to 0.9 mm. Average vector differences outside the mesh surface ranged from 0.7 to 1.8 mm, with maximum differences ranging from 3.3 to 8.2 mm. For lymph node registrations, the average and maximum transform vector differences were 0.2 ± 0.3 mm and 0.6 ± 1.0 mm at the surface of these targets. Average vector differences ranged from 0.2 to 0.9 mm inside the lymph node surface and 0.2 to 1.4 mm outside the surface. Maximum errors of1.1 ± 0.8 mm and 5.5 ± 6.1 mm were computed at a distance of five voxels inside and outside the mesh surface, respectively.

Figure 5 demonstrates the effect of local averaging within regions of varying diameter. On the surface of primary tumor meshes, the average magnitude of differences between DMR and the known deformation ranged from 0.5 to 0.6 mm. At a distance of five voxels, average differences were 0.5 to 0.9 mm inside the mesh and 1.6 to 1.8 mm outside the mesh. In both cases, the differences were generally reduced as the region diameter increased. The maximum differences for primary tumor registrations ranged from 2.4 to 2.8 mm at the mesh surface, from 1.3 to 2.0 mm five voxels inside the mesh surface, and from 6.7 to 8.2 mm five voxels outside the mesh surface. Similar trends were noted for lymph node registrations. Average differences of 0.2 to 0.5 mm, 0.2 to 0.9 mm, and 0.9 to 1.4 mm were observed on the mesh surface, five voxels inside the mesh, and five voxels outside the mesh, respectively. Corresponding maximum errors for the lymph nodes were 0.5 to 1.2 mm, 0.2 to 1.1 mm, and 2.7 to 5.5 mm. At a distance of 5 voxels inside or outside the mesh surface, differences were again reduced as the region diameter increased.

IV. DISCUSSION

This study aimed to evaluate deformable mesh registration as a validation tool for deformable and semi-deformable image registration algorithms for automatic target localization in image-guided radiation therapy. The developed DMR algorithm demonstrated vertex registration errors for the deformably-propagated meshes that were less than the voxel size for images in this study. Primary tumor registrations contributed larger errors than lymph node registrations. This was because the primary tumors were generally larger and more irregularly shaped than the lymph nodes, and thus underwent greater shape and volume change (by absolute distance and volume). Results in this study are relatively consistent with intensity-based registrations, which often demonstrate accuracy on the order of the voxel size or less. This is also less than the range of typical action levels for patient setup corrections, where treatment couch shifts less than 2 to 3 mm are generally ignored.[2,22,23]

Using DMR, intensity-based registration algorithms for online target localization could be validated on and near the target surface by comparison against the DMR transform. It should be noted that DMR was not intended for online validation during image-guided radiotherapy (e.g., as a ‘second check’ of automated registration). Rather, this validation tool was designed for use during the development and validation of intensity-based target localization algorithms to be implemented during online guidance. Because DMR relies solely on the alignment of surface mesh vertices, this approach provides a method of validation that is independent of local intensity values and that is expected to be more robust than DIR against large deformation and tissue change.

The above analysis provides a straightforward method for validating deformable image registration using DMR, an example of which is provided in Figure 6. However, this technique may also be applied to other types of image registration. One particularly suitable application is block-matching registration, in which the rigid alignment of a series of small blocks of image content yields an effective global registration of the entire image.[24,25] In this case, the expected transform for an individual block placed near the surface of a contoured target could be predicted by DMR. If all blocks are registered consistently with the corresponding DMR transforms, then it is likely that the global image registration will adequately capture the contoured target volume. Similar methods may be extended to the validation of rigid and affine transforms as well.

Because the deformably-propagated meshes were generated from intensity-based registration of the weekly CTs, these meshes were reasonably similar to the physician-delineated meshes for the patients in this study. Exceptions were noted for two patients with resolving atelectasis, which was why these patients were excluded from VRE-related studies and limited to SSD-based analysis. The final VRE results were thus expected to provide an estimate of registration errors for physician-delineated meshes, which lacked a known vertex correspondence. Differences between the VRE and SSD were analyzed by computing both metrics for artificially-deformed meshes. As expected, slight reductions were noted for the average SSD, indicating that the nearest-neighbor vertices were generally located very close to the actual corresponding vertices. However, substantially larger differences were noted between the maximum VRE and maximum SSD. This result highlights the potential for large registration errors parallel to the target surface, where nearest-neighbor vertices may be somewhat removed from the true corresponding vertices. The maximum SSD of physician-delineated meshes may therefore be somewhat underestimated. When applying DMR as a validation tool, the average SSD should be computed as the more reliable measure, specifically by considering the transform vectors from a distribution of points throughout the entire target surface.

The SSD for physician-delineated meshes was actually found to be somewhat larger than the VRE of the artificially-deformed meshes, the reason for which may be twofold. First, although contouring uncertainties may impact the initial target from the planning CT, no additional contouring variability was present for the remaining artificially-deformed meshes. In contrast, the physician-delineated meshes were all created independently, and contouring variability between targets could have potentially contributed to larger SSD results. The second reason likely stemmed from the fact that the known deformation in this study only approximated the true underlying anatomic and pathological changes for patients in this study. Because the physician-delineated meshes were identified on the actual patient images, these meshes likely incorporated a greater degree of irregularity that was actually present in the weekly CTs. These mesh irregularities could have also potentially contributed to larger SSD results.

The final DMR transform, as well as the magnitude of the SSD metric, has some dependence on the density of points in the surface mesh. In this work, targets contained an average of 50 vertices per cm^2 (range: 12 to 120) along their surface, which was selected to balance registration accuracy and execution time. Increasing the density of mesh vertices would have likely had a negligible influence on the final DMR transform and on the SSD reported in this study. However, decreasing the number of mesh points could potentially introduce a slight degree of variability in the final transform and could also increase the SSD by a small amount. The extent of this effect would depend on how sparsely distributed the mesh vertices were. In general, we anticipate a very small impact on the DMR transform for all but the most sparsely sampled vertex distributions.

The focus of this study involved the application of DMR to validate intensity-based registration of local image sub-volumes. For image voxels at the surface of the propagated meshes, the transform vectors from deformable mesh registration demonstrated sub-millimeter agreement with a known deformation field. The average magnitude of vector differences was found to be consistent with the average VRE, as expected. Furthermore, these discrepancies remained relatively constant inside the surface of target meshes. Larger discrepancies, however, were noted outside the surface of these meshes. This indicates that while DMR may be a reliable validation tool on or just inside the target surface, uncertainties can become much more substantial at distances farther outside these volumes. It was possible to reduce uncertainties by averaging the result of DMR over localized regions, but as evident in Figure 5, large uncertainties persisted at greater distances outside the mesh surface. The scope of DMR as a validation tool should thus be limited to regions near the target surface. Registration accuracy in these regions is one of the primary concerns for target localization, which stems from the importance of orienting the target entirely within the intended radiation fields. For other applications such as dose mapping and adaptive radiotherapy tasks, the requirement for accurate surface alignment is necessary but may not be sufficient, illustrating one of the limitations of our method.

Because DMR relies on target contours, this method is also inherently limited by contouring variability. The surface of primary lung tumors is generally well-visualized against the surrounding lung parenchyma, improving the reliability of contours in these regions. Larger variability may be expected for tumors extending into the mediastinum or bordering atelectasis. Systematic contouring errors along these parts of the tumor surface would lead directly to local systematic errors in the deformable mesh transform, consequently leading to larger discrepancies between DMR and DIR in these regions. Because of the reduced contrast in the mediastinum or near atelectasis, however, discrepancies between the two algorithms could also stem from uncertainties in the intensity-based registration. Operator judgment may be necessary to resolve the true source of discrepancies in this case.

Contouring variability with high spatial frequency, such as slice-to-slice variability, is not anticipated to substantially detract from the final DMR transform. This is because B-spline registration provides a locally smooth transform in which the effect of purely random fluctuations should cancel out. Relatively few B-spline control points are used in this study to promote a smooth transform and avoid over-fitting the mesh models. This effect can be observed in the rightmost panel of Figure 1, where the high-frequency ‘roughness’ of the contours has not been smoothed out by the registration.

As a final limitation, deformable mesh registration cannot be considered a “ground truth” for determining the registration errors of other algorithms because of potential contouring variability noted above as well as the registration errors reported in this work. Instead, in lieu of a ground truth, DMR is intended to serve as a standard metric for comparing different intensity-based registrations at or near the tumor surface(Figure 6). We expect that DMR provides a reasonably accurate approximation of the true underlying changes in anatomy as it is based on the physician’s clinical judgment and potentially other sources of clinical information (e.g., PET/CT). In general, a DIR algorithm in better agreement with DMR is more likely to reflect the underlying anatomical changes at the target surface than another algorithm with worse agreement. This logic may also be applied to algorithm development, where two different versions of a code could both be compared against DMR to determine which better localizes the target surface. Future work will involve the application of DMR in this capacity, as we work toward robust automatic registration tools for target localization.

V. CONCLUSION

A deformable mesh registration tool has been implemented for the purpose of validating the quality of target localization from automatic image registration in image-guided radiation therapy. The sub-voxel accuracy of this tool was reasonable for the specific application of target localization, with errors less than the typical action levels of modern patient setup protocols. Although this tool is limited to validating registrations of the image sub-volumes encompassed by the given meshes, its applicability extends to both rigid (including affine) and non-rigid registration problems.

ACKNOWLEDGEMENTS

This work was partially supported by NIH R01CA166119. It relied on the Insight Segmentation and Registration Toolkit (ITK), an open source software developed as an initiative of the U.S. National Library of Medicine and available at www.itk.org.

TABLES AND FIGURES

Figure 1. Starting with the initially unregistered meshes, deformable mesh registration proceeds through three sequential steps: (1) a rigid similarity transform that includes an isotropic scaling parameter, (2) an affine transform, and (3) a B-spline deformable transform.

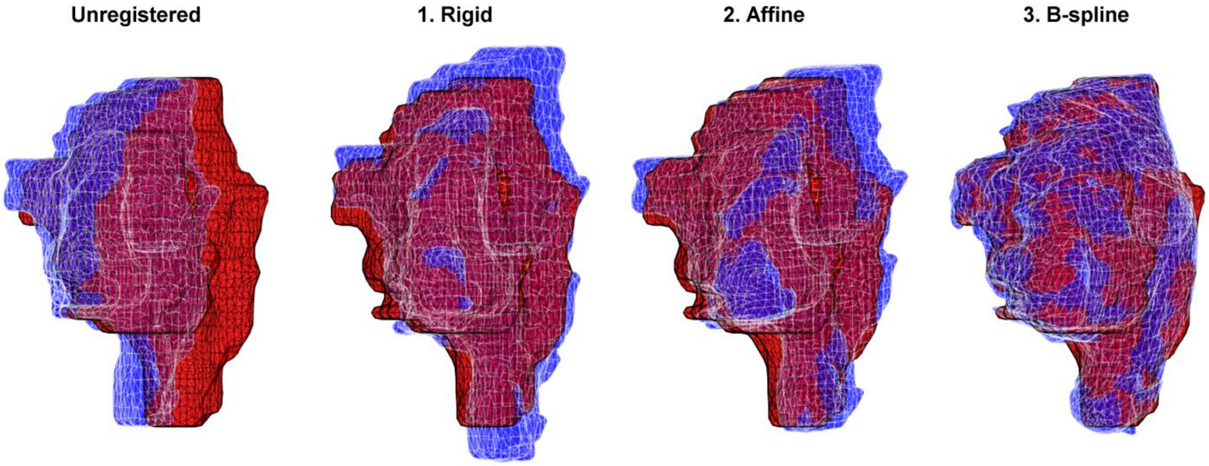

Figure 2. Average, root-mean-square (RMS), and maximum vertex registration errors between reference and *deformably propagated* surface meshes at each step in the registration process. Error bars represent one standard deviation across all target registrations.

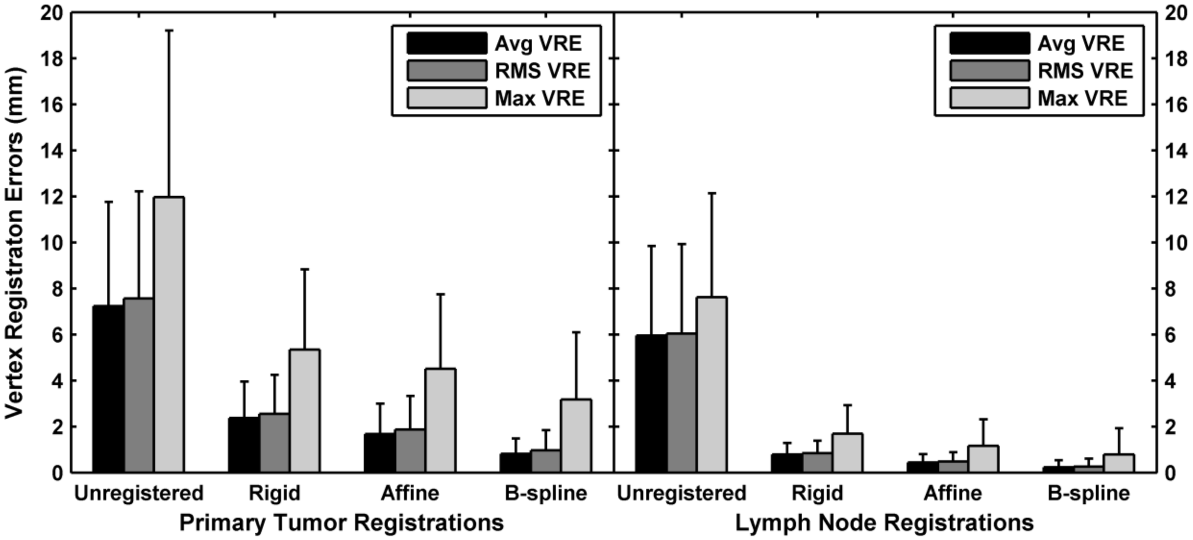

Figure 3. Average, root-mean-square (RMS), and maximum symmetric surface distances between reference and *physician-delineated* meshes at each step in the registration process. Error bars represent one standard deviation across all target registrations.

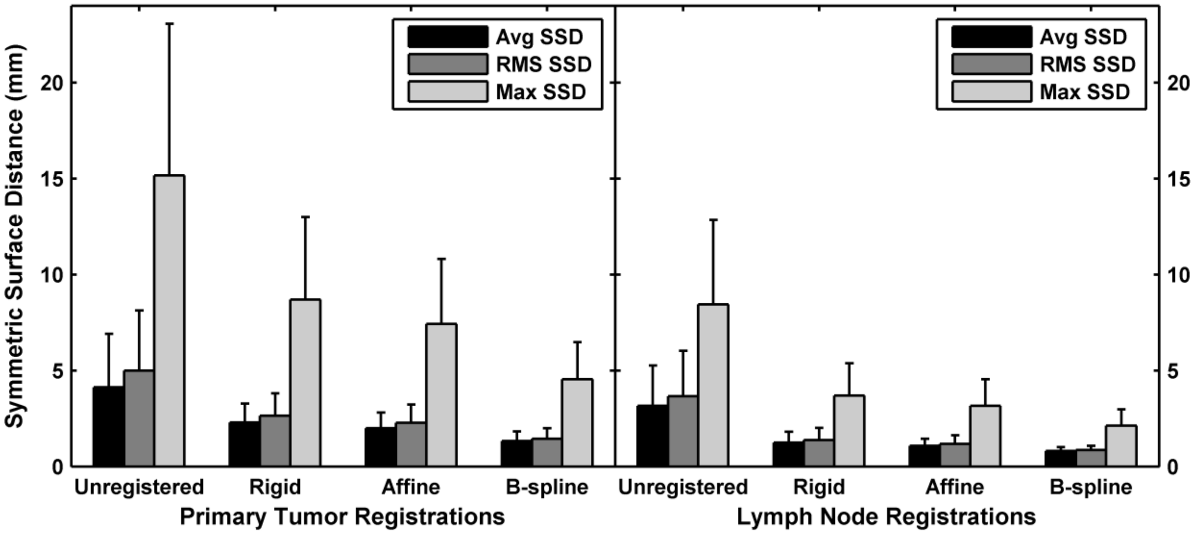

Figure 4. Average, root-mean-square, and maximum of the magnitude of the differences between transform vectors from deformable mesh registration and the known deformation, plotted as a function of distance (in voxels) from the fixed mesh surface. Positive distances represent outward displacements from the surface mesh.

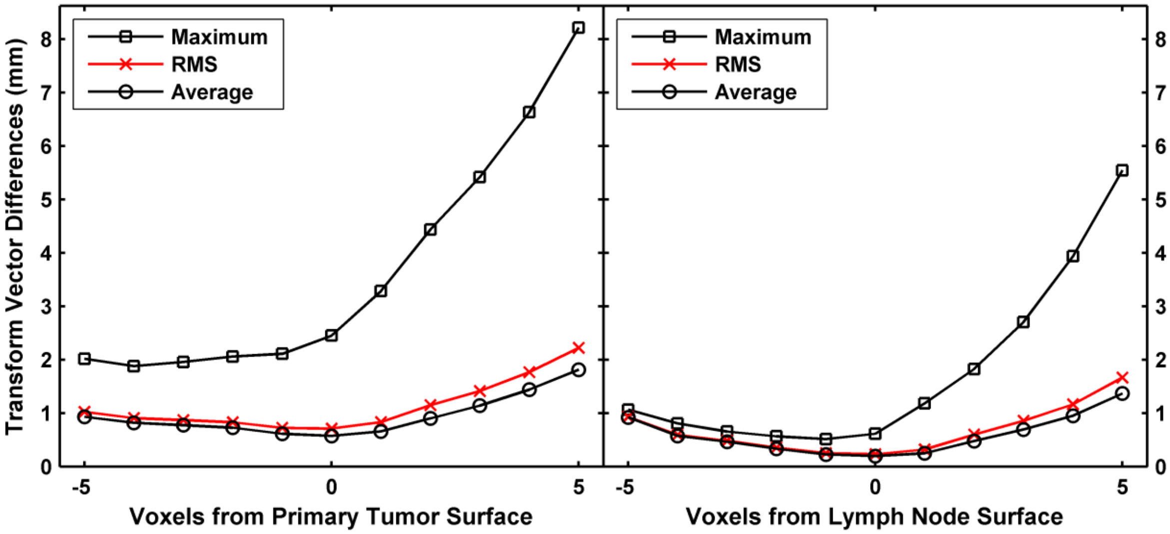

Figure 5. Average (top row) and maximum (bottom row) of the regional differences between deformable mesh registration and a known deformation for primary tumor meshes (left column) and lymph node meshes (right column). Results were assessed as a function of both region size and the distance from the center voxel of a given region to the mesh surface.

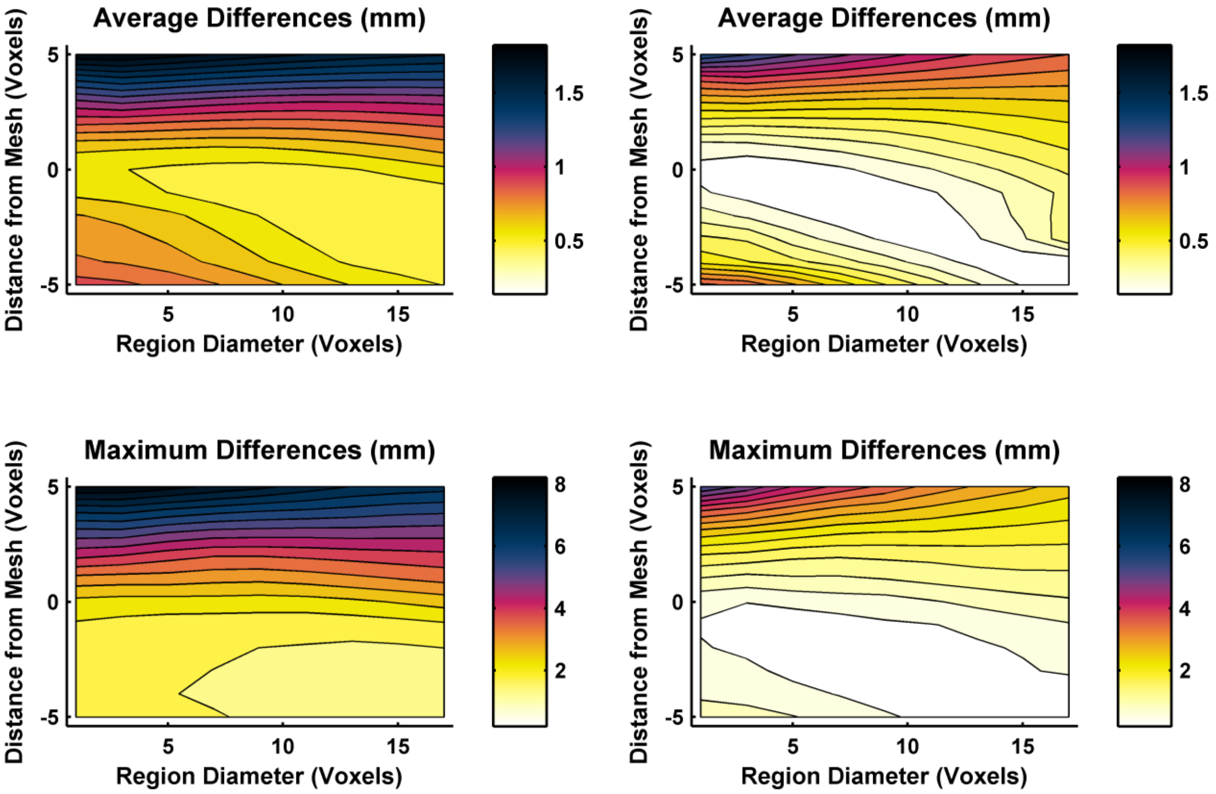

Figure 6. Deformable mesh registration (DMR) for validation of automatic intensity-based target registration algorithms. The initial primary GTV (top left) demonstrated some regression and shape change by week 5 of treatment (top center). Intensity-based deformable image registration (DIR) was performed between these two CTs (top right), and the transform vectors were computed from DIR at each vertex on the initial GTV surface mesh (bottom left, shown for the current slice only). By comparing these transform vectors against those from DMR (bottom center), the resulting differences (bottom right) can be used to detect inconsistency between DMR and DIR. In this case, it is clear from the top right panel that the DIR algorithm underestimated the magnitude of tumor volume change, consistent with the difference between DMR and DIR deformation fields.

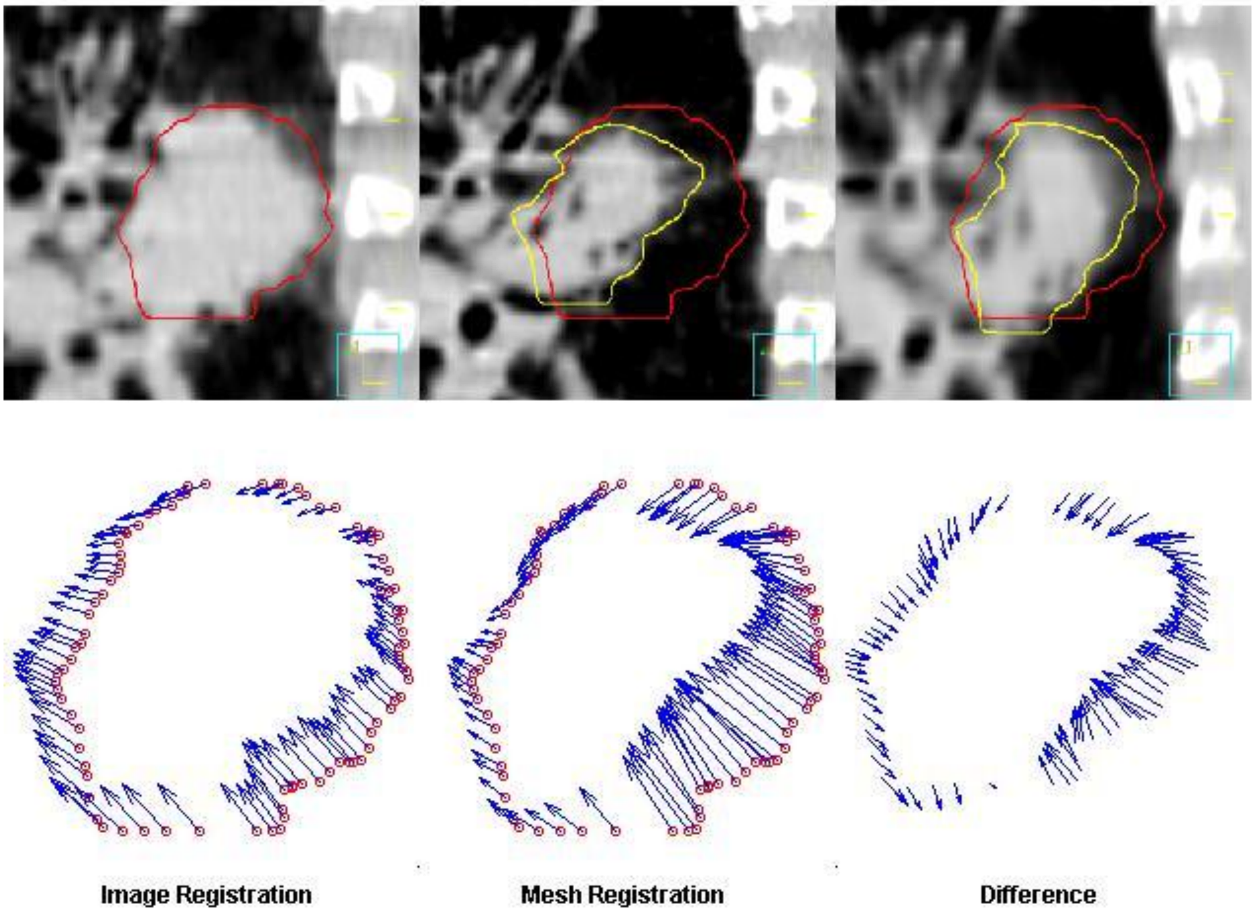

Image Registration

Mesh Registration

Difference

REFERENCES

[1]M. van Herk, “Different styles of image-guided radiotherapy,” Semin. Radiat. Oncol. **17**, 258–267 (2007).

[2]J.-P. Bissonnette, T. G. Purdie, J. A. Higgins, W. Li, and A. Bezjak, “Cone-beam computed tomographic image guidance for lung cancer radiation therapy,” Int. J. Radiat. Oncol., Biol., Phys. **73**, 927–934 (2009).

[3]N. Mohammed, L. Kestin, I. Grills, C. Shah, C. Glide-Hurst, D. Yan, and D. Ionascu, “Comparison of IGRT registration strategies for optimal coverage of primary lung tumors and involved nodes based on multiple four-dimensional CT scans obtained throughout the radiotherapy course,” Int. J. Radiat. Oncol., Biol., Phys. **82**, 1541–1548 (2012).

[4]E. S. Worm, A. T. Hansen, J. B. Petersen, L. P. Muren, L. H. Præstegaard, and M. Høyer, “Inter- and intrafractional localisation errors in cone-beam CT guided stereotactic radiation therapy of tumours in the liver and lung,” Acta Oncol. **49**, 1177–1183 (2010).

[5]A. R. Yeung, J. G. Li, W. Shi, H. E. Newlin, A. Chvetsov, C. Liu, J. R. Palta, and K. Olivier, “Tumor localization using cone-beam CT reduces setup margins in conventionally fractionated radiotherapy for lung tumors,” Int. J. Radiat. Oncol., Biol., Phys. **74**, 1100–1107 (2009).

[6]J. Higgins, A. Bezjak, K. Franks, L. W. Le, B. C. Cho, D. Payne, and J.-P. Bissonnette, “Comparison of spine, carina, and tumor as registration landmarks for volumetric image-guided lung radiotherapy,” Int. J. Radiat. Oncol., Biol., Phys. **73**, 1404–1413 (2009).

[7]J.-J. Sonke and J. Belderbos, “Adaptive radiotherapy for lung cancer,” Semin. Radiat. Oncol. **20**, 94–106 (2010).

[8]S. van Beek, S. van Kranen, A. Mencarelli, P. Remeijer, C. Rasch, M. van Herk, and J.-J. Sonke, “First clinical experience with a multiple region of interest registration and correction method in radiotherapy of head-and-neck cancer patients,” Radiother. Oncol. **94**, 213–217 (2010).

[9]K. K. Brock, M. Hawkins, C. Eccles, J. L. Moseley, D. J. Moseley, D. A. Jaffray, and L. A. Dawson, “Improving image-guided target localization through deformable registration,” Acta Oncol. **47**, 1279–1285 (2008).

[10]C. K. Glide-Hurst, E. Gopan, and G. D. Hugo, “Anatomic and pathologic variability during radiotherapy for a hybrid active breath-hold gating technique,” Int. J. Radiat. Oncol., Biol., Phys. **77**, 910–917 (2010).

[11]G. Lim *et al.*, “Tumor regression and positional changes in non-small cell lung cancer during radical radiotherapy,” J. Thorac. Oncol. **6**, 531–536 (2011).

[12]G. D. Hugo, E. Weiss, A. Badawi, and M. Orton, “Localization accuracy of the clinical target volume during image-guided radiotherapy of lung cancer,” Int. J. Radiat. Oncol., Biol., Phys. **81**, 560–567 (2011).

[13]S. P. Robertson, E. Weiss, and G. D. Hugo, "Localization accuracy from automatic and semi-automatic rigid registration of locally-advanced lung cancer targets during image-guided radiation therapy," Med. Phys. **39**, 330–341 (2011).

[14]L. Ibanez, W. Schroeder, L. Ng, and J. Crates, *The ITK Software Guide,* Edition 2.

[15]Z. Zhang, "Iterative point matching for registration of free-form curves and surfaces," Int. J. Comput. Vis. **13**, 119–152 (1994).

[16]B. Zitová and J. Flusser, "Image registration methods: A survey," Image Vis. Comput. **21**, 977–1000 (2003).

[17]E. Weiss, S. P. Robertson, N. Mukhopadhyay, and G. D. Hugo, "Tumor, lymph node, and lymph node-to-tumor displacements over a radiotherapy series: Analysis of interfraction and intrafraction variations using active breathing control (ABC) in lung cancer," Int. J. Radiat. Oncol., Biol., Phys. **82**, e639–e645 (2012).

[18]A. M. Badawi, E. Weiss, W. C. Sleeman IV, and G. D. Hugo, "Classifying geometric variability by dominant eigenmodes of deformation in regressing tumours during active breath-hold lung cancer radiotherapy," Phys. Med. Biol. **57**, 395–413 (2012).

[19]G. E. Christensen, J. H. Song, W. Lu, I. El Naqa, and D. A. Low, "Tracking lung tissue motion and expansion/compression with inverse consistent image registration and spirometry," Med. Phys. **34**, 2155 (2007).

[20]T. Heimann *et al*., "Comparison and evaluation of methods for liver segmentation from CT datasets," IEEE Trans. Med. Imaging **28**, 1251–1265 (2009).

[21]P.-E. Danielsson, "Euclidean distance mapping," Comput. Graph. Image Process. **14**, 227–248 (1980).

[22]G. R. Borst, J.-J. Sonke, A. Betgen, P. Remeijer, M. van Herk, and J. V. Lebesque, "Kilo-voltage cone-beam computed tomography setup measurements for lung cancer patients; First clinical results and comparison with electronic portal-imaging device," Int. J. Radiat. Oncol., Biol., Phys. **68**, 555–561 (2007).

[23]I. S. Grills, G. D. Hugo, L. L. Kestin, A. P. Galerani, K. K. Chao, J. Wloch, and D. Yan, "Image-guided radiotherapy via daily online cone-beam CT substantially reduces margin requirements for stereotactic lung radiotherapy," Int. J. Radiat. Oncol., Biol., Phys. **70**, 1045–1056 (2008).

[24]M. Söhn, M. Birkner, Y. Chi, J. Wang, D. Yan, B. Berger, and M. Alber, "Model-independent, multimodality deformable image registration by local matching of anatomical features and minimization of elastic energy," Med. Phys. **35**, 866 (2008).

[25]U. Malsch, C. Thieke, P. E. Huber, and R. Bendl, "An enhanced block matching algorithm for fast elastic registration in adaptive radiotherapy," Phys. Med. Biol. **51**, 4789–4806 (2006).

APPENDIX III

A BLOCK-MATCHING REGISTRATION ALGORITHM FOR LOCALIZATION OF LOCALLY-ADVANCED LUNG TUMORS

A Block-Matching Registration Algorithm for Localization of Locally-Advanced Lung Tumors

Scott Robertson, B.Sc., Elisabeth Weiss, M.D., Geoffrey D. Hugo, Ph.D.

Department of Radiation Oncology, Virginia Commonwealth University, Richmond, VA, 23298

Corresponding author

Geoffrey D. Hugo, Ph.D.
Department of Radiation Oncology
Virginia Commonwealth University
401 College Street
PO Box 980058
Richmond, VA 23298
Phone: 804-628-3457
Fax: 804-628-0271
E-mail: gdhugo@vcu.edu

Conflicts of interest

None of the authors has any actual or potential conflicts of interest.

ABSTRACT

Purpose: To implement and evaluate a block-matching registration (BMR) algorithm for locally-advanced lung tumor localization during image-guided radiotherapy.

Methods: Small (1 cm^3), non-overlapping image sub-volumes (“blocks”) were automatically placed on the planning image throughout the entire tumor surface using a measure of the gradient. Blocks were independently and automatically registered to the on-treatment image using a rigid transform. A multi-resolution strategy was implemented for improved speed and accuracy. At each resolution, multiple potential displacement vectors were initially permitted for each block. Then, after all blocks were registered, the final set of displacement vectors (one per block) was iteratively determined to maximize the local displacement consistency across immediately neighboring blocks. Finally, the optimal rigid transform for the on-treatment image was extracted using a Procrustes analysis, providing the couch shift for patient setup correction. This algorithm was evaluated for 18 locally-advanced lung cancer patients, each with 4 to 7 weekly on-treatment CT scans having physician-delineated gross tumor volumes (GTV). Volume overlap and radial border error (RBE) were calculated relative to the nominal physician-identified targets to establish residual error after registration.

Results: Implementation of multi-resolution registration improved block matching accuracy by 39%. By also permitting multiple potential displacements per block, initial errors were reduced by 65%. After BMR with the final implementation, left-right, anterior-posterior, and superior-inferior systematic RBE were 3.2, 2.4, and 4.4 mm respectively, with random RBE of 2.4, 2.1, and 2.7 mm. Required margins included both localization and delineation uncertainties and ranged from 5.0 to 11.7 mm, an average of 40% less than required for bony alignment.

Conclusions: BMR is a promising approach for automatic lung tumor localization. Further evaluation is warranted to assess the accuracy and robustness of BMR against other potential localization strategies.

Key words

Non-small-cell lung cancer, image registration, image-guided radiation therapy

I. INTRODUCTION

Online image guidance is an established and powerful tool for reducing geometric uncertainties in radiotherapy.[1] For example, inter-fractional errors resulting from patient setup variability are routinely corrected by on-treatment imaging immediately prior to each fraction.[2,3] Using volumetric imaging, direct visualization of primary tumors has enabled accurate and robust localization, particularly for lung tumors. Precision in patient setup is essential for modern treatment techniques that utilize narrow margins, steep dose gradients, and hypofractionated treatment regimens.

Direct localization of primary lung tumors is possible using both manual[4,5] and automatic[6–8] registration techniques. However, these approaches predominantly apply to stereotactic body radiation therapy (SBRT), where targets are generally small and well- Furthermore, with treatments lasting only 1 to 2 weeks, changes in pathology and surrounding anatomy are generally limited,[9] resulting in straightforward target localization. This is not the case for locally-advanced lung tumors, where tumor shrinkage over time and pulmonary conditions such as atelectasis or pleural effusion introduce substantial geometric variability throughout treatment.[10] These pathoanatomical changes present a major challenge to manual and automatic rigid registration algorithms[11,12] as well as commonly-available deformable registration algorithms.[13] A more robust registration technique is needed to improve the reliability of target localization for locally-advanced lung cancer patients.

The current study explores the feasibility of an automatic block-matching registration (BMR) algorithm as an alternative for improved lung tumor localization. This registration technique is carried out in three subsequent steps.[14,15] First, small image sub-volumes, termed "blocks", are identified and distributed on the planning CT to prioritize the registration of distinct tumor features. Each block is then independently registered to the on-treatment image using an automatic rigid transform. Finally, the displacement vectors from each separate block registration are reduced to a global registration of the on-treatment image, representing a couch shift for patient setup corrections. This registration strategy offers several key advantages to its novel application of target localization. Because this algorithm relies on the rigid alignment of many small image blocks, BMR is expected to execute as quickly as rigid registration of the entire target volume and faster than rigid registration of the entire on-treatment image.[16,17] Furthermore, because each block is registered independently, complex deformations such as shearing and tissue topology changes can be recovered. Lastly, the set of block displacement vectors can be regularized or filtered to reduce the impact of mis-registrations on the final image alignment.[18–20]

The purpose of this study is to implement and evaluate a block-matching registration algorithm specifically for the localization of locally-advanced lung tumors. The accuracy and robustness of block-matching is assessed for several different BMR implementations, including a new algorithm based on the identification of multiple candidate registrations for each individual block.

II. METHODS

The block-matching registration algorithm in this study was implemented based on an existing framework for physics-based non-rigid registration.[15] Advantages of this algorithm include parallel execution, block placement using both image intensity features and a binary mask, and an open source implementation as part of the Insight Segmentation and Registration Toolkit (ITK, version 4.2.0). The following sections describe the developments tailoring this algorithm to the specific purpose of lung tumor localization.

II.A. Algorithm implementation

II.A.1. Block placement

As an important requirement for reliable target localization, the surface of the on-treatment target must be well-aligned with (or, in the case of shrinking targets, entirely within) the surface of the planning target. Surface alignment was prioritized by placing blocks in close proximity to existing target contours. Although this algorithm required target contours on the planning CT, this condition is easily met in the context of image-guided radiation therapy. Contours were converted to a binary image mask, which was then dilated by 2 mm to provide a larger region near the tumor surface in which optimal soft-tissue features could be identified. Blocks were then distributed such that the center voxel was contained within the dilated mask region. The resulting block distribution was intended to capture the high contrast gradients commonly observed between lung tumors and the surrounding lung parenchyma, increasing the potential accuracy of block registrations.

In general, smaller blocks may fail to reliably match corresponding intensity features between two images, whereas larger blocks may capture regions containing substantial deformations that complicate the local rigid registration.[21] Preliminary tests revealed a nominal block size of 1 cm^3 to balance these competing factors. The voxel size was 1.2 by 1.2 mm^2 axially with a slice thickness of 2.0 mm for images in this study. Blocks were first placed in the most distinct regions of the planning target surface, as determined by the minimum eigenvalue of the structure tensor reflecting the local intensity gradient.[22] A larger minimum gradient eigenvalue indicated that a given block was more likely to contain a distinct, corner-like structure. This provided a better predictor of block-matching accuracy than edge-based feature detectors such as gradient magnitude or local intensity variance. Blocks were then distributed without overlap in order of decreasing distinctiveness throughout the rest of the GTV surface. By covering the entire surface with blocks, the final registration effectively incorporated local changes occurring anywhere along the tumor surface.

II.A.2. Block registration

Each block was individually registered from the planning CT to a predefined window region in the on-treatment image. In initial tests, a search radius of 2.5 cm was necessary to capture the displacement of the tumor surface for all patients in the current study population. However, for more general clinical application, a search radius exceeding 3 to 4 cm may be necessary to account for target shape and volume variability and positional uncertainties (e.g., initial setup errors, respiratory motion, etc.)[23] Registrations were performed using an exhaustive search over all possible translations within the window region. Rotations were not included for efficiency purposes. Block similarity between planning and on-treatment images was computed using the correlation ratio.

Initial data analysis revealed that large block displacements were correlated with large block mis-registrations. To reduce the impact of these large errors, a multi-resolution pyramid registration scheme was employed. Sequential registrations were performed for images down-sampled by factors of 4, 2, and 1, with block diameters of 4 cm, 2 cm, and 1 cm respectively. Because of down-sampling, blocks contained the same number of voxels at each physical dimension. The window region spanned 8 cm, 4 cm, and 2 cm respectively in the on-treatment image.

After all blocks were registered at a given resolution, the resulting displacement vectors were regularized using a median filter.[18] The median displacement was computed separately for each Cartesian axis within small neighborhoods of immediately adjacent blocks. Specifically, the neighborhood $\mathcal{N}(b_i)$ for the block centered at point b_i was defined to include all blocks centered at points less than twice the block diameter from b_i:

$$\mathcal{N}(b_i) = \{b_j \mid \|b_j - b_i\| < 2 \cdot BlockDiameter\}.$$

This definition was necessary to account for the non-uniform block distribution employed in this study. After regularization, the final displacements were used to initialize the position of the window region for subsequent registrations at finer resolutions.

A second major development in the current BMR algorithm addressed blocks that were registered with a high similarity value, but that were not matched to their expected location near the tumor surface. These blocks often contained degenerate features such as edges or planes that matched at multiple locations within the window region. In many cases, it was possible to recover the expected displacement by searching for “near-optimal” registrations in a strategy referred to as multiple candidate registration (MCR). During the exhaustive search over all possible translations, a similarity map of the correlation ratios was generated, from which a set of candidate registrations was extracted. Starting with the maximum correlation ratio, additional candidate registrations were identified in order of decreasing correlation ratio according to the following constraints:

i. the correlation ratio was at least 95% of the true maximum,

ii. the correlation ratio was greater than 0.75, and

iii. the distance between candidate registrations was greater than the block radius.

The first constraint ensured that only near-optimal displacements were considered as potential candidate registrations. The second constraint was heuristically based on preliminary data that associated lower correlation ratios with less accurate block registrations. Finally, the third constraint limited the identification of degenerate block registrations along smooth, planar tissue surfaces. After all blocks were registered, a post-processing step was used to extract the single most likely displacement for each block. Assuming that the registration of immediately adjacent blocks on the tumor surface should demonstrate a high degree of consistency, the final set of block registrations (one per block) was iteratively selected to minimize the variance of the displacement vectors for all local block neighborhoods. Figure 2 demonstrates an example of block-matching with MCR. For pyramid registrations using the MCR method, the median filter was always applied to the final set of displacements from MCR (Figure 2, right panel).

II.A.3. Target localization

The sparsely sampled displacement vector field provided an estimate of the true underlying changes in pathology and local anatomy between the planning and on-treatment images. To compute the optimal rigid transform between images to be used for setup correction, a Procrustes analysis was implemented. Briefly, translational corrections were given by the mean of the displacement vectors in each cardinal direction. To determine rotational corrections, it was first necessary to compute the covariance matrix between the center coordinates of blocks from the initial and registered distributions. Singular value decomposition of the covariance matrix yielded a rotation matrix that optimally oriented the two block distributions. This final, global transform was applied to on-treatment images for analysis.

II.B. Analysis

According to a protocol approved by the local institutional review board, weekly breath-hold CT scans were acquired for 18 locally-advanced lung cancer patients throughout 4 to 7 weeks of conventionally fractionated radiotherapy.[10,24] One patient presented with two tumors that were registered and analyzed separately. The primary gross tumor volume (GTV) was delineated by a physician on each image. Prior to automatic block-matching registration, manual bony-anatomy registrations were performed to align all weekly CTs with the planning CT.

II.B.1. Block registration errors

The implementation and development of the current BMR algorithm was assessed using the week 4 CT for a randomly-selected subset of 12 patients. The week 4 CT was selected (1) for consistency, as not all patients had images acquired after this week of treatment, and (2) to provide an intermediate degree of variability in tumor shape and volume and in pathoanatomical conditions such as atelectasis or pleural effusion.[12]

Because blocks were distributed along the surface of the primary tumor, physician contours were used to compute block registration errors. No point-to-point correspondence existed between contoured targets from the planning and weekly CTs, so an in-house deformable mesh registration tool was used to generate the nominal transform between target surfaces.[25] Block registration errors were then computed as the difference between these nominal displacements and the observed block displacements. Large discrepancies between block-matching and deformable mesh registration were a strong indicator of poor block registration quality. In contrast, better agreement between these two registration techniques indicated a more reliable registration of blocks between the target surfaces.

Contouring variability inherently limited the accuracy of deformable mesh registration as a validation tool for BMR. To circumvent this problem, BMR was also evaluated for a set of artificially-deformed images. These images were previously generated for the current study sub-population[26] using the small deformation, inverse consistent linear elastic (SICLE) algorithm.[27] The deformed images thus provided a reasonable approximation of the actual internal changes for these patients. Block registration errors were computed in this case as the difference between the known deformation and the observed block displacement. Unlike the block registration errors defined for weekly image registrations, these errors were not affected by delineation uncertainties.

II.B.2. Target registration errors

Using the multi-resolution pyramid technique with multiple candidate registrations, the final block-matching algorithm was used to register all 18 patients and all available weekly images, for a total of 93 registrations. Target registration errors were assessed by computing radial border errors (RBE) and volume overlap. In both cases, the physician-delineated target volume on the planning CT was compared with the physician-delineated target from the registered on-treatment image. Target borders were defined by the lower and upper corners of the bounding box enclosing the target volume. Positive RBE were then defined as any shift of the on-treatment target borders radially outward from the respective borders of the planning target. Likewise, negative RBE were scored for inward shifts of the on-treatment target borders. The group mean (G) and the systematic (Σ) and random (σ) variability were computed separately in each cardinal direction (left-right [LR], anterior-posterior [AP], and superior-inferior [SI]), from which the required margins were computed.[28] Finally, volume overlap was computed as the intersection of planning and registered target volumes divided by the registered target volume.

Because patient setup uncertainties may be influenced by pathoanatomical conditions (PAC) such as atelectasis or pleural effusion,[10] border errors and volume overlap were recomputed separately for patient sub-populations with and without the presence of PAC. Patients with these conditions were referred to as the PAC-positive group (N=7; 35 registrations), while patients without these conditions were referred to as the PAC-negative group (N=11; 58 registrations).

III. RESULTS

III.A. Block registration accuracy

Figures 3, 4, and 5 highlight the accuracy of block-matching for 12 of the 18 patients in the current study population. These figures show patients listed in order of increasing tumor size. For patients 1 – 7, the GTV ranged from 0.6 to 46.6 cm^3 initially and from 0.6 to 32.0 cm^3 by the fourth week of treatment. These targets regressed by an average of 35% (range: 0% to 64%) during this period. For patients 8 – 12, the initial GTV ranged from 58.3 to 241.9 cm^3, with the week 4 GTV ranging from 35.6 to 181.5 cm^3. Mean target volume regression was 37% (range: 25% to 45%). Figure 5 provides the number of blocks included in each registration, which ranged from 13 to 181. Two PAC-positive patients were included in this sub-population, one of which (patient 2) had a pleural effusion that progressed throughout treatment and another (patient 8) with atelectasis that resolved by the fourth week of treatment.

Figure 3 shows the average magnitude of RBE after registration of the artificially deformed images. The initial BMR implementation resulted in mean block displacement errors of 4.1 mm for all patients (Σ = 4.4 mm, σ = 7.8 mm). The MCR modification reduced group mean errors to 2.5 mm (Σ = 3.0 mm, σ = 4.7 mm). With pyramid registration and median filtering, group mean errors were 1.7 mm (Σ = 1.2 mm, σ = 1.8 mm) without MCR and 1.7 mm (Σ = 0.8 mm, σ = 1.3 mm) with MCR.

Figure 4 shows the magnitude of discrepancies resulting from comparison between block-matching registration of weekly CTs and deformable mesh registration. The initial BMR implementation resulted in mean block displacement errors of 11.5 mm (Σ = 4.9 mm, σ = 10.0 mm). Using MCR, mean errors were reduced to 7.6 mm (Σ = 4.0 mm, σ = 6.5 mm). With pyramid registration and median filtering, errors averaged 5.2 mm (Σ = 2.2 mm, σ = 3.1 mm) without MCR and 4.8 mm (Σ = 1.9 mm, σ = 2.6 mm) with MCR.

Figure 5 demonstrates the impact of MCR by only considering blocks that were modified by this regularization strategy. The top panel illustrates improvements relative to the initial BMR algorithm, whereas the bottom panel includes pyramid registration. According to the top panel, between 7% and 62% of block displacements were modified by the MCR technique. For these blocks, separate application of median filtering and MCR resulted in respective block registration errors of 7.9 ± 4.9 mm and 7.8 ± 4.9 mm. The combined approach of MCR with median filtering reduced registration errors to 6.2 ± 3.5 mm. In the bottom panel, one patient did not have any block displacements modified by MCR. The remaining patients had between 4% and 57% of block displacements modified using the MCR technique. For these blocks, the smallest registration errors of 6.2 ± 3.5 mm were again provided by the combined approach of MCR with median filtering.

III.B. Target localization accuracy

Table 1 lists the border errors for bony anatomy alignment and block-matching registration. The negative group means indicated that target borders were predominantly shifted inward, and that tumor volumes generally regressed throughout treatment for the study population. Compared to bony alignment, BMR reduced systematic and random border errors by 1.2 to 2.4 mm and 0.5 to 0.9 mm respectively for all patients. For PAC-negative patients, BMR reduced systematic and random border errors by 0.4 to 1.1 mm and 0.3 to 0.8 mm respectively. Corresponding error reductions for PAC-positive patients were 1.5 to 4.0 mm and 0.8 to 1.1 mm respectively. These reductions translated to improvements in the required margins ranging from 3.5 to 6.9 mm (all patients), 1.9 to 3.1 mm (PAC-negative), and 4.4 to 11.4 mm (PAC-positive).

Figure 6 shows the volume overlap of targets after bony alignment and block-matching registration. BMR improved the overall volume overlap of PAC-negative patients by an average of 0.10 ± 0.12 (range: -0.03 to 0.45), with 88% of registrations resulting in better overlap. Of these registrations, initial VO of 0.81 ± 0.14 was increased to 0.93± 0.07. The remaining 12% of registrations reduced the VO by an average of 1% from 0.88 ± 0.06 to 0.87 ± 0.06. For PAC-positive patients, the volume overlap improved by an average of 0.20 ± 0.32 (range: -0.19 to 0.98). Bony alignment resulted in no target overlap for three weeks of treatment for the same patient. Block-matching improved the volume overlap in 21 of 33 registrations from an initial average of 0.59 ± 0.31 to 0.94 ± 0.05. The 12 registrations with reduced volume overlap changed from 0.89 ± 0.08 to 0.83 ± 0.12.

IV. DISCUSSION

A block-matching registration algorithm has been implemented to improve the localization of locally-advanced lung tumors. Eventually, such an algorithm could be used to automate registration of on-treatment imaging for image-guided setup correction. By concentrating blocks near the surface of tumors, this algorithm prioritizes surface alignment as an important requirement for target localization, and it exploits the high-contrast gradients commonly observed between lung tumors and the surrounding lung tissue. Accurate and robust block-matching was possible using multi-resolution pyramid registration in conjunction with the multiple-candidate registrations technique. This led to reductions in systematic and random border variability and improved volume overlaps for both PAC-positive and PAC-negative patient sub-populations.

The accuracy of block registrations was evaluated using both weekly on-treatment images and artificially deformed images. Because the deformed images were generated directly from the weekly CTs, they provided a reasonable approximation of the pathological and anatomical changes demonstrated by these patients. Comparison of block displacement vectors with the expected transform from deformable image registration yielded an error metric affected solely by inaccuracies in the block-matching process. However, because deformed images may not represent the full extent of irregular target volume changes (e.g., abrupt changes in the tumor surface or dissolving of the tumor interior), these errors may have potentially underestimated block-matching accuracy for the weekly patient images. In general, any changes between planning and weekly CTs that could not be modeled by pure deformation would likely increase the block-matching errors shown in Figure 3.

Assessment of block-matching accuracy was not as straightforward for weekly CT registrations, as no ground truth existed for local deformations along the tumor surface. To establish an estimate of block-matching accuracy, deformable surface-mesh registration was used to orient the physician-delineated targets from planning and weekly CTs. Previous work has demonstrated this method to be accurate to within 2 to 3 millimeters at the tumor surface. The block registration errors in Figure 4 include uncertainties in deformable mesh registration and target delineation, implying that uncertainties arising solely from block-matching may be less than the errors actually reported in this case. Therefore, these results are considered an upper bound on the true accuracy of BMR at the tumor surface. Note that block-matching errors do not directly correspond to projected errors in target localization. Rather, these measures tended to be randomly distributed, which helped to reduce the impact of block-matching errors on the final target registration.

Two strategies were implemented in this work to improve block registration accuracy. First, pyramid registration was employed to better capture both coarse and fine details in the registration. Down-sampling by a factor of 4 enabled an initial 8 cm window region in the moving image, sufficient for the registration of images with target volume regression, respiratory excursion, or slight initial misalignment. Pyramid registration also provided the opportunity for intermediate data regularization. Initial block matching errors could thus be corrected before they were propagated to subsequent registrations at finer resolutions.

The second improvement involved the detection of multiple candidate registrations as part of the block-matching process. This enabled the algorithm to correct large block registration errors by searching for near-optimal displacements (with respect to the correlation ratio) that were more consistent with other neighboring block registrations. Although block mis-registrations were not guaranteed to be corrected by this method, results demonstrated that the new block displacements were on average more consistent with changes in the target surface, as determined by deformable mesh registration. Despite these improvements, Figure 3 and Figure 4 both include cases where the overall accuracy becomes worse as a result of pyramid registration with MCR. This was attributed to regularization with the median filter, which provided a somewhat variable degree of improvement on the final registration results.

The final block-matching algorithm led to substantial gains in target localization compared to bony anatomy alignment. However, required margins still ranged from 5.0 to 11.7 mm after block-matching registration. These relatively large margins resulted from the combined effects of localization error, delineation uncertainty, and target volume variability (i.e., changes in tumor shape and size). This implies that even with high-quality target registration, purely rigid shifts have a limited ability to correct for all sources of uncertainty throughout treatment. To further reduce margins, strategies to manage target volume variability (such as adaptive radiation therapy) and delineation error are required.

Yeung *et al*. conducted a similar study for lung cancer patients also receiving conventionally fractionated radiotherapy.[29] In their retrospective review, automatic rigid registration of the spine was compared against automatic soft-tissue-based registration of the planning target volume. Variations in the relative treatment couch shifts were used to formulate margins, which were shown to decrease by 5 to 14 mm after direct tumor registration. However, these margins did not account for potential residual errors in the tumor registration. More modest gains ranged from 3.5 to 6.9 mm for patients in the current study, likely because target registration errors were directly assessed for both registrations.

Larger gains were demonstrated for the PAC-positive subgroup. PAC-positive patients demonstrated larger variations between planning and on-treatment CTs due to changes in tumor volume, atelectasis, and pleural effusion.[10] This led to larger initial target registration errors from bony anatomy alignment and larger potential corrections after BMR. Block-matching led to systematic and random border errors with an average improvement of 46% and 28%, respectively, for the PAC-positive patients. This resulted in a 52% overall decrease in margin size.

The current study sought to establish block-matching as an accurate and robust registration technique for locally-advanced lung tumors. To date, this has been demonstrated using CT-CT registration for images acquired with an active breath-hold protocol. Further evaluation of this tool for CT-CBCT registration is pending. The correlation ratio similarity metric is suitable for multi-modality registration and should not impact the results of CT-CBCT registrations. The presence of additional noise, potential image artifacts, and respiratory motion in CBCT images may all impact the accuracy reported in this study. However, BMR is anticipated to be robust against these complications due to the independent registration of each image sub-volume. Mis-registration of a reasonably small number of blocks can be corrected through a combination of pyramid registration, the multiple candidate registrations technique, and median filtering, leading to robust target localization and reduced patient setup uncertainties.

Future work will also consider the simultaneous registration of multiple treatment targets, as direct tumor alignment may result in poor localization of other lesions such as metastatic lymph nodes.[30] Furthermore, direct tumor alignment may increase the dose delivered to nearby risk structures.[7] Because block-matching provides local displacements of the entire tumor surface, it may be possible to adapt the final tumor registration in order to better localize other lesions or better spare risk structures.

V. CONCLUSION

A block-matching registration algorithm has been implemented specifically for the localization of locally-advanced lung tumors. Through a combination of regularized pyramid registration and a new multiple candidate registrations strategy, substantial improvements were demonstrated relative to an initial bony anatomy alignment in systematic and random border errors, margin sizes, and target volume overlap. Accurate and robust registrations were observed for patients both with and without the presence of pathoanatomical conditions such as atelectasis or pleural effusion. Future work is warranted to evaluate block-matching against other potential localization strategies for routine image-guidance.

ACKNOWLEDGEMENTS

This work was partially supported by NIH R01CA166119. It relied on the Insight Segmentation and Registration Toolkit (ITK), an open source software developed as an initiative of the U.S. National Library of Medicine and available at www.itk.org.

TABLES AND FIGURES

Figure 1. Workflow for block-matching registration. Left: Blocks are placed on the reference (planning) image at the surface of the initial gross tumor volume (red contour). Center: Each block is independently registered to the moving image using an exhaustive search over all translations in a predefined window. The blocks in this center image show the registered location of the blocks from the left image; two additional blocks registered into the current image slice. The weekly physician contour is provided in yellow for reference. Right: The resulting transform vectors are aggregated to obtain the global image registration. This corresponds to the couch shift required for patient setup correction.

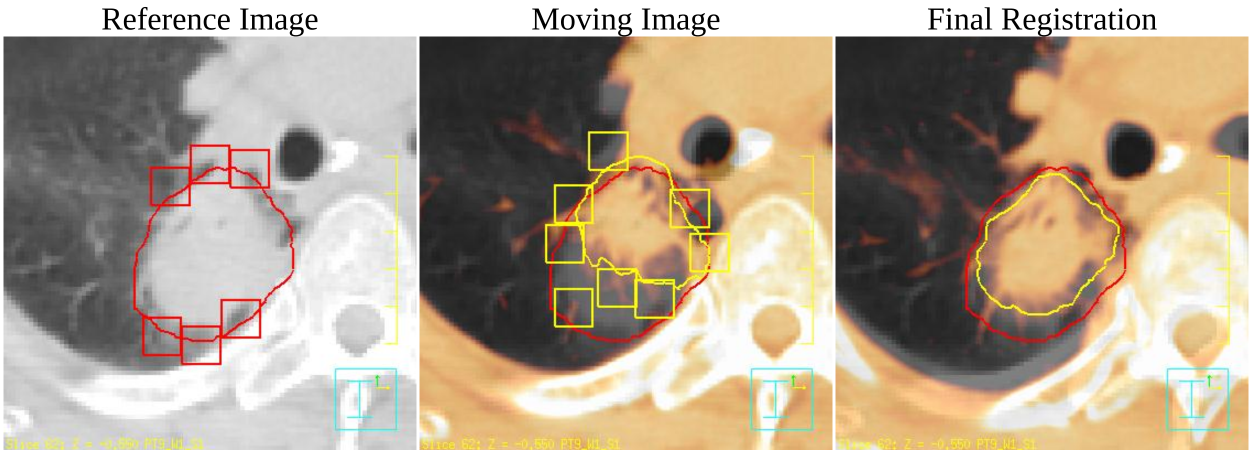

Reference Image

Moving Image

Final Registration

Figure 2. Block-matching with multiple candidate registrations. The initial block displacements (left) correspond to registrations with the maximum correlation ratio. However, by also considering *near*-optimal block displacements (center), it becomes possible to extract a set of displacements more consistent with registration of the tumor surface (right).

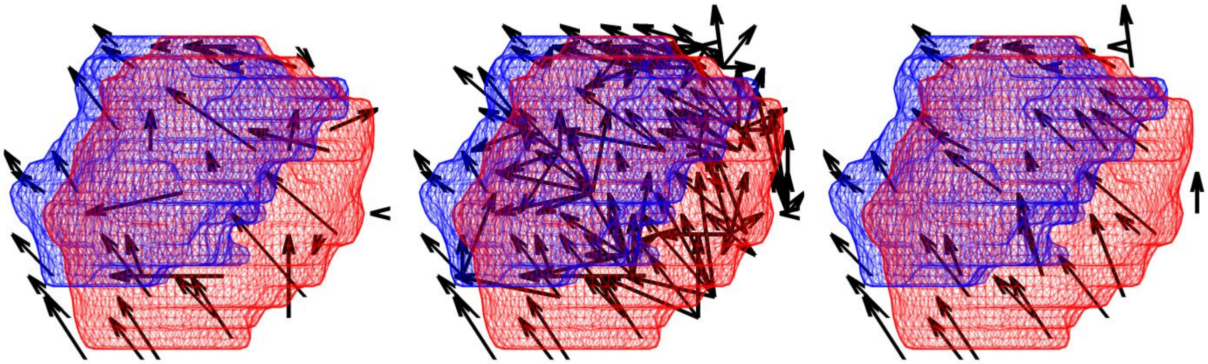

Figure 3. Magnitude of block matching errors from registration of artificially deformed images. Results are shown for the initial BMR implementation, multiple candidate registrations (MCR), multi-resolution pyramid registration, and the combined effect of MCR and pyramid registration. The final group (“All”) represents the mean and random error for all registrations.

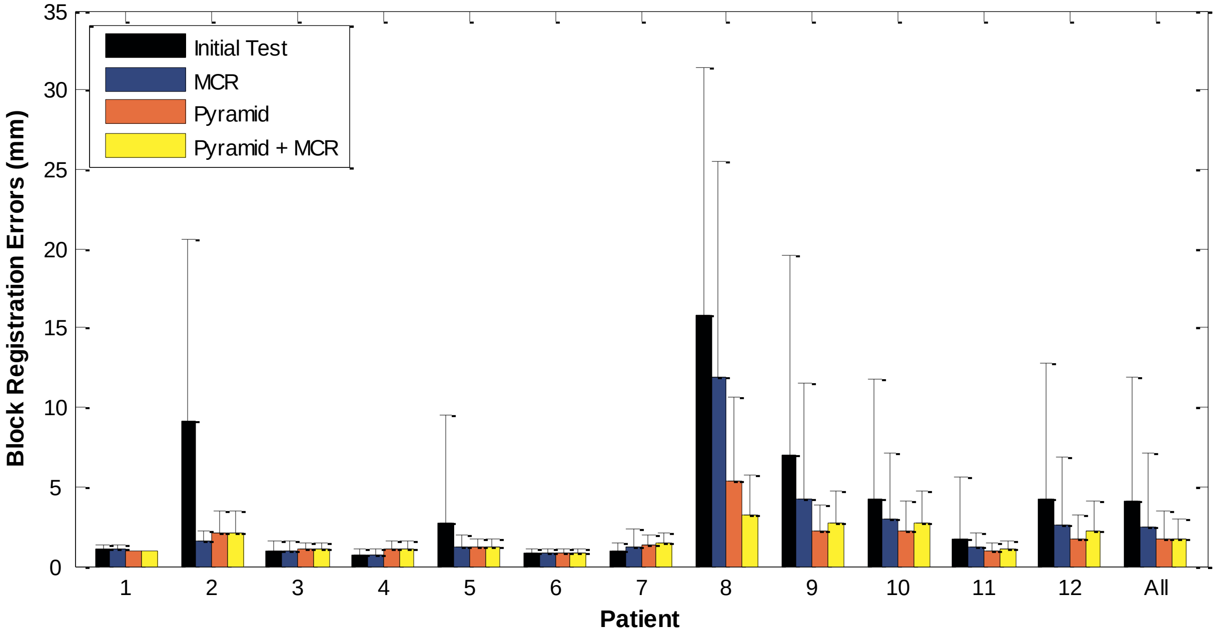

Figure 4. Magnitude of discrepancies between block-matching registration of weekly CT images and deformable mesh registration (annotations according to Figure 3.)

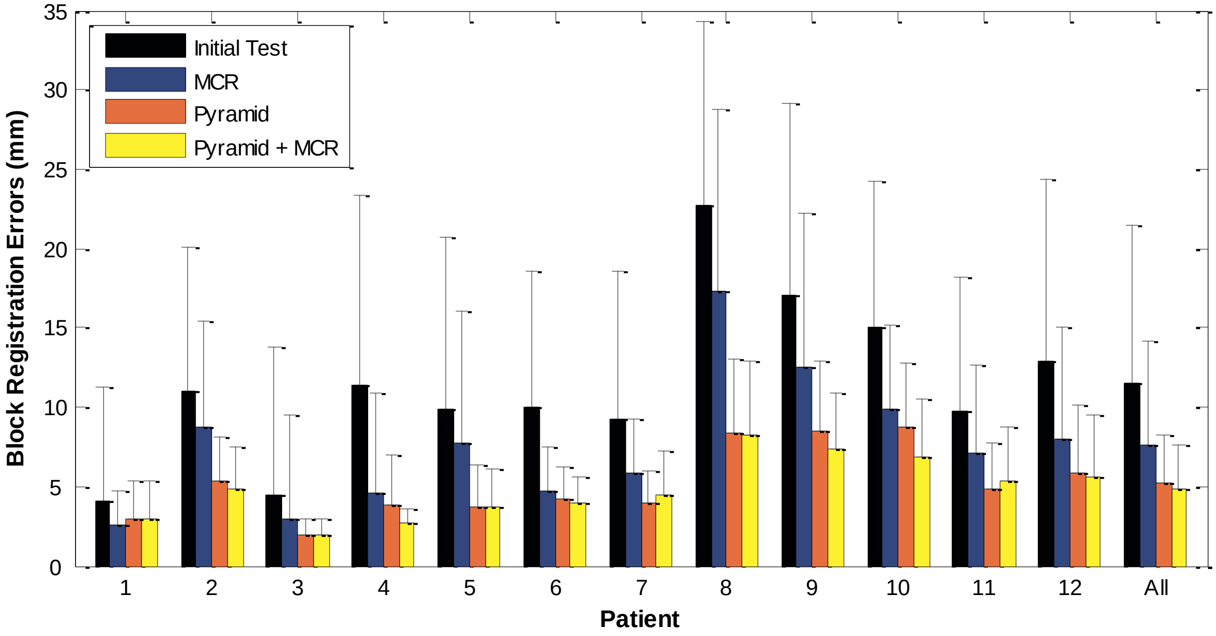

Figure 5. Registration accuracy for the subset of block displacements that were modified by the multiple candidate registrations (MCR) strategy (annotations according to Figure 3). The fraction of modified block displacements is provided beneath each patient index. All results correspond to registration of weekly images.

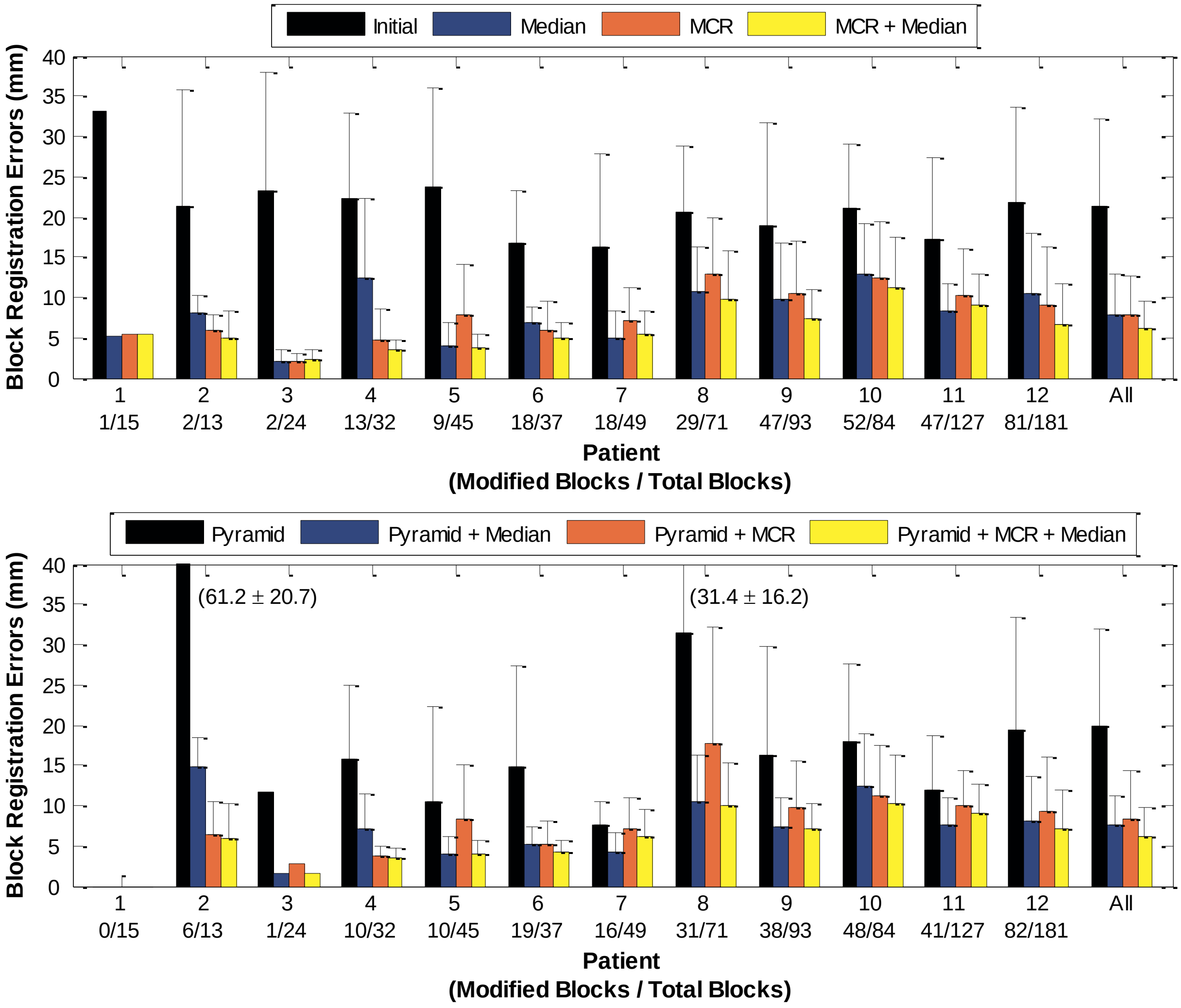

Figure 6. Cumulative histograms of the volume overlap between planned and treatment GTV after bony anatomy alignment (Bony) and block-matching registration (BMR). Results are shown for patients stratified according to the presence of pathoanatomical conditions (PAC) such as atelectasis and pleural effusion.

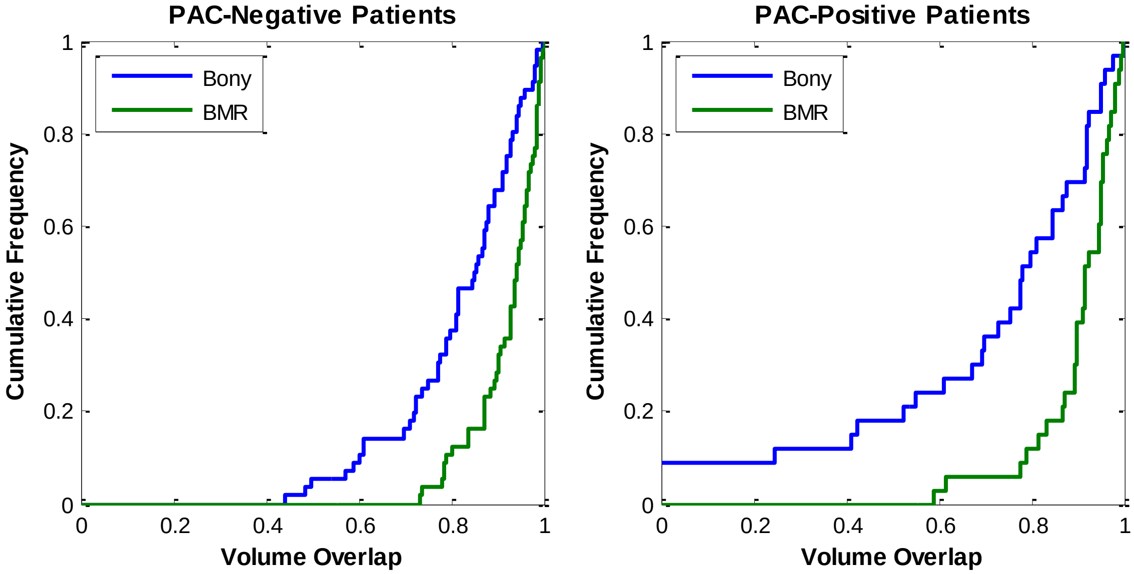

Table 1. Mean (G), systematic (Σ), and random (σ) border displacement errors (in millimeters), along with required margins (M) in the left-right (LR), anterior-posterior (AP), and superior-inferior (SI) directions. Results are shown for all patients, for the sub-group without pathoanatomical conditions (PAC-negative), and for the sub-group with pathoanatomical conditions (PAC-positive).

	All Patients			PAC-Negative			PAC-Positive		
	LR	AP	SI	LR	AP	SI	LR	AP	SI
Bony Alignment									
G	-2.2	-2.0	-1.2	-2.1	-1.7	-0.6	-2.3	-2.3	-2.1
Σ	4.4	4.8	6.1	4.7	3.3	4.7	4.0	6.6	7.7
σ	2.9	2.9	3.6	2.7	2.4	3.3	3.1	3.6	4.0
M	10.7	11.9	16.7	11.2	7.7	13.5	9.7	16.9	20.5
Block-Matching Registration									
G	-2.2	-1.9	-1.0	-2.2	-1.6	-0.5	-2.1	-2.4	-1.7
Σ	3.2	2.4	4.4	3.6	2.2	4.3	2.5	2.6	4.6
σ	2.4	2.1	2.7	2.4	1.8	2.5	2.3	2.5	2.9
M	7.2	5.0	11.7	8.2	4.6	11.6	5.3	5.5	11.5

REFERENCES

[1]M. van Herk, “Different styles of image-guided radiotherapy,” Semin. Radiat. Oncol. **17**, 258–267 (2007).

[2]G. R. Borst, J.-J. Sonke, A. Betgen, P. Remeijer, M. van Herk, and J. V. Lebesque, “Kilo-voltage cone-beam computed tomography setup measurements for lung cancer patients; First clinical results and comparison with electronic portal-imaging device,” Int. J. Radiat. Oncol., Biol., Phys. **68**, 555–561 (2007).

[3]T. G. Purdie, J.-P. Bissonnette, K. Franks, A. Bezjak, D. Payne, F. Sie, M. B. Sharpe, and D. A. Jaffray, “Cone-beam computed tomography for on-line image guidance of lung stereotactic radiotherapy: localization, verification, and intrafraction tumor position,” Int. J. Radiat. Oncol., Biol., Phys. **68**, 243–252 (2007).

[4]J.-P. Bissonnette, T. G. Purdie, J. A. Higgins, W. Li, and A. Bezjak, “Cone-beam computed tomographic image guidance for lung cancer radiation therapy,” Int. J. Radiat. Oncol., Biol., Phys. **73**, 927–934 (2009).

[5]L. Wang, S. Feigenberg, J. Fan, L. Jin, A. Turaka, L. Chen, and C.-M. C. Ma, “Target Repositional Accuracy and PTV Margin Verification using Three-dimensional Cone-Beam Computed Tomography (CBCT) in Stereotactic Body Radiotherapy (SBRT) of Lung Cancers,” J. Appl. Clin. Med. Phys. **13**, (2012).

[6]I. S. Grills, D. L. Fitch, N. S. Goldstein, D. Yan, G. W. Chmielewski, R. J. Welsh, and L. L. Kestin, “Clinicopathologic analysis of microscopic extension in lung adenocarcinoma: defining clinical target volume for radiotherapy,” Int. J. Radiat. Oncol., Biol., Phys. **69**, 334–341 (2007).

[7]A. P. Galerani *et al.*, “Dosimetric impact of online correction via cone-beam CT-based image guidance for stereotactic lung radiotherapy,” Int. J. Radiat. Oncol., Biol., Phys. **78**, 1571–1578 (2010).

[8]M. Josipovic, G. F. Persson, Á. Logadottir, B. Smulders, G. Westmann, and J. P. Bangsgaard, “Translational and rotational intra- and inter-fractional errors in patient and target position during a short course of frameless stereotactic body radiotherapy,” Acta Oncol. **51**, 610–617 (2012).

[9]M. L. Siker, W. A. Tomé, and M. P. Mehta, “Tumor volume changes on serial imaging with megavoltage CT for non-small-cell lung cancer during intensity-modulated radiotherapy: how reliable, consistent, and meaningful is the effect?” Int. J. Radiat. Oncol., Biol., Phys. **66**, 135–141 (2006).

[10]E. Weiss, S. P. Robertson, N. Mukhopadhyay, and G. D. Hugo, “Tumor, lymph node, and lymph node-to-tumor displacements over a radiotherapy series: Analysis of interfraction and intrafraction variations using active breathing control (ABC) in lung cancer,” Int. J. Radiat. Oncol., Biol., Phys. **82**, e639–e645 (2012).

[11] J. Higgins, A. Bezjak, K. Franks, L. W. Le, B. C. Cho, D. Payne, and J.-P. Bissonnette, “Comparison of spine, carina, and tumor as registration landmarks for volumetric image-guided lung radiotherapy,” Int. J. Radiat. Oncol., Biol., Phys. **73**, 1404–1413 (2009).

[12] S. P. Robertson, E. Weiss, and G. D. Hugo, “Localization accuracy from automatic and semi-automatic rigid registration of locally-advanced lung cancer targets during image-guided radiation therapy,” Med. Phys. **39**, 330–341 (2011).

[13] M. Guckenberger, K. Baier, A. Richter, J. Wilbert, and M. Flentje, “Evolution of surface-based deformable image registration for adaptive radiotherapy of non-small cell lung cancer (NSCLC),” Radiat. Oncol. **4**, 68 (2009).

[14] S. Ourselin, A. Roche, S. Prima, and N. Ayache, “Block matching: A general framework to improve robustness of rigid registration of medical images,” in *Proceedings of MICCAI*, 2000, pp. 557–566.

[15] Y. Liu, A. Kot, F. Drakopoulos, A. Enquobahrie, O. Clatz, and N. Chrisochoides, “An ITK implementation of physics-based non-rigid registration method,” Insight J., (2012).

[16] U. Malsch, C. Thieke, P. E. Huber, and R. Bendl, “An enhanced block matching algorithm for fast elastic registration in adaptive radiotherapy,” Phys. Med. Biol. **51**, 4789–4806 (2006).

[17] A. Wang, B. Disher, J. Battista, and T. Peters, “Use of a graphics processor (GPU) for high-performance deformable registration of cone beam (kV) and megavoltage (MV) CT images,” Med. Phys. **37**, 3909 (2010).

[18] Y. H. Lau, M. Braun, and B. F. Hutton, “Non-rigid image registration using a median-filtered coarse-to-fine displacement field and a symmetric correlation ratio,” Phys. Med. Biol. **46**, 1297–1319 (2001).

[19] E. Suárez, C.-F. Westin, E. Rovaris, and J. Ruiz-Alzola, “Nonrigid Registration Using Regularized Matching Weighted by Local Structure,” in *Proceedings of MICCAI*, 2002, pp. 581–589.

[20] M. Bhattacharjee, A. Pitiot, A. Roche, D. Dormont, and E. Bardinet, “Anatomy-preserving nonlinear registration of deep brain ROIs using confidence-based block-matching,” in *Proceedings of MICCAI*, 2008, pp. 956–963.

[21] P. Rösch, T. Netsch, M. Quist, G. P. Penney, D. L. G. Hill, and J. Weese, “Robust 3D deformation field estimation by template propagation,” in *Proceedings of MICCAI*, 2000, pp. 521–530.

[22] J. Shi and C. Tomasi, “Good features to track,” in *IEEE Computer Society Conference on Computer Vision and Pattern Recognition*, 1994, pp. 593–600.

[23] J.-J. Sonke and J. Belderbos, “Adaptive radiotherapy for lung cancer,” Semin. Radiat. Oncol. **20**, 94–106 (2010).

[24]C. K. Glide-Hurst, E. Gopan, and G. D. Hugo, “Anatomic and pathologic variability during radiotherapy for a hybrid active breath-hold gating technique,” Int. J. Radiat. Oncol., Biol., Phys. **77**, 910–917 (2010).

[25]S. P. Robertson, E. Weiss, and G. D. Hugo, “Deformable Mesh Registration for the Validation of Automatic Target Localization Algorithms,” Med. Phys., (2013).

[26]A. M. Badawi, E. Weiss, W. C. Sleeman IV, and G. D. Hugo, “Classifying geometric variability by dominant eigenmodes of deformation in regressing tumours during active breath-hold lung cancer radiotherapy,” Phys. Med. Biol. **57**, 395–413 (2012).

[27]G. E. Christensen, J. H. Song, W. Lu, I. El Naqa, and D. A. Low, “Tracking lung tissue motion and expansion/compression with inverse consistent image registration and spirometry,” Med. Phys. **34**, 2155 (2007).

[28]G. D. Hugo, E. Al Sulaimani, E. Weiss, and S. P. Robertson, “Evaluation of the Carina as a Surrogate for Daily Localization of Mediastinal Lymph Nodes during Radiation Therapy of Locally-Advanced Lung Cancer,” Pract. Radiat. Oncol., (submitted).

[29]A. R. Yeung, J. G. Li, W. Shi, H. E. Newlin, A. Chvetsov, C. Liu, J. R. Palta, and K. Olivier, “Tumor localization using cone-beam CT reduces setup margins in conventionally fractionated radiotherapy for lung tumors,” Int. J. Radiat. Oncol., Biol., Phys. **74**, 1100–1107 (2009).

[30]N. Mohammed, L. Kestin, I. Grills, C. Shah, C. Glide-Hurst, D. Yan, and D. Ionascu, “Comparison of IGRT registration strategies for optimal coverage of primary lung tumors and involved nodes based on multiple four-dimensional CT scans obtained throughout the radiotherapy course,” Int. J. Radiat. Oncol., Biol., Phys. **82**, 1541–1548 (2012).

APPENDIX IV

COMPARISON OF AUTOMATIC REGISTRATION ALGORITHMS FOR LOCALLY-ADVANCED LUNG TUMOR LOCALIZATION DURING IMAGE-GUIDED RADIOTHERAPY

Comparison of Automatic Registration Algorithms for Locally-Advanced Lung Tumor Localization during Image-Guided Radiotherapy

Scott Robertson, B.Sc., Salim Balik, Ph.D., Elisabeth Weiss, M.D., Geoffrey D. Hugo, Ph.D.

Department of Radiation Oncology, Virginia Commonwealth University, Richmond, VA, 23298

Corresponding author

Geoffrey D. Hugo, Ph.D.
Department of Radiation Oncology
Virginia Commonwealth University
401 College Street
PO Box 980058
Richmond, VA 23298
Phone: 804-628-3457
Fax: 804-628-0271
E-mail: gdhugo@vcu.edu

Conflicts of interest

None of the authors has any actual or potential conflicts of interest.

ABSTRACT

Purpose: To assess the accuracy of locally-advanced lung tumor localization resulting from automatic soft-tissue-based registration.

Methods: Four different registrations were evaluated in this study: rigid registration of the gross tumor volume (GTV), block-matching registration (BMR), deformable registration with the small deformation, inverse consistent linear elastic (SICLE) algorithm, and deformable registration with a diffeomorphic demons algorithm (Demons). For BMR, SICLE, and Demons, deformation vectors were extracted at the surface of the GTV from the planning CT. These vectors were used to compute the translations and rotations that best rigidly aligned the surface of the GTV from on-treatment images. For 16 non-small-cell lung cancer patients, the end-inspiration phases from a four-dimensional (4D) planning CT and 6 to 8 weekly 4D kilovoltage cone-beam CT images were registered. After registration, radial border errors were defined as outward displacements of the registered GTV surface relative to the planning GTV and were used to formulate margins to compensate for registration error. Volume overlap (VO) was defined as the intersection of planning and registered target volumes divided by the registered target volume.

Results: Bony anatomy alignment resulted in margins of 11.4 to 18.4 mm and a median VO of 0.73 (minimum: 0.24). All soft-tissue-based registrations provided significantly better VO than bony alignment ($p < 0.05$). BMR resulted in the most robust target localization with margins of 11.1 to 12.9 mm and a significantly greater VO than any other registration ($p < 0.05$; median: 0.83; minimum: 0.61). Required margins from rigid, SICLE, and Demons registrations ranged from 11.0 to 18.0 mm with median (minimum) VO of 0.77 (0.34), 0.80 (0.23), and 0.77 (0.25) respectively. A maximum VO of 0.99 was achieved for all registrations.

Conclusions: Automatic soft-tissue-based registration significantly improved VO for locally-advanced lung tumors, with block-matching registration being the most robust and accurate. Treatment margins also improved but remained relatively large, confirming that target localization alone cannot account for all sources of uncertainty in these patients.

Key words

Non-small-cell lung cancer, image registration, image-guided radiation therapy

I. INTRODUCTION

The accuracy of lung tumor localization during image-guided radiotherapy can be influenced by a number of different factors, especially for locally-advanced disease. Several studies have demonstrated the potential for large variations in tumor shape and volume,[1–3] with target volume regression exceeding 80% in extreme cases.[4] Other pathoanatomical conditions such as atelectasis and pleural effusion may also increase variability in tumor position relative to bony anatomy or neighboring soft-tissue landmarks.[3–5] Further complications arise for patients with multiple primary lesions or metastatic lymph nodes, where configurational changes between targets may limit the localization accuracy of each individual target.[6,7] All of these uncertainties require generous treatment margins to compensate. This leads to larger target volumes and a corresponding increase in the risk of normal tissue toxicities, limiting the potential tumor dose.[8] Treatment-related uncertainties must therefore be carefully controlled to facilitate safe dose escalation for improved local tumor control.[9]

Image-guided radiation therapy is a powerful tool for mitigating many of these uncertainties. For example, imaging immediately prior to each treatment fraction has enabled highly accurate patient setup to reduce inter-fractional variability. Higgins *et al*. demonstrated that registration of tumor surrogates including the spine and carina can be used for efficient and reproducible patient setup.[10] Mohammed *et al*. further demonstrate that patient setup based on bony anatomy alignment provides reasonable simultaneous localization of the primary tumor and involved lymph nodes, with only slight improvements offered by direct simultaneous registration of the tumor and nodes.[7] However, tumor surrogates do not always reflect potential changes in target position or configuration.[5] Direct target registration should therefore provide more reliable localization throughout treatment. Because manual target registration is prone to inter- and intra-observer variability,[10] automatic target registration provides the most attractive solution for robust tumor localization.

The purpose of this study is to compare the accuracy of lung tumor localization resulting from several soft-tissue-based automatic registration algorithms. Rigid tumor registration is included as a common approach to online localization, providing efficient and reasonably accurate alignment of targets with slight to moderate changes in shape and size.[6] Deformable image registration is also assessed to address more substantial internal changes often observed for locally-advanced lung cancer patients. Finally, we evaluate a sparsely-sampled deformable block-matching registration algorithm, which detects local tumor changes through independent rigid registration of many small image sub-volumes near the tumor surface.[11] The current study aims to evaluate and compare these algorithms for potential use during image-guided radiotherapy.

II. METHODS

II.A. Registrations

Four soft-tissue-based automatic registration algorithms were evaluated in this work, including (1) rigid registration of the primary gross tumor volume (GTV), (2) block-matching registration of the primary GTV, (3) deformable registration with the small deformation, inverse consistent linear elastic (SICLE) algorithm, and (4) deformable registration with the diffeomorphic demons algorithm. Refer to Balik *et al.*[12] for details on rigid and deformable registrations and to Robertson *et al.*[11] for details on block-matching registration.

For the first test algorithm, rigid tumor registrations were performed using in-house software, in which the optimal translations and rotations were computed by minimizing the sum-of-squared intensity differences. Only soft-tissue intensities were included in the registration, with CT numbers adjusted on a per-patient basis to exclude bony anatomy. The registered volume on each image was limited to the GTV bounding box plus a uniform 1 cm margin.

For the second test algorithm, a separate in-house block-matching registration tool was also explored in this study. The details of this algorithm are described by Robertson *et al.*[11] Briefly, small (1 cm^3), non-overlapping image sub-volumes (termed “blocks”) were identified on the planning CT near the tumor surface. Between 11 and 121 blocks were identified (median: 39 blocks), depending on the tumor size at the beginning of treatment. Each block was independently and automatically registered to the on-treatment image using only translational degrees of freedom. Then, based on the resulting displacement field, the optimal translation and rotation of the on-treatment image was computed using an orthogonal Procrustes analysis.[11] This method prioritized the alignment of the tumor surface as an important requirement for target localization. The BMR algorithm employed a hierarchical, multi-resolution approach with regularization (median-filtering) performed after registration at each resolution. Previous work has shown that BMR is capable of robust tumor alignment in CT-CT registrations.[11]

For the last two test algorithms, deformable registrations were performed for the entire overlapping region between planning and on-treatment images. For the purpose of target localization, it was necessary in this work to reduce the full deformable registration to a simpler rigid transform representing the couch shift for patient setup corrections. This was accomplished by computing the translations and rotations that best aligned the GTV surface between planning and on-treatment images, consistent with the BMR algorithm. The physician-delineated tumor from the planning CT was converted to a surface mesh and deformably propagated to the on-treatment image using either SICLE or Demons. Then, the optimal rigid transform between the physician and propagated surface meshes was computed using the orthogonal Procrustes analysis. The resulting transform was applied to the on-treatment image for analysis.

II.B. Analysis

Registrations were performed for 16 patients with locally-advanced non-small-cell lung cancer.[12] All patients received a planning four-dimensional (4D) fan-beam computed tomography (FBCT) image at the beginning of treatment. Weekly 4D kilovoltage cone-beam computed tomography (CBCT) images were also acquired for each patient throughout 6 to 8 weeks of conventionally fractionated radiotherapy, for a total of 111 CBCT images. The 4D images were binned into 10 respiratory phases, of which only the end-of-inspiration (EOI) phase was included in this study. Images were initially pre-aligned to bony anatomy using automatic rigid registration, which served as a consistent starting point for all soft-tissue-based registrations.

Each of the four registration algorithms was evaluated based on the accuracy of target localization. Physician contours of the primary tumor were available for all EOI images from FBCT and CBCT scans. Using these contours, target localization errors were assessed using measures of border agreement and volume overlap. First, tumor borders were defined by the minimum bounding box enclosing each target. Radial border errors were then computed as a displacement of the tumor borders from an on-treatment image relative to corresponding borders from the planning CT. Outward border displacements were considered positive radial border errors. The error distributions from opposing target borders (left-right [LR], anterior-posterior [AP], and superior-inferior [SI]) were combined to compute the mean, systematic, and random errors in each direction, from which the required margins were deterimined.[13] Note that margins primarily reflected large residual uncertainties in target localization due to target shape changes and delineation error, with residual registration errors comprising a smaller component. This served as a more clinically relevant endpoint for patient setup corrections.

Volume overlap was computed as the intersection between planning and registered target volumes divided by the registered target volume. Statistically significant differences in volume overlap between registrations were computed using SigmaPlot (version 12.3). Because the overlaps were not normally distributed (Shapiro-Wilk test, $p < 0.05$), statistical differences were determined using the ranks of the data in Friedman's repeated-measures analysis of variance test. The bony anatomy registration and all four soft-tissue-based registrations were included in this evaluation. Pairwise comparisons between registration algorithms were performed using a Tukey test at a significance level of 0.05.

III. RESULTS

Initial target volumes on the planning FBCT averaged 53.7 ± 51.3 cm^3 (range: 7.3 to 192.1 cm^3). Tumors regressed by an average of 42.7% ± 13.3% throughout treatment (range: 21.3% to 64.0%).

Table 1 lists the mean border errors from each registration technique separately in each direction, and Figure 1 shows the systematic and random border errors and the corresponding margins for each cardinal patient axis. Mean border errors ranged from -4.4 to -2.1 cm (LR), -

2.6 to 0.9 cm (AP), and -2.7 to -0.6 cm (SI) for all registrations. Merging the error distributions from opposing target borders resulted in mean differences of 0.3 mm or less between the different registrations. Block-matching registration required the smallest margins in the AP and SI directions (11.1 mm and 12.9 mm respectively) and the second smallest margin in the LR direction (11.1 mm), for which SICLE demonstrated a small advantage (11.0 mm).

The distribution and cumulative histogram of target volume overlaps are shown in Figure 2 and Figure 3 respectively. According to Friedman's test, significant differences were observed between the various registration algorithms ($p < 0.001$). The best target volume overlap was achieved by block-matching registration, which provided statistically significant improvements over all other registration techniques. The 25th-percentile, median, and 75th-percentile volume overlaps were 0.77, 0.83, and 0.90 respectively. All soft-tissue-based registrations provided significantly better volume overlap than bony anatomy alignment. Of the soft-tissue-based registrations, only the rigid and Demons algorithms were not statistically different at the 5% level.

IV. DISCUSSION

In this study, target localization accuracy was assessed from several potential automatic registration algorithms for use during image-guided radiotherapy. Block-matching registration of locally-advanced lung tumors provided a clear advantage in terms of target volume overlap and the required margins to account for border variability. Furthermore, block-matching registration did not result in any volume overlap outliers (Figure 2), indicating superior robustness compared to the other registration techniques. Since BMR rigidly registers small blocks of the image, it is likely less sensitive to cone beam CT image quality issues such as noise and scatter artifact than traditional deformable registration algorithms such as SICLE and Demons.

Rigid registration was not anticipated to dramatically improve tumor localization accuracy, as changes in target shape and size are often more substantial than can captured with a purely rigid transform.[6] Instead, we hypothesized that deformable image registration (DIR) would provide the best target localization accuracy in this study. These algorithms were performed with a much larger number of parameters and were more capable of modeling complex changes in the primary tumor and surrounding anatomy. For tumor localization, it was necessary to reduce the full deformation field to the optimal set of translations and rotations representing a treatment couch shift during online guidance. This process relied on accurate propagation of target contours between planning and on-treatment CTs. Although contour propagation uncertainties were approximately equal to inter-observer delineation uncertainties,[12] DIR uncertainties near the tumor surface directly contributed to target localization errors. SICLE demonstrated smaller margins and significantly better volume overlap than Demons for targets in this study, consistent with previous observations that SICLE provided more reliable contour propagation as well.[12]

Despite the advantages offered by block-matching registration, relatively large margins exceeding 10 mm were still necessary for the current study population as a result of several contributing factors. First, delineation uncertainties can introduce systematic errors of 2 to 7 mm, especially near obscured regions of the tumor surface (e.g., bordering atelectasis).[5] Even greater uncertainties were possible for delineation of CBCT images, where reduced contrast can further obscure tumor boundaries.[14] Large delineation errors were anticipated to reduce the apparent differences between algorithms.

A second contributing factor to the large margins in Figure 1 involved changes in target shape and volume throughout treatment. Target volume regression was greater than 40% on average for patients in this study, consistent with published data by Fox *et al.* (44.3% after 50 Gy), Weiss *et al*. (35% after 5 weeks of treatment), and Lim *et al*. (51% after treatment completion).[1–3] Negative mean border errors were observed in all but the anterior direction, further indicating the degree of target volume regression. Although the GTV appeared well-localized throughout treatment, tumor regression also contributed to larger systematic and random border errors, consequently resulting in larger treatment margins. Adaptive radiotherapy may better account for inter-fractional tumor variability in order to obtain smaller treatment margins without sacrificing dosimetric coverage.[5]

For clinical implementation, automatic registration algorithms should execute in a reasonably short amount of time, such that patient setup errors may be corrected as quickly as possible following image acquisition. Any patient motion that occurs between imaging and setup correction is not measured and could reduce the accuracy of the correction. In the interest of optimal target localization accuracy, registration times were not considered a primary endpoint in this study, and both deformable registration algorithms were optimized for accuracy rather than speed. However, the multi-threaded BMR algorithm was capable of computing patient setup corrections in less than 15 seconds on a 16-core workstation, well within the necessary time constraints for routine clinical use. A second important clinical consideration is the simultaneous localization of multiple treatment targets (including metastatic lymph nodes) and organs at risk. This remains the subject of future work.

V. CONCLUSION

Four automatic soft-tissue-based registration algorithms have been assessed for the localization of locally-advanced primary lung tumors. All four algorithms significantly improved target volume overlap compared to the initial bony anatomy alignment. The most robust and accurate target localization was provided by block-matching registration, which demonstrated the smallest treatment margins and significantly better volume overlap than all other algorithms. However, relatively large margins exceeding 10 mm were still computed for patients in this study, indicating that target localization alone is insufficient for addressing potentially large interfractional uncertainties throughout conventionally fractionated radiotherapy.

ACKNOWLEDGEMENTS

This work was partially supported by NIH R01CA166119 and NIH P01CA116602.

FIGURES AND TABLES

Table 1. Mean border errors (in millimeters) in each of the six patient-specific directions from bony anatomy alignment, rigid tumor registration, block-matching registration (BMR), and deformable registration using the SICLE and Demons algorithms. Positive values indicated a predominantly outward shift of the on-treatment target borders relative to the corresponding tumor border from the planning CT.

Registration	Right	Left	Posterior	Anterior	Superior	Inferior
Bony	-4.4	-2.1	-2.6	0.9	-1.1	-2.5
Rigid	-4.1	-2.2	-2.6	0.9	-1.9	-1.4
BMR	-3.4	-3.2	-1.5	0.0	-2.7	-0.6
SICLE	-3.1	-3.3	-1.6	-0.1	-1.8	-1.2
Demons	-3.1	-3.1	-2.6	0.8	-1.8	-1.4

Figure 1. Systematic and random border errors and corresponding margins in the left-right (LR), anterior-posterior (AP), and superior-inferior (SI) directions. Registrations included bony-anatomy alignment, rigid tumor registration, block-matching registration (BMR), and deformable registration with the SICLE and Demons algorithms.

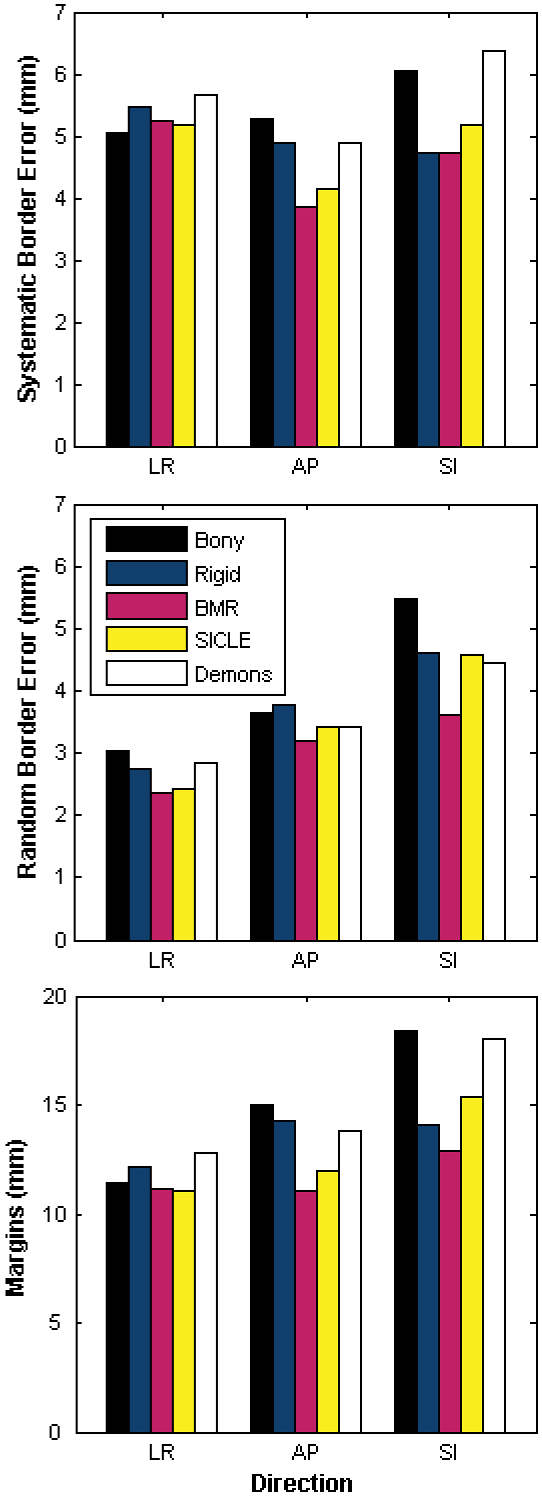

Figure 2. Distribution of target volume overlap indices (registrations as listed in Figure 1). Boxes represent the 25th-percentile, median, and 75th-percentile of overlaps.

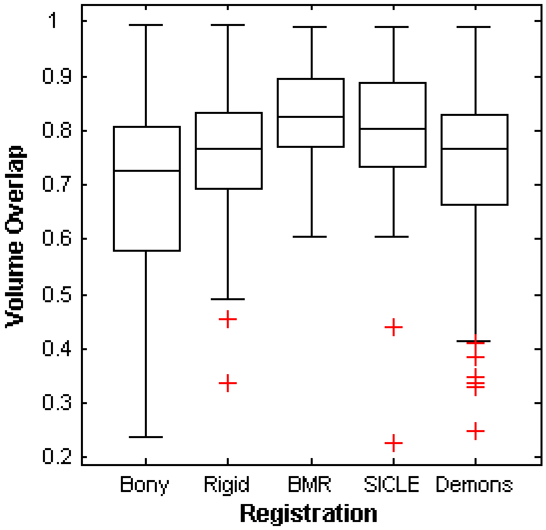

Figure 3. Cumulative histogram of target volume overlaps (registrations as listed in Figure 1).

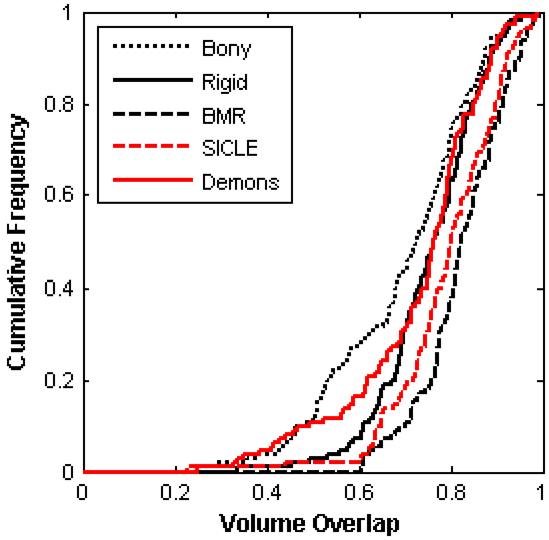

REFERENCES

[1] J. Fox, E. Ford, K. Redmond, J. Zhou, J. Wong, and D. Y. Song, “Quantification of tumor volume changes during radiotherapy for non-small-cell lung cancer,” Int. J. Radiat. Oncol., Biol., Phys. **74**, 341–348 (2009).

[2] E. Weiss, S. P. Robertson, N. Mukhopadhyay, and G. D. Hugo, “Tumor, lymph node, and lymph node-to-tumor displacements over a radiotherapy series: Analysis of interfraction and intrafraction variations using active breathing control (ABC) in lung cancer,” Int. J. Radiat. Oncol., Biol., Phys. **82**, e639–e645 (2012).

[3] G. Lim *et al*., “Tumor regression and positional changes in non-small cell lung cancer during radical radiotherapy,” J. Thorac. Oncol. **6**, 531–536 (2011).

[4] C. K. Glide-Hurst, E. Gopan, and G. D. Hugo, “Anatomic and pathologic variability during radiotherapy for a hybrid active breath-hold gating technique,” Int. J. Radiat. Oncol., Biol., Phys. **77**, 910–917 (2010).

[5] J.-J. Sonke and J. Belderbos, “Adaptive radiotherapy for lung cancer,” Semin. Radiat. Oncol. **20**, 94–106 (2010).

[6] S. P. Robertson, E. Weiss, and G. D. Hugo, “Localization accuracy from automatic and semi-automatic rigid registration of locally-advanced lung cancer targets during image-guided radiation therapy,” Med. Phys. **39**, 330–341 (2011).

[7] N. Mohammed, L. Kestin, I. Grills, C. Shah, C. Glide-Hurst, D. Yan, and D. Ionascu, “Comparison of IGRT registration strategies for optimal coverage of primary lung tumors and involved nodes based on multiple four-dimensional CT scans obtained throughout the radiotherapy course,” Int. J. Radiat. Oncol., Biol., Phys. **82**, 1541–1548 (2012).

[8] L. B. Marks *et al*., “Radiation dose–volume effects in the lung,” Int. J. Radiat. Oncol., Biol., Phys. **76**, S70–S76 (2010).

[9] J. D. Fenwick, A. E. Nahum, Z. I. Malik, C. V. Eswar, M. Q. Hatton, V. M. Laurence, J. F. Lester, and D. B. Landau, “Escalation and intensification of radiotherapy for stage III non-small cell cung cancer: Opportunities for treatment improvement,” Clin. Oncol. **21**, 343–360 (2009).

[10] J. Higgins, A. Bezjak, K. Franks, L. W. Le, B. C. Cho, D. Payne, and J.-P. Bissonnette, “Comparison of spine, carina, and tumor as registration landmarks for volumetric image-guided lung radiotherapy,” Int. J. Radiat. Oncol., Biol., Phys. **73**, 1404–1413 (2009).

[11] S. P. Robertson, E. Weiss, and G. D. Hugo, “Localization of locally-advanced lung tumors using a block-matching registration algorithm,” Med. Phys. (in press).

[12] S. Balik *et al*., “Evaluation of 4-dimensional computed tomography to 4-dimensional cone-beam computed tomography deformable image registration for lung cancer adaptive radiation therapy,” Int. J. Radiat. Oncol., Biol., Phys., (submitted).

[13] G. D. Hugo, E. Al Sulaimani, E. Weiss, and S. P. Robertson, “Evaluation of the carina as a surrogate for daily localization of mediastinal lymph nodes during radiation therapy of locally-advanced lung cancer,” Pract. Radiat. Oncol., (submitted).

[14] E. Weiss *et al*., “Clinical evaluation of soft tissue organ boundary visualization on cone-beam computed tomographic imaging,” International Journal of Radiation Oncology, Biology, Physics **78**, 929–936 (2010).

[15] M. M. Knap, L. Hoffmann, M. Nordsmark, and A. Vestergaard, “Daily cone-beam computed tomography used to determine tumour shrinkage and localisation in lung cancer patients,” Acta Oncol. **49**, 1077–1084 (2010).

[16] A. P. Galerani *et al*., “Dosimetric impact of online correction via cone-beam CT-based image guidance for stereotactic lung radiotherapy,” Int. J. Radiat. Oncol., Biol., Phys. **78**, 1571–1578 (2010).

VITA

Scott Patrick Robertson was born on December 1, 1986 in Columbia, Maryland. He graduated from the Red Lion Area Senior High School, Red Lion, Pennsylvania in 2005. In May 2009, he received his Bachelor of Science in Physics from the University of Maryland, College Park, Maryland, graduating Cum Laude. While at Maryland, Scott spent two summers as an undergraduate research fellow at the National Institute of Standards and Technology, Department of Ionizing Radiation, which motivated his decision to further pursue a career in medical physics. He enrolled at Virginia Commonwealth University in August 2009, joining the research group of Dr. Geoffrey Hugo. To date, he has been the primary author on one peer-reviewed research article, has co-authored three additional research articles, and has contributed to four national or international meeting abstracts. In 2011, he was the first prize recipient of the Young Investigators Competition hosted by the Mid-Atlantic Chapter of the American Association of Physicists in Medicine. For his academic achievements, Scott was inducted into the Honor Society of Phi Kappa Phi in November 2010 and has been awarded two scholarships on behalf of the Virginia Commonwealth University School of Medicine.